Flow sensing with thermal sigma-delta modulators

Makinwa, KAA

Publication date
2004

Document Version
Final published version

Citation (APA)
Makinwa, KAA. (2004). *Flow sensing with thermal sigma-delta modulators*.

FLOW SENSING WITH THERMAL SIGMA-DELTA MODULATORS

FLOW SENSING WITH THERMAL SIGMA-DELTA MODULATORS

PROEFSCHRIFT

ter verkrijging van de graad van doctor
aan de Technische Universiteit Delft
op gezag van de Rector Magnificus prof.ir. J.T. Fokkema,
voorzitter van het College voor Promoties,
in het openbaar te verdedigen
op dinsdag 29 juni 2004 om 10:30 uur.

door

Kofi Afolabi Anthony MAKINWA

Master of Science
Obafemi Awolowo University, Ile-Ife, Nigeria
Master of Electronic Engineering
Philips International Institute, Eindhoven

geboren te Accra, Ghana.

Dit proefschrift is goedgekeurd door de promotor:

Prof.dr.ir. J.H. Huijsing

Samenstelling promotiecommissie:

Rector Magnificus,	voorzitter
Prof.dr.ir. J.H. Huijsing,	Technische Universiteit Delft, promotor
Prof.dr. P.J. French,	Technische Universiteit Delft
Prof.dr.ir. M. Elwenspoek,	Technische Universiteit Twente
Prof.dr. L. Castañer,	Universidad Politécnica de Cataluña
Prof.dr.ir. R. Puers,	Katholieke Universiteit Leuven
Prof.dr. N.F. de Rooij,	Universiteit van Neuchâtel
Dr.ir. F.R. Riedijk,	Xensor Integration, Delft

Printed by [OPTIMA] Grafische Communicatie, Rotterdam

ISBN: 90-77595-61-9

PRINTED IN THE NETHERLANDS

The wind blows wherever it pleases. You hear its sound, but you cannot tell where it comes from or where it is going.

John 3:8

Table of Contents

5 A Smart CMOS Wind Sensor *85*

Introduction 1

Thermal sigma-delta (TΣΔ) modulators are analog-to-digital converters that directly convert an analog heat flow into a digital signal. This thesis describes their application to the interfacing of thermal flow sensors. In this case, the digitized heat flow will be the sensor's heat loss, from which the speed, and in some cases, the direction of a fluid flow can be determined. This introduction begins with an explanation of the basic operating principles of thermal flow sensors. This is followed by a review of the traditional methods with which such sensors have been interfaced. The basic operating principles of TΣΔ modulators and their application to the interfacing of thermal flow sensors are then described. Finally, the motivation and organization of this thesis is presented.

1.1 Thermal Flow Sensors

Flow sensors are indispensable in many applications, e.g. process control, environmental monitoring, drug dispensation, and industrial metering. Over the last two decades or so, a major scientific effort has been devoted to their realization in silicon. This has been motivated by the fact that such sensors can be batch fabricated at low cost using integrated circuit (IC) technology. In consequence, the required interface electronics can then be realized on the same chip as the sensor. The ultimate goal of this effort is the realization of low-cost *smart* flow sensors, that is, flow sensors whose output is a robust (digital) signal [1.1–1.5].

Although the movement of fluid can be measured using many physical principles, the majority of silicon flow sensors found in literature have employed thermal operating principles [1.6]. This is due to the fact that the required heaters and temperature sensors, can be readily implemented in IC technology [1.7]. The operation of these *thermal* flow sensors is

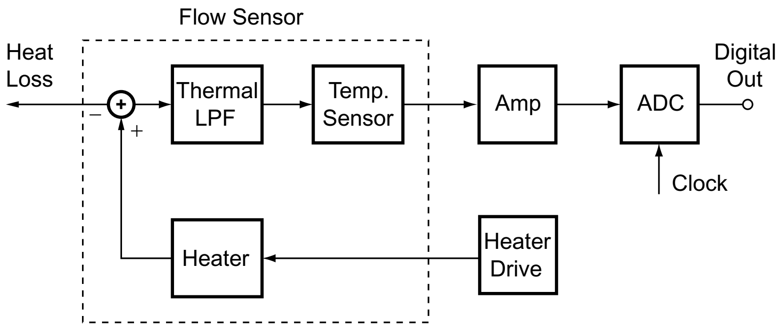

Figure 1-1 *Open-loop interfacing of a thermal flow sensor.*

based on the convective cooling of a heated object (the sensor) by a flow. In general, this will result in two effects. Firstly, the total heat loss of the object will be a function of flow speed. Flow sensors based on this effect are known as *thermal anemometers.* Secondly, the object will be differentially cooled, with most of its heat loss occurring upstream, at the point where it first encounters the flow. Flow sensors based on this effect are known as *calorimetric flow sensors*, and can determine both flow speed and direction.

1.2 Interfacing Thermal Flow Sensors

The task of interfacing thermal flow sensors is one of converting their flow-dependent heat loss into a robust (digital) signal. This should be done with a minimum of circuitry, and in such a way that it maximizes the performance of the flow sensor. To accomplish this task, both open-loop and closed-loop approaches have been used.

In the open-loop approach, the flow sensor is heated above ambient temperature, and its flow-dependent heat loss causes temperature changes which are converted by a temperature sensor into an electrical signal (Fig. 1-1). This signal is then periodically sampled and digitized by an analog-to-digital converter (ADC). This approach is quite straightforward and has been used to interface both thermal anemometers and calorimetric flow sensors [1.6]. However, it suffers from two important drawbacks: the

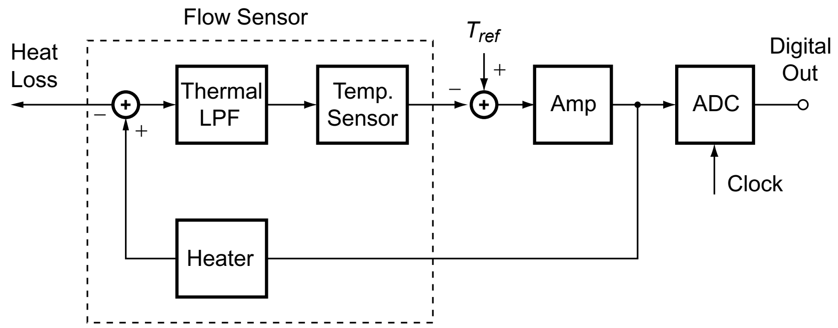

Figure 1-2 *Closed-loop interfacing of a thermal flow sensor.*

response time of the system will be limited by the flow sensor's thermal inertia (which may be modelled as a low-pass filter (LPF) in the thermal domain), and the accuracy of the system's transfer function will be influenced by *all* the elements in the measurement chain.

These limitations can be alleviated by the use of a closed-loop approach, in which a feedback loop maintains the sensor at a constant temperature T_{ref} (Fig. 1-2). The required heating power compensates for the sensor's heat loss, and will, therefore, be a function of flow speed. Compared to the open-loop approach, this approach results in faster response because the sensor's temperature is fixed. Furthermore, the transfer function of the closed-loop system will be determined mainly by the feedback element, that is, the heater, provided that the total loop gain is much greater than one. Due to these advantages, this approach has often been used to interface thermal anemometers [1.6, 1.8].

Calorimetric flow sensors can also be interfaced using a closed-loop approach. In this case, the temperature sensor now measures temperature *differences*, and the feedback loop (Fig. 1-2) varies the distribution of heat in the sensor such that flow-induced temperature differences are cancelled, i.e., $T_{ref} = 0$. The required heat distribution compensates for the sensor's differential heat loss, and thus provides information about flow speed and direction. Although proposed more than a decade ago [1.9], and again recently [1.10], this method of interfacing calorimetric flow sensors has not yet been investigated in detail.

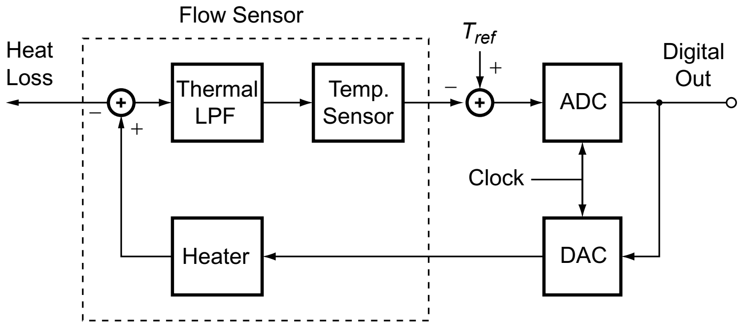

Figure 1-3 *Block diagram of a thermal sigma-delta modulator.*

The closed-loop approach can be developed further by incorporating the ADC in the feedback loop (Fig. 1-3). Since the output of the loop is now a digital signal, a digital-to-analog converter (DAC) is required to drive the heater. The resulting closed-loop system now performs two functions: it maintains the sensor at a fixed temperature T_{ref} and simultaneously digitizes its heat loss. This topology is functionally identical to that of a sigma-delta modulator (described in the next section), and as such it is known as a *thermal* sigma-delta modulator [1.11].

1.3 Sigma-Delta Modulators: The Basics

A sigma-delta (ΣΔ) modulator is a feedback loop in which an analog input signal is continuously balanced by a digital *approximation*. (Fig. 1-4). The resulting error signal is integrated, periodically sampled (at a frequency f_s) and then quantized, i.e., mapped to a finite number of levels, by an ADC. The feedback loop is completed by a DAC. As a result of the feedback, the *average* value of the ADC's output will be a digital representation of the average value of the input signal [1.12].

Since the ADC has finite resolution, its output will contain quantization errors. Viewed in the frequency domain (Fig. 1-4a), these errors may be regarded as a form of noise (known as quantization noise) whose power is distributed between DC and half the sampling frequency, i.e., $f_s/2$.

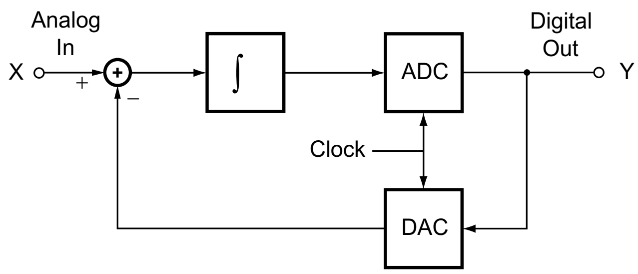

Figure 1-4 *Block diagram of a sigma-delta modulator.*

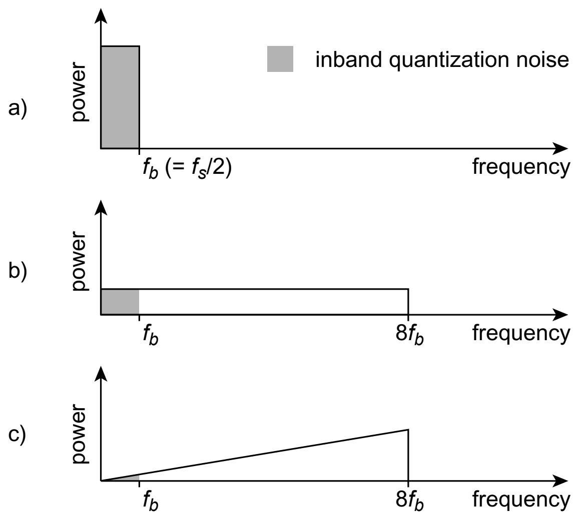

Figure 1-5 *Quantization noise spectrum for a) Nyquist-rate sampling, b) oversampling and c) oversampling with noise-shaping.*

According to the Nyquist theorem, if the bandwidth of the input signal extends from DC to f_b, it must be sampled at a minimum frequency of $2f_b$ to prevent aliasing. If the signal is *oversampled*, that is, if a sampling frequency greater than $2f_b$ is used, the quantization noise power will be spread over a larger frequency range, and so the noise power present in the signal band will decrease (Fig. 1-4b). The degree of oversampling is usually denoted by the so-called oversampling ratio, $OSR = f_s/(2f_b)$.

The integrator in the loop also assists in reducing any quantization noise in the signal band. This is because it suppresses quantization noise in the modulator's bitstream output more effectively at low frequencies than at high frequencies. The quantization noise is then said to be *noise-shaped*. As shown in Fig. 1-4c, the combination of noise-shaping and oversampling ensures that the quantization noise power in the signal band decreases rapidly as the sampling frequency is increased. Most of the quantization noise will then lie *outside* the signal band, where it can be removed by a digital low-pass filter.

Improved noise-shaping can be obtained by replacing the integrator with a higher-order loop filter. However, for filter orders greater than two, careful design is required to prevent the feedback loop from becoming unstable. By choosing the filter order and oversampling ratio appropriately, very high resolution (in a given signal band) can be achieved with a simple 1-bit ADC and DAC. Their ability to trade sampling rate for resolution is the main reason why ΣΔ modulators are so widely used.

1.4 Thermal Sigma-Delta Modulators

As shown in Fig. 1-3, a *thermal* sigma-delta (TΣΔ) modulator is a ΣΔ modulator whose summing "node" is in the thermal domain. In the case of a flow sensor, the summing node is the thermal mass of the sensor itself, which is heated above ambient temperature and cooled by the flow. The modulator's output will then be a digital representation of the sensor's flow-dependent heat loss. The sensor's thermal inertia may also be used as a loop filter, since it behaves like a low-pass filter in the thermal domain.

The implementation of a TΣΔ modulator can be greatly simplified by using a 1-bit ADC. In this case, the ADC can be simply implemented as a clocked comparator (Fig. 1-6). Furthermore, no explicit DAC is required, since the heater can be driven by the comparator's binary output. Compared to the interface architectures of Fig. 1-1 and Fig. 1-2, the result is a compact interface architecture, which retains all the advantages of the closed-loop approach.

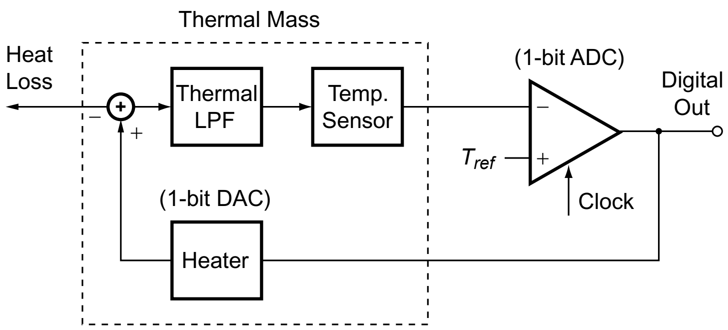

Figure 1-6 *Block diagram of a thermal sigma-delta modulator that uses a 1-bit ADC.*

Because it leaks heat to the surroundings, a thermal low-pass filter, unlike an ideal integrator, will have a finite DC gain. As a result, the DC transfer function of the Fig. 1-3 modulator, unlike that of an ideal ΣΔ modulator, will be non-linear. Fortunately, the degree of non-linearity decreases with increasing clock frequency. For design purposes, an analytical relationship describing this trade-off would be useful. However, due to the complexity of the analysis, such a relationship is only known for the case of a single-pole loop filter [1.13]. Some approximate results have been derived for thermal anemometers, which may be modelled as a special class of multiple-pole filter [1.14]. Modulator linearity can also be improved by architectural modifications such as the use of multi-bit quantizers or the use of extra filtering in the electrical domain [1.15].

Since the bandwidth of a thermal flow sensor is rather small (typically ranging from a few Hertz to a few kilohertz), high oversampling ratios may be readily employed, and so a 1-bit ADC will provide sufficient linearity and resolution. Such single-bit TΣΔ modulators have been mainly used to interface thermal anemometers [1.11, 1.15–1.17]. They have also been used to interface thermal root-mean-square converters [1.18] and thermal conductivity sensors [1.19]. Although their application to the interfacing of calorimetric flow sensors has been suggested [1.20], no operational systems have been demonstrated.

1.5 Motivation

As has been shown in the previous sections, the use of TΣΔ modulators to interface thermal flow sensors combines the advantages of closed-loop operation with digital output. Despite these advantages, however, this approach has not (yet) been widely used. One reason for this may be the fact that not much research work has been done in this area. Furthermore, most of this work has concentrated on the interfacing of thermal anemometers. Another, related, reason is the absence of a well-defined design methodology. The main aim of this thesis, therefore, is to investigate the application of TΣΔ modulators to the interfacing of thermal flow sensors in general, and of calorimetric flow sensors in particular. A secondary aim is the development of a design methodology for TΣΔ modulators based on the extraction of frequency-domain models of thermal flow sensors. This methodology was verified by the design and realization of interface circuitry for a hot-transistor anemometer: a thermal anemometer based on a self-heated transistor. In addition, a smart wind sensor has been realized: a silicon chip on which a two-dimensional calorimetric flow sensor and its interface circuitry have been integrated.

1.6 Thesis Organization

Besides this introductory chapter, this thesis consists of six chapters and an appendix. Chapter 2 is an introduction to thermal flow sensors. The main classes are identified, together with their operating principles and distinguishing characteristics. Also described are the various modes in which these sensors can be operated. Many examples are given of the realization of thermal flow sensors in silicon using the various heating and temperature sensing devices available in IC technology.

In Chapter 3, the properties of thermal filters are discussed, and the consequences for the stability and linearity of TΣΔ modulators investigated. Analytical results for a multiple-pole thermal anemometer (derived in the appendix) are presented. For calorimetric flow sensors, a discrete-time representation was developed with which fast time-domain simulations can be carried out. Finally, different architectural options for improving the linearity of these modulators are described.

In Chapter 4, the realization of a low-cost flow sensor based on a self-heated bipolar transistor is described. The extraction of a frequency-domain model of the transistor is presented. Due to its poor filtering characteristics, the transistor was interfaced by a TΣΔ modulator with an extra electrical integrator. The realization of this modulator, using a new technique for measuring small temperature differences with bipolar transistors, is described. Finally, the results of wind tunnel measurements on the anemometer are given.

Chapter 5 describes the realization of three 2-D wind sensors with different interface architectures in a standard CMOS process. The first two chips were used to design and validate elements of an interface architecture based on three TΣΔ modulators, and so are only briefly described. The third chip, a smart wind sensor, is a realization of the complete architecture and is described in more detail. Finally, the results of wind tunnel measurements on the smart wind sensor are given.

In Chapter 6, the main conclusions of the thesis are presented and some recommendations for future work are made.

1.7 References

[1.1] G. Stemme, "A CMOS integrated silicon gas-flow sensor with pulse-modulated output," *Sensors and Actuators A: Physical*, vol. 14, no. 3, pp. 293-303, July 1988.

[1.2] E. Yoon and K.D. Wise, "An integrated mass-flow sensor with on-chip CMOS interface circuitry," *IEEE Trans. on Electron Devices*, vol. 39, no. 6, pp. 1376-1386, June 1992.

[1.3] R. Kersjes, F. Liebscher, E. Spiegel, Y. Manoli and W. Mokwa, "An invasive catheter flow sensor with on-chip CMOS read-out electronics for the on-line determination of blood flow," *Sensors and Actuators A: Physical*, vol. 54, no. 1-3, pp. 563 - 567, June 1996.

[1.4] P. Malcovati et al., "Combined air humidity and flow CMOS microsensor with on-chip 15 bit sigma-delta A/D interface," *Symp. VLSI Circuits Dig. Tech. Papers*, pp. 45-46, 1995.

[1.5] F. Mayer, A. Haberli, G. Ofner, H. Jacobs, O. Paul and H. Baltes, "Single-chip CMOS anemometer," *Digest of IEDM 1997*, pp. 895-898, Dec. 1997.

[1.6] A. Rasmussen and M.E. Zaghloul, “In the flow with MEMS,” *IEEE Circuits and Systems Magazine*, vol. 14, no. 4, pp. 12-25, July 1998.

[1.7] M. Elwenspoek and R. Wiegerink, “Mechanical Microsensors, Berlin, Springer-Verlag, 2001.

[1.8] B.W. van Oudheusden, “Effect of operating conditions on the dynamic response of thermal sensors with and without analog feedback,” *Sensors and Actuators A: Physical*, vol. 58, no. 2, pp. 129 -135, Feb. 1997.

[1.9] B.W. van Oudheusden and J.H. Huijsing, “The thermal modelling of a flow sensor based on differential convective heat transfer,” *Sensors and Actuators A: Physical*, vol. 29, no. 2, pp. 93-106, Nov. 1991.

[1.10] T.S.J. Lammerink, N.R. Tas, G.J.M. Krijnen and M.C. Elwenspoek, “A new class of thermal flow sensors using $\Delta T = 0$ as a control signal,” *Proc. of MEMS 2000*, pp. 525-530, Jan. 2000.

[1.11] Y. Pan, F.R. Riedijk and J.H. Huijsing, “A new class of integrated thermal oscillators with duty-cycle output for application in thermal sensors,” *Sensors and Actuators A: Physical*, vol. 21-23, pp. 655-659, Mar. 1990.

[1.12] S.R. Norsworthy, R. Schreier and G.C. Temes (Eds.), “Delta-sigma data converters,” New York, IEEE Press, 1997.

[1.13] O. Feely and L.O. Chua, “The effect of integrator leak in Σ–Δ modulation,” *IEEE Transactions on Circuits and Systems*, vol. 38, no. 11, pp. 1293-1305, Nov. 1991.

[1.14] M. Domínguez and L. Castañer, “Bounding of thermal Σ–Δ modulators’ output for sensors,” *Proc. of ISCAS ‘99*, vol. 2, pp. 244-247, 1999.

[1.15] H.-J Verhoeven, “Smart thermal flow sensors,” Ph.D. thesis, Delft University of Technology, 1996.

[1.16] L. Castañer, V. Jimenez, M. Domínguez, F. Masana and A. Rodriguez “A conduction-convection design for liquid flow sensing,” *Sensors and Actuators A: Physical*, vol. 66, no. 1-3, pp. 131-137, April 1998.

[1.17] M. Domínguez, F. Masana, V. Jimenez, S. Bermejo, J. Amirola, J. Ballester, N. Fueyo and L. Castañer, “Low-cost thermal TΣΔ airflow sensor,” *IEEE Sensors Journal*, vol. 2, no. 5, pp. 453–462, October 2002.

[1.18] D. Jaeggi, C. Azeredo Leme, P. O’Leary and H. Baltes, “Improved CMOS power sensor,” *Proc. of Transducers ‘93*, pp. 462-465, June 1993.

[1.19] C. Condemine, M. Belleville, D. Barbier, G. Delhomme and A. Dittmar, “A new sigma-delta thermal conductivity microsystem,” *Proc. of the 1st IEEE EMBS conference*, pp. 188-91, Oct. 2000.

[1.20] J.K. Zelisse, F.R. Riedijk and J.H. Huijsing, “Thermal sigma-delta modulator for wind speed and direction measurement,” *Proc. of Eurosensors V*, p. 303, Sept. 1991.

Thermal Flow Sensors 2

The operation of thermal flow sensors is based on the interaction between a heated object and a fluid (liquid or gas) flow. In general, heat will be transferred from the object to the flow, or in other words, the object will be cooled by the flow. Furthermore, the object will be cooled in a non-uniform manner, with its upstream region experiencing the most cooling. Based on these two effects, a wide variety of thermal flow sensors have been devised. In this chapter, it will be shown that these can be grouped into three main classes: thermal anemometers, calorimetric flow sensors and thermal time-of-flight sensors. An overview will be given of the main characteristics of each of these classes, and of the different modes in which they can be operated. In addition, the realization of such sensors in standard IC technology will be described.

2.1 Classification of Thermal Flow Sensors

Based on the way they interact with the flow, thermal flow sensors can be divided into three main classes [2.1, 2.2]:

- *thermal anemometers*
- *calorimetric sensors*
- *thermal time-of-flight sensors*

Thermal anemometers measure the total heat loss of a single heated object. Since they only measure one parameter, such sensors can only determine flow speed. Both flow speed *and* direction can be determined by calorimetric sensors, which measure the flow-dependent modulation of the heat distribution in or around a heated object. Lastly, thermal time-of-flight sensors, as their name implies, measure the time it takes for a heated volume of fluid to travel a known distance. As such, they are relatively insensitive to variations in the physical properties of the fluid.

It should be noted that the *names* of the various classes are by no means standardized. For instance, thermal anemometers are sometimes referred to as heat-loss sensors or hot-wire anemometers, and calorimetric flow sensors are sometimes referred to as thermotransfer or direction-sensitive flow sensors. However, the names given in the list above are the ones most commonly found in the literature.

2.2 Thermal Anemometers

Thermal anemometers determine flow *speed* by measuring the heat loss of a single heated object. The relationship between the heating power P dissipated in the object and the flow speed U was first derived by King for a laminar flow over a thin wire [2.3], and for this reason it is known as King's law. It states that:

$$\frac{P}{\Delta T} = A + B\sqrt{U} \qquad (2\text{-}1)$$

in which A and B are constants and ΔT is the *overheat*, i.e. the difference between the temperature of the *surface* exposed to the flow and ambient temperature. The constants A and B represent the wire’s heat loss by conduction (to its supports) and convection (to the fluid), respectively. Their magnitude depends on the sensor geometry and on the physical properties of the fluid, the most important of which are its thermal conductivity, density, viscosity and specific heat. Due to the temperature dependence of these properties, the constants of King’s law will, in general, be temperature dependent.

Although developed for a cylindrical wire, King’s law has been found to hold for many other sensor geometries. In some cases, however, e.g. [2.4, 2.5], a better representation of the experimentally observed behaviour is obtained with the following generalized version of King's law:

$$\frac{P}{\Delta T} = A + BU^n \tag{2-2}$$

where n is a constant that depends on the geometry of the sensor and on whether the flow is laminar ($n \sim 0.5$) or turbulent ($n \sim 0.8$).

From (2-2), the *speed* of the flow can be determined if the sensor's power dissipation and overheat are known. The *direction* of the flow can be determined by arranging *multiple* anemometers to measure various components of the flow velocity [2.6, 2.7].

2.2.1 Examples

The best known example of a thermal anemometer is the hot-wire anemometer [2.3]. It consists of a thin metal wire (typically only a few micrometers in diameter) which is heated by an electrical current. The temperature of the wire is determined by measuring its resistance, which will usually be a function of temperature. A second, unheated wire can be used to measure ambient temperature. Since the thermal inertia of the wire is quite small, very fast response times (in the microsecond range) can be achieved. Because the thin wire is rather fragile, however, the more robust (but slower) hot-*film* anemometer has been developed, in which the sensing element is a thin-film resistor on an insulating substrate.

Miniature thermal anemometers have been realized in silicon using heaters on micromachined structures such as bridges [2.8] and membranes [2.4], which are thermally isolated from a (relatively) massive silicon substrate. Due to the isolation, the resulting response times are quite fast (in the millisecond range).

Non-micromachined thermal anemometers have also been implemented in standard IC technology. These typically consist of a silicon chip on which a heating resistor and a transistor-based temperature sensor have been integrated [2.5, 2.9, 2.10, 2.11]. A self-heated bipolar transistor can also be used as a low-cost thermal anemometer [2.12]. Due to their

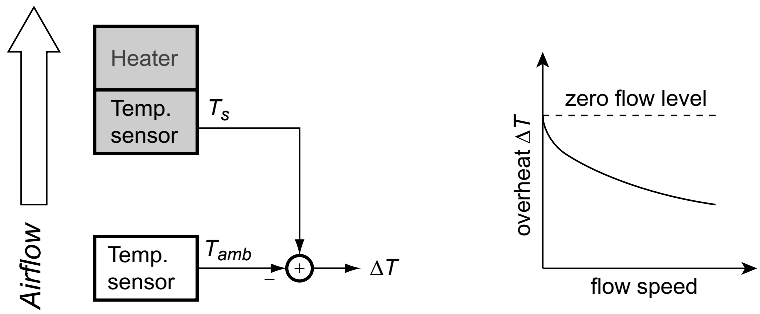

Figure 2-1 *CP operation of a thermal anemometer.*

significantly larger size, however, such sensors are much slower (with typical time constants of a few hundred milliseconds) than their micromachined counterparts.

2.2.2 Operating Modes

From King's law, the flow speed can be determined from two parameters: the heater power dissipation P and the overheat ΔT. In practice, one of these parameters is kept constant while the other is varied. This results in two distinct operating modes: constant power (CP) mode and constant temperature difference (CTD) mode.

In CP mode, a constant heating power is dissipated in the sensor. Power-regulating circuits [2.13, 2.14] can be used to ensure that its power dissipation is indeed constant, since the resistance of a heating resistor will typically be temperature dependent. In many cases, the resistor is simply driven at constant current or voltage and any resistance variations are compensated for by calibrating the sensor. From King's law, the sensor's overheat will vary with flow speed (Fig. 2-1). As a result, the sensor's response time will be limited by its thermal time constant. Furthermore, the sensor's characteristic will be influenced by the temperature dependence of the sensor *and* of the physical properties of the fluid.

Both these drawbacks can be mitigated by operating the sensor in CTD mode, in which a feedback loop maintains the sensor at a constant

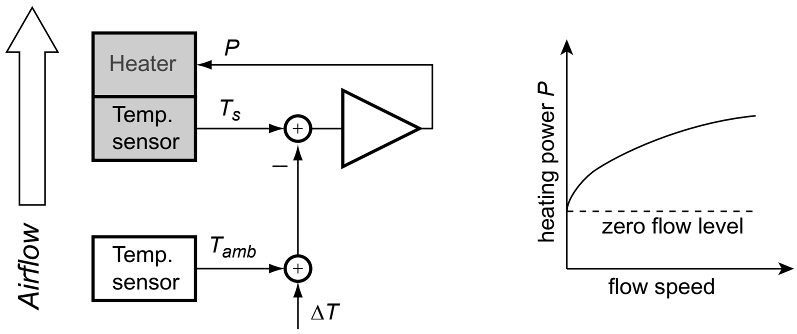

Figure 2-2 *CTD operation of a thermal anemometer.*

overheat (Fig. 2-2). The use of feedback will significantly increase the bandwidth, and hence decrease the response time of the resulting closed-loop system [2.15]. In CTD mode, information about flow speed will be contained in the sensor's power dissipation, which, from King's law, will increase with the square root of flow speed.

To avoid the need for an ambient temperature sensor, hot-wire anemometers are sometimes operated in constant temperature (CT) mode. Reasonable accuracy can be achieved, provided that the overheat is much larger than the expected fluctuations in ambient temperature.

2.3 Calorimetric Flow Sensors

Calorimetric flow sensors make use of the fact that the symmetry of the heat distribution in (or around) a hot object will be modulated by the flow. The degree of asymmetry is determined by measuring the flow-induced temperature difference between two (or more) points symmetrically located around the heater(s). This difference will be a function of both flow speed and direction. Based on this principle, both one-dimensional (1-D) and two-dimensional (2-D) flow sensors have been realized [2.1]. In general, the characteristic of a calorimetric sensor will be a function of the geometry of the sensor, the geometry of the flow channel and of the physical properties of the fluid [2.16, 2.17].

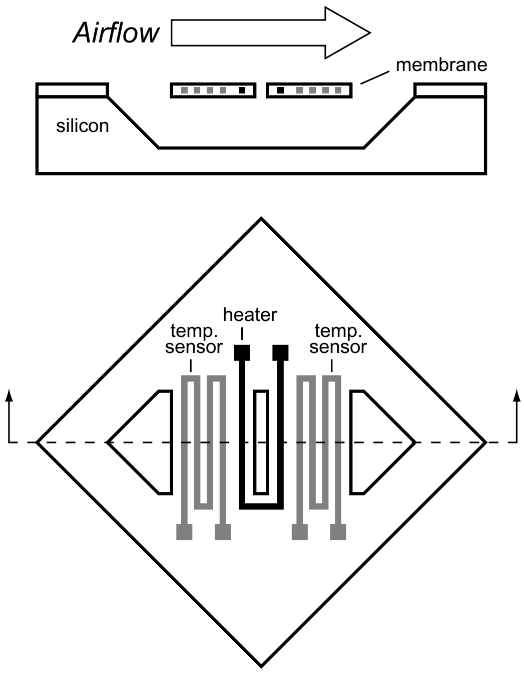

Figure 2-3 *A 1-D micromachined calorimetric flow sensor.*

2.3.1 Examples

An example of a 1-D calorimetric flow sensor is the micromachined airflow sensor developed by Honeywell [2.18, 2.19]. This was one of the first commercially available silicon flow sensors. It consists of three resistors laminated into a thermally insulating dielectric membrane, as shown in Fig. 2-3. One of the resistors is used as a heater (operated in CTD mode), while the other two are used as temperature sensors, and are arranged symmetrically downstream and upstream of the heater.

At zero flow, the heat distribution in the sensor is symmetric, and so the temperature difference between the two sensors δT will be zero. In the presence of flow, the upstream sensor will be cooled, while the downstream sensor will be heated by heat transported from the heater by

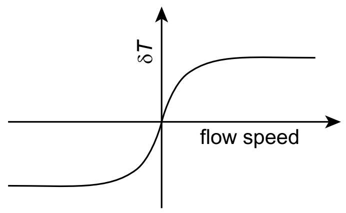

Figure 2-4 *Typical characteristic of a 1-D micromachined calorimetric sensor.*

the flow. At low flow speeds, δT will be an approximately linear function of flow speed, while flow direction δT can be determined from its polarity (Fig. 2-3). At high flow speeds, however, δT will saturate because the upstream sensor cannot be cooled below ambient temperature, while the downstream sensor cannot become hotter than the heater. The sensor has a response time of only a few milliseconds, since the resistors are small and well isolated from the substrate.

Similar micromachined flow sensors have been realized using germanium thermistors [2.20], and integrated thermopiles [2.21, 2.22, 2.23] as temperature sensors. A simpler sensor structure can be obtained by using *self-heated* temperature sensing resistors, in which case only two resistors are required [2.24].

An example of a 2-D calorimetric flow sensor is the wind sensor described in [2.25, 2.26], and developed by Mierij Meteo BV into a commercial product [2.27]. It consists of a square, non-micromachined chip on which four heaters, four thermopiles, and an NPN transistor have been integrated (Fig. 2-5). The chip is bonded to a thin ceramic disc, which protects it from direct contact with the airflow. Since ceramic is a fairly good heat conductor, the chip will still be in *thermal* contact with the airflow.

In operation, a control loop maintains the chip's average temperature (as measured by the NPN transistor) at a constant overheat ΔT, thus creating a hot spot on the surface of the disc. Airflow passing over the *other* side of the disc will then cool it asymmetrically, and induce a net temperature gradient $\delta \boldsymbol{T}$ across the chip. The magnitude of $\delta \boldsymbol{T}$ will be a function of flow speed, while its direction will be the same as that of the flow.

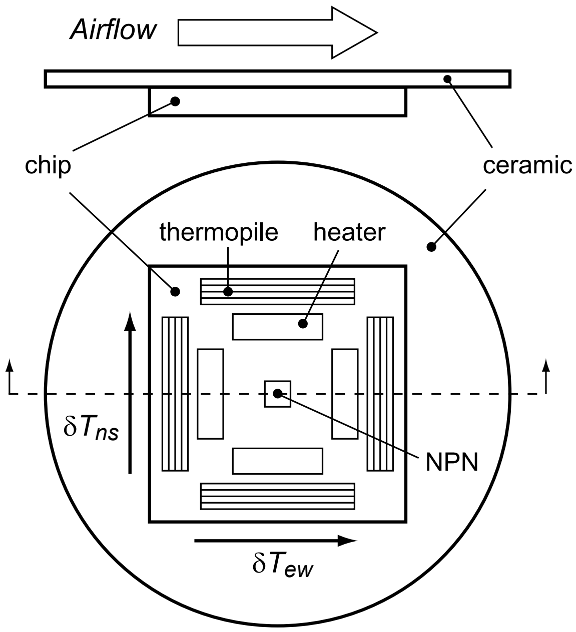

Figure 2-5 *A 2-D calorimetric flow sensor (the disc is not drawn to scale, it is actually much larger than the sensor).*

Orthogonal components (δT_{ns} and δT_{ew}) of $\delta \boldsymbol{T}$ are measured by the thermopiles. Since silicon is a good thermal conductor, these temperature differences are quite small (less than 1% of the overheat). In this case, it can be shown [2.25, 2.28] that:

$$\frac{\delta T_{ns}}{\Delta T} = S\sqrt{U_{ns}} \qquad \frac{\delta T_{ew}}{\Delta T} = S\sqrt{U_{ew}} \tag{2-3}$$

where ΔT is the overheat, S is a constant that depends on sensor geometry and fluid properties, and U_{ns} and U_{ew} are the corresponding components of flow velocity. From (2-3), δT_{ns} and δT_{ew} will be sinusoidal functions of flow direction, Φ, whose amplitude will increase with flow speed U (Fig.

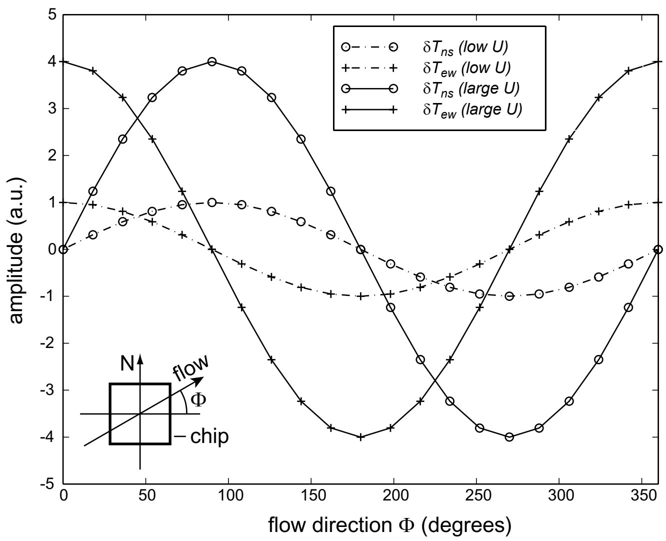

Figure 2-6 *Flow-induced temperature differences in a 2-D calorimetric flow sensor.*

2-6). Since ΔT is known, U_{ns} and U_{ew} can be determined from δT_{ns} and δT_{ew}, and in turn, flow speed U and direction Φ can be determined from:

$$U = \sqrt{U_{ns}^2 + U_{ew}^2} = \frac{\sqrt{\delta T_{ns}^2 + \delta T_{ew}^2}}{S\Delta T}, \tag{2-4}$$

$$\Phi = \operatorname{atan}\frac{U_{ns}}{U_{ew}} = \operatorname{atan}\frac{\delta T_{ns}}{\delta T_{ew}}. \tag{2-5}$$

It is of interest to note that the expression for flow direction Φ is independent of sensor and fluid properties. A detailed analysis, however, shows that sensor geometry will play a role [2.25]. In practice, the computed flow direction is quite accurate: errors less than ±2° have been obtained with a 6x6mm sensor [2.29]. The variation of the computed flow speed as a function of direction is also small: less than ±3%. However, the sensor is relatively slow, having a response time of about 2 seconds to changes in flow direction. This is mainly due to the thermal inertia of the ceramic disc, since the theoretical response time of the chip alone is estimated to be only 40ms [2.29].

Two-dimensional sensors have also been realized on thin micromachined substrates [2.30–2.32]. This enhances their sensitivity and response speed, at the expense of mechanical robustness. If the substrate is insulating, however, the flow-induced temperature differences will become large compared to the overheat, and so (2-3) no longer applies. At low flow speeds, the magnitude of the temperature differences will typically be a linear function of flow speed [2.31].

2.3.2 Possible Operating Modes

As is the case with thermal anemometers, the response of calorimetric flow sensors will be greatly influenced by their operating mode. Since *both* the sensor's (average) temperature T_S as well as the flow-induced temperature gradient $\delta\boldsymbol{T}$ can either be measured or regulated, several operating modes are possible. Depending on whether $\delta\boldsymbol{T}$ is measured or regulated, these operating modes can be subdivided into two groups.

One group consists of operating modes in which flow speed and direction are determined by measuring a temperature gradient $\delta\boldsymbol{T}$. These modes will therefore be referred to as *temperature gradient* (TG) modes. Two such modes have been extensively used: one in which the *total* power dissipated in the sensor is kept constant (CP-TG mode), and one in which the sensor's (average) overheat is kept constant (CTD-TG mode). In a few cases, the sensor's *absolute* temperature is kept constant (CT-TG mode) [2.33].

The other group consists of operating modes in which $\delta\boldsymbol{T}$ is regulated. This has been suggested in the past [2.28], but only recently have experimental results been published [2.34, 2.35]. These operating modes will be referred to as *temperature balance* (TB) modes, after [2.34]. In these modes, the power dissipated in *multiple* heaters is varied so as to *cancel* the flow-induced temperature gradient, i.e., $\delta\boldsymbol{T} = 0$. For a 1-D sensor, the temperature difference δT can be cancelled by an appropriately located *pair* of heaters (Fig. 2-5). Flow speed and direction can then be determined by measuring the required differential heating power, δP. The

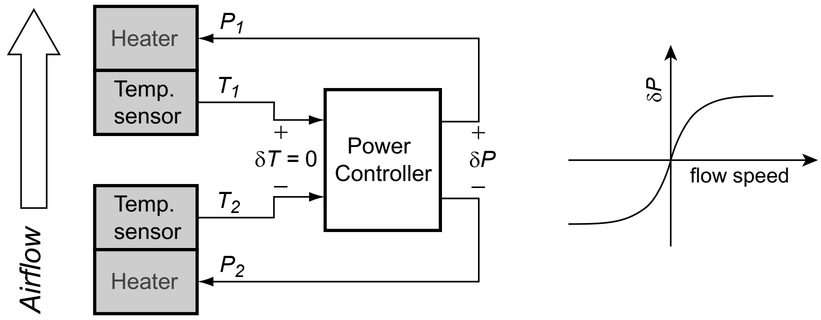

Figure 2-7 *TB operation of a 1-D calorimetric flow sensor.*

total power dissipated in the sensor may either be kept constant (CP-TB mode), or may be regulated such that the overheat is kept constant (CTD-TB mode).

The various modes in which calorimetric flow sensors may be operated are summarized in table 2-1.

Table 2-1 *Operating modes of a calorimetric flow sensor*

	unregulated $\delta \boldsymbol{T}$	regulated $\delta \boldsymbol{T}$
unregulated T_S	CP-TG	CP-TB
regulated T_S	CTD-TG, CT-TG	CTD-TB

In the TG modes, the non-idealities (non-linearity, sensitivity variations, offset etc.) of the temperature sensor(s) used to measure $\delta \boldsymbol{T}$ will influence the output of the flow sensor. Despite this disadvantage, most of the calorimetric sensors reported in literature have been operated this way. The main advantage of the TB modes is that the temperature sensors are only used as null detectors. As a result, the output of the flow sensor will be influenced *only* by temperature sensor offset. However, the extra accuracy is achieved at the expense of an extra control loop.

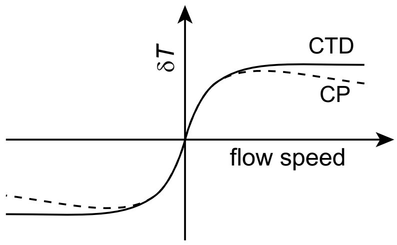

Figure 2-8 *Characteristic of a 1-D micromachined calorimetric sensor as a function of its operating mode.*

2.3.3 Temperature Gradient Modes

In most micromachined sensors, e.g. the Honeywell sensor (Fig. 2-3), the heater(s) and the temperature sensor(s) will be thermally isolated. Since their thermal time constants will then be roughly the same, operating the heater in CTD rather than CP mode will not significantly improve the sensor's response time. For simplicity, therefore, such sensors are typically operated in CP-TG mode. In this mode, the heater's temperature will decrease with increasing flow speed and as a result, the flow-induced temperature difference(s) will saturate and also *decrease* with increasing flow speed [2.31, 2.36] (Fig. 2-8). In contrast, operating the heater in CTD mode results in a monotonic characteristic [2.18]. This is also the case when the average overheat of the *membrane* (as measured by the temperature sensors) is kept constant [2.20].

Another method of extending the monotonic range of a micromachined sensor is by measuring the overheat of the *fluid* ΔT_f in the neighbourhood of the heater, and then using the quotient $\delta T/\Delta T_f$ as a measure of flow speed [2.23]. This technique also significantly reduces the sensor's sensitivity to the fluid's thermal conductivity, and thus, to ambient temperature.

In the 2-D sensor of Fig. 2-5, the heaters and temperature sensors are thermally coupled via the substrate. Also, since silicon has a low thermal resistance, the time constant associated with the overheat will be much larger than that associated with the flow-induced temperature differences [2.29]. In this case, operation in CTD-TG mode will result in faster response times than operation in CP-TG mode. From (2-3), the flow-induced temperature differences in CTD-TG mode will be proportional to the square root of flow speed.

The 2-D sensor can also be operated in CP-TG mode. This simplifies matters, because the overheat control loop and the associated temperature sensors are no longer required. However, this will be at the expense of a slower response time. Noting that the sensor's overheat will then be governed by King's law, the resulting temperature differences can be obtained by combining (2-1) and (2-3):

$$\delta T_{ns} = \frac{P\sqrt{U_{ns}}}{C + D\sqrt{U_{ns}}} \qquad \delta T_{ew} = \frac{P\sqrt{U_{ew}}}{C + D\sqrt{U_{ew}}} \tag{2-6}$$

where C and D are sensor constants. Thus the temperature differences will still be monotonically increasing functions of flow speed, and should also be substantially independent of ambient temperature.

2.3.4 Temperature Balance Modes

A micromachined sensor operated in the CP-TB mode is described in [2.37]. It consists of two heating resistors and two temperature sensing resistors configured as shown in Fig. 2-7. The normalized differential heating power, $\delta P/P$, where P is the total power dissipated in the sensor, was found to be a linear function of flow speed. This result may be understood by noting that, when operated in CP mode, the flow-induced *temperature* difference δT will be a linear function of flow speed and heating power. The differential heating power will be proportional to the cancelled temperature difference, and as such, will also be a linear function of flow speed.

The 2-D sensor of Fig. 2-5 can also be operated in CP-TB mode. This requires two control loops, each driving opposing pairs of heaters, to cancel both components of the flow-induced temperature gradient. A suitable interface architecture, capable of operating the sensor in both TB modes, is described in Chapter 5. Information about the flow may now be obtained from the resulting differential heating powers δP_{ns} and δP_{ew}. These, in turn, will be proportional to the cancelled temperature differences δT_{ns} and δT_{ew}. From (2-6), the differential heating powers will be given by:

$$\frac{\delta P_{ns}}{P} = \frac{\sqrt{U_{ns}}}{E + F\sqrt{U_{ns}}} \qquad \frac{\delta P_{ew}}{P} = \frac{\sqrt{U_{ew}}}{E + F\sqrt{U_{ew}}} \tag{2-7}$$

where P is the total power dissipated in the sensor, and E and F are sensor constants. This non-square-root-law behaviour has been experimentally verified (Chapter 5).

Faster response can be obtained by operating the 2-D sensor in the CTD-TB mode. This, however, complicates the interface electronics further as it requires a third control loop to regulate the overheat. As expected from (2-3), the sensor will exhibit a square-law characteristic when operated in the CTD-TB mode (Chapter 5).

2.4 Thermal Time-of-Flight Sensors

Thermal time-of-flight sensors measure the time it takes for a heated volume of fluid to travel from a heater to a downstream temperature sensor. In principle, the relationship between the flow speed U, the measured time of flight Δt_f and the known distance Δx between the heater and the temperature sensor is given by:

$$\Delta t_f = \frac{\Delta x}{U} \quad . \tag{2-8}$$

In practice, however, significant departures from (2-8) will occur, due to the thermal time constants of the heater and the temperature sensor and the effects of heat diffusion. These effects result in the typical characteristic shown in Fig. 2-9. When compared to other classes of thermal flow sensors, time-of-flight sensors are much less sensitive to the physical properties of the fluid. Since the amplitude of the received signal is unimportant, they are also insensitive to non-idealities such as sensitivity variations, offset and drift. Despite these advantages, thermal time-of-flight sensors have not yet found widespread application. A probable

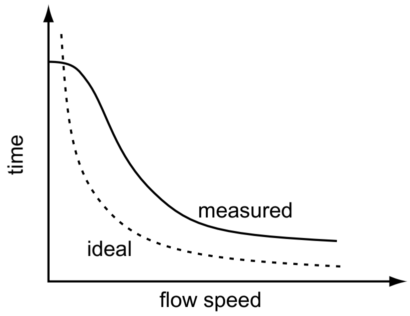

Figure 2-9 *Time of flight as a function of flow speed.*

reason for this is the relatively sophisticated signal processing required to determine the time of flight from the dispersed pulse received by the temperature sensor.

2.4.1 Examples

Thermal time-of-flight sensors typically employ the same structure as calorimetric flow sensors: two temperature-sensing resistors on either side of a heating resistor. The resistors can be mounted on a contiguous insulating substrate [2.38, 2.39] or can be mounted on bridges [2.40, 2.41, 2.42]. The use of micromachining is essential to ensure that the transport of heat takes place via the flow and not via the substrate. A detailed analysis shows that the measured time of flight will be significantly influenced by the thermal time constants of the flow-sensing elements [2.42]. Since these time constants increase as flow speed decreases, they increase the measured time of flight at low flow speeds. This can be used to mitigate the effects of heat diffusion at low speeds, and thus increase the sensor's useful operating range. Flow direction can be determined by comparing the time of flight (or the amplitude) of the heat pulses received by the two temperature sensors.

2.4.2 Operating Modes

Time-of-flight sensors may be operated in either pulsed or AC modes. In pulsed mode, a short pulse is applied to the heater and the time for the temperature sensor's output to peak is measured [2.38, 2.41]. As flow

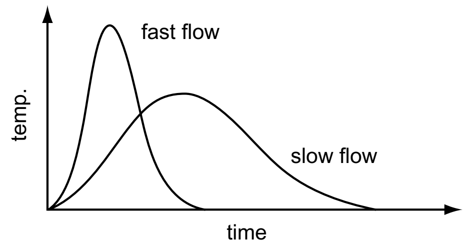

Figure 2-10 *Effects of diffusion on the received pulse in a thermal time-of-flight sensor.*

speed decreases, however, the amplitude of the received pulse will decrease while its width will increase (Fig. 2-10). This phenomenon makes it increasingly difficult to determine exactly when the peak occurs. This problem can be avoided by operating the sensor in AC mode, in which the phase difference between a sinusoidal heating signal and the output of the temperature sensor is measured [2.39, 2.42, 2.43]. Synchronous detection techniques can then be used to determine the phase shift over a wide range of flow speeds [2.42]. The main drawback of this mode is that the frequency of the heating signal must be quite low (typically in the order of a few Hertz) in order to obtain a sufficiently large signal at the temperature sensor's output [2.39]. As a result, operation in AC mode is only useful for the measurement of slowly changing flows.

Since they use the same structure, thermal time-of-flight sensors can also be configured as calorimetric flow sensors. The combination of the two measurement principles can be used to improve the sensor's accuracy and/or to increase its operating range [2.38, 2.40, 2.41].

2.5 Realization of Thermal Flow Sensors in Silicon

As can be seen from the examples in the previous sections, many thermal flow sensors have been realized in silicon. In a standard IC process, however, there are only a limited number of elements with which the heaters and temperature sensors of a thermal flow sensor can be realized. These elements are resistors, bipolar transistors, and thermocouples. The

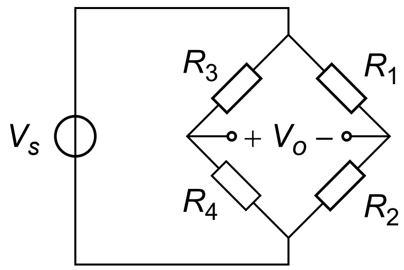

Figure 2-11 *Wheatstone bridge.*

first two can be used as heaters, while all of them can be used as temperature sensors. In this section, their characteristics will be discussed.

2.5.1 Resistors

In standard IC technology, resistors can be made of doped silicon, doped polysilicon, or interconnect metal. These resistors can be used as heaters or, by exploiting their non-zero temperature coefficients (typically a few thousand ppm/K), as temperature sensors.

Due to process spread, the accuracy of integrated resistors is poor: tolerances of a few tens of percent are typical. As a result, such resistors must be individually calibrated if they are to be used as accurate absolute-temperature sensors. However, the match between neighbouring resistors is much better: mismatch errors of a few thousand ppm are typical. To exploit this, resistors are often used in a Wheatstone bridge configuration to measure temperature differences (such as an overheat). In the configuration shown in Fig. 2-11, four identical resistors are used: R_1 and R_2 are at different temperatures T_1 and T_2, while R_3 and R_4 are at the same temperature. The output of the bridge V_o is then given by:

$$V_o = \frac{1}{4}\beta V_s(T_1 - T_2), \tag{2-9}$$

where β is the temperature coefficient of the resistors and V_s is the voltage across the bridge. For a typical β of 2000 ppm/K and a 5V supply voltage, the sensitivity of the bridge will be 2.5mV/K. Resistor mismatch will then cause temperature sensing errors of a few degrees. For greater accuracy the bridge must be trimmed, either by hand or by laser trimming. however, both methods increase fabrication costs.

In simple CP schemes, in which a heating resistor is actually driven at constant voltage (or constant current), resistance tolerance causes proportional variations in the resistor's power dissipation. These, in turn, cause variations in the sensitivity of the corresponding flow sensor. A simple method of stabilizing the dissipated power is by inserting an off-chip resistor with the same nominal resistance between the heater and a reference voltage. The variations in the heater's power dissipation will now be proportional to the *square* of its tolerance, which is good enough for most applications. However, half the power drawn from the supply will be dissipated in the reference resistor. Using active components, more efficient power control circuits have been designed [2.13, 2.44]. However, these circuits still require the use of an off-chip reference resistor.

2.5.2 Bipolar Transistors

By appropriate biasing, a bipolar transistor can be used as a heater. It can also be used as a temperature sensor because its base-emitter voltage V_{BE} depends on temperature in a predictable manner [2.45].

The collector current I_c of a bipolar transistor can be expressed as:

$$I_c = I_s \exp\left\{\frac{qV_{BE}}{kT}\right\} \tag{2-10}$$

where I_s is the saturation current, q is the electron charge, k is Boltzmann's constant and T is the absolute temperature. Then, V_{BE} is given by:

$$V_{BE} = \frac{kT}{q}\ln\left\{\frac{I_c}{I_s}\right\}. \tag{2-11}$$

Although this equation seems to imply that V_{BE} has a positive temperature coefficient, this is not the case. The reason for this is that the saturation current I_s depends strongly on temperature. If the collector current I_c is also temperature dependent (which is typical of an on-chip current) and of the form:

$$I_c \propto T^m , \tag{2-12}$$

then it can be shown [2.46] that:

$$V_{BE}(T) = V_{g0}\left\{1-\frac{T}{T_r}\right\}+\frac{T}{T_r}V_{BE}(T_r)+\frac{kT}{q}(\eta-m)\ln\left\{\frac{T}{T_r}\right\} \tag{2-13}$$

where V_{g0} is the extrapolated band-gap voltage at zero Kelvin, $V_{BE}(T_r)$ is the base-emitter voltage at a *chosen* reference temperature T_r and η is a process-dependent constant. This rather complex equation can be expressed as the sum of a constant term (V_{BE0}), a linear term (λT) and a non-linear or curvature term $c(T)$ as:

$$V_{BE}(T) = V_{BE0}-\lambda T-c(T) \tag{2-14}$$

where:

$$V_{BE0} = V_{g0}+(\eta-m)\frac{kT_r}{q} \tag{2-15}$$

$$\lambda_{BE} = \frac{V_{BE0}-V_{be}(T_r)}{T_r} \tag{2-16}$$

$$c(T) = \frac{k}{q}(\eta-m)\left(T_r-T+T\ln\frac{T}{T_r}\right). \tag{2-17}$$

For transistors realized in standard IC processes, the slope λ_{BE} has a value of about 2mV/K. Thus V_{BE} *decreases* in an almost linear manner with increasing temperature (Fig. 2-12) and thus can be used as a measure of temperature. This will be referred to as V_{BE} sensing. Due to the effects of process spread, however, the spread in $V_{BE}(T_r)$ will be in the order of

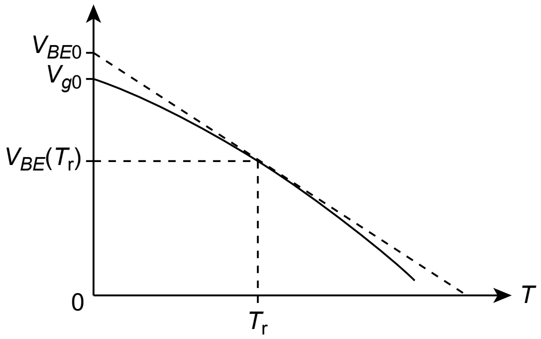

Figure 2-12 *Base-emitter voltage of a bipolar transistor as a function of temperature (the curvature is exaggerated for clarity).*

several millivolts, resulting in temperature-sensing errors of several degrees. This can be ascribed mainly to the spread in the transistor's saturation current. Many thermal flow sensors have used V_{BE} sensing as a means of determining the overheat [2.5, 2.9, 2.26]. Such circuits are usually trimmed at a known temperature, in order to compensate for the effects of process spread on V_{BE}.

A much better way of measuring absolute temperature involves measuring the *change* in V_{BE}, denoted by ΔV_{BE}, which occurs when the *same* transistor is biased at two different collector currents I_1 and I_2. This will be referred to as ΔV_{BE} sensing. Using (2-11) we obtain:

$$\Delta V_{BE} = V_{be}(I_1) - V_{be}(I_2) = \frac{kT}{q}\ln\left\{\frac{I_1}{I_2}\right\} = \lambda_{PTAT}T. \qquad (2\text{-}18)$$

This voltage is proportional to absolute temperature (PTAT) and is *independent* of process parameters. However, its temperature coefficient λ_{PTAT} is an order of magnitude less than λ_{BE} (for a collector current ratio I_1/I_2 of 8, $\lambda_{PTAT} \sim 180\mu V/K$). Despite this, temperature-sensing errors much less than a degree can be achieved by careful design of the circuitry used to measure ΔV_{BE} and define the collector current ratio [2.47, 2.48].

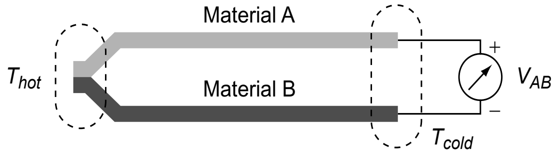

Figure 2-13 *Operating principle of a thermocouple.*

2.5.3 Thermocouples

The various conducting materials of an IC process can be used as elements of a thermocouple. As shown in Fig. 2-13, a thermocouple is created when two dissimilar conductors are connected together. In the presence of a temperature difference $\Delta T = T_{hot} - T_{cold}$, a voltage difference V_{AB} will be measured between the two free ends. This is a consequence of the Seebeck effect, which states that a temperature difference ΔT across the two ends of an electrical conductor will cause a potential difference V_s given by:

$$V_S = \alpha \Delta T \tag{2-19}$$

where α is the material's *absolute* Seebeck coefficient. This is expressed in V/K and may be either positive or negative. By convention, the sign reflects the polarity of the cold end with respect to that of the hot end. In a thermocouple two different materials are involved and so V_{AB}, known as the relative Seebeck voltage, is given by:

$$V_{AB} = (\alpha_A - \alpha_B)\Delta T \tag{2-20}$$

where α_A and α_B are the Seebeck coefficients of materials A and B respectively. The voltage difference V_{AB} may also be expressed as:

$$V_{AB} = \alpha_{AB}\Delta T \tag{2-21}$$

where $\alpha_{AB} = (\alpha_A - \alpha_B)$ is the *relative* Seebeck coefficient between the materials.

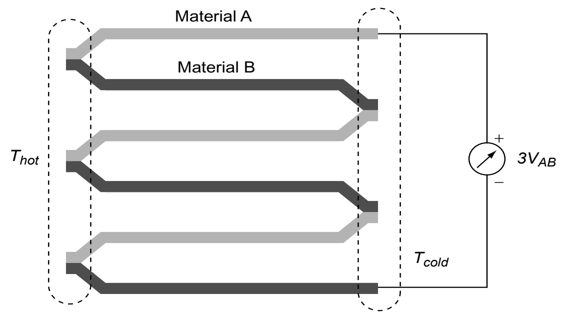

Figure 2-14 *Operating principle of a thermopile.*

Thermocouples, unlike resistors and transistors, directly measure temperature differences. Extremely small differences can be measured because they are intrinsically free of offset. This is because the Seebeck effect is a self-generating effect. In contrast, device mismatch causes significant offset when resistor or transistor pairs are used to measure temperature differences. Their lack of offset makes thermocouples ideally suited for use in flow sensors operated in TB modes.

Commonly used thermocouple materials in standard IC processes are doped silicon and polysilicon, which have *absolute* Seebeck coefficients ranging from 0.1 to 1.5mV/K. The exact value is dependent on ambient temperature, and on the material's doping level [2.49, 2.50]. As a result, the relative Seebeck coefficient of integrated thermocouples will be temperature dependent and suffer from process spread.

In order to increase the generated voltage, many thermocouples can be connected in series electrically and arranged in parallel thermally to form a thermopile. The generated voltage will then increase by a factor *N*, where *N* is the number of thermocouples. However, the electrical resistance of the thermopile will also increase by a factor *N*, leading to increased levels of Johnson noise. In addition, the thermal resistance between the hot and cold junctions will decrease by the same factor. This is an important consideration in micromachined flow sensors, where the thermopile is realized on an insulating substrate.

2.6 Conclusions

Many thermal flow sensors have been realized in silicon. This is because they have no moving parts, are compatible with IC technology and can operate through a thin protective substrate (since they only need to be in thermal contact with the fluid). Their main disadvantages are a non-linear response, which is dependent on the sensor's geometry and on the physical properties of the fluid.

Thermal flow sensors can be grouped into three main classes: thermal anemometers, calorimetric flow sensors, and thermal time-of-flight sensors. Thermal anemometers operate by measuring the total heat loss, while calorimetric flow sensors operate by measuring differential heat loss. Thermal time-of-flight sensors measure the time it takes for a heat pulse to travel a known distance, however, they are not widely used due to the relative complexity of the required signal processing.

The input-output characteristic of a thermal flow sensor will be significantly influenced by the mode in which it is operated. Thermal anemometers can be operated in either constant power (CP) or constant temperature difference (CTD) modes. Operation in CTD mode is to be preferred, since the use of a feedback loop to regulate the overheat reduces the response time and improves the accuracy of the overall system. Calorimetric flow sensors can be operated in *four* different modes, since both the overheat *and* a flow-induced temperature gradient can be regulated or measured. However, most reported sensors have been operated in a temperature gradient (TG) mode, in which the flow-induced gradient is measured. The sensor is then operated in either CP or CTD modes. In general, operation in CTD mode is to be preferred since it increases the useful operating range and reduces the response time, at the expense of an extra control loop. Improved accuracy can be obtained by operating the sensor in the so-called temperature balance (TB) mode, in which the flow-induced temperature gradient is cancelled (regulated) by a control loop. Best performance is obtained by combining the CTD and TB modes, i.e., by operating the sensor in the CTD-TB mode.

The temperature sensors of a thermal flow sensor can be readily realized in silicon; resistors, bipolar transistors and thermopiles can be used.

Resistors are easily realized, but will usually require trimming due to their limited accuracy. Using ΔV_{be} sensing, bipolar transistors can be used as accurate absolute-temperature sensors, at the expense of reduced sensitivity. On-chip temperature differences can best be measured with thermopiles, due to their offset-free nature.

2.7 References

[2.1] B.W. van Oudheusden "Silicon thermal flow sensors," *Sensors and Actuators A: Physical*, vol. 30, no. 1-2, pp. 5-26, Jan. 1992.

[2.2] M. Elwenspoek and R. Wiegerink, "Mechanical Microsensors, Berlin, Springer-Verlag, 2001.

[2.3] L.V. King, "On the convection of heat from small cylinders in a stream of fluid," *Philosophical Transactions of the Royal Society (London) A*, vol. 214, pp. 373-432, 1914.

[2.4] F. Mailly et. al., "Anemometer with hot platinum thin film," *Sensors and Actuators A: Physical*, vol. 94, no. 1-2, pp. 32-38, Oct. 2001.

[2.5] R. Kersjes, F. Liebscher, E. Spiegel, Y. Manoli and W. Mokwa, "An invasive catheter flow sensor with on-chip CMOS read-out electronics for the on-line determination of blood flow," *Sensors and Actuators A: Physical*, vol. 54, no. 1-3, pp. 563 - 567, June 1996.

[2.6] C.F. Wilson, "The measurement of wind on the surface of Mars," Ph.D. Thesis, Linacre College, Oxford University, 2003.

[2.7] T. Ebefors, E. Kalvesten and G. Stemme, "Three dimensional silicon triple-hot-wire anemometer based on polyimide joints," *Proc. of MEMS 1998*, pp. 93-98, 1998.

[2.8] T. Neda, K. Nakamura and T. Takumi, "A polysilicon flow sensor for gas flow meters," *Sensors and Actuators A: Physical*, vol. 54, no. 1-3, pp. 626-631, June 1996.

[2.9] M. Domínguez, F. Masana, V. Jimenez, S. Bermejo, J. Amirola, J. Ballester, N. Fueyo and L. Castañer, "Low-cost thermal TΣΔ airflow sensor," *IEEE Sensors Journal*, vol. 2, no. 5, pp. 453–462, October 2002.

[2.10] L. Castañer, V. Jimenez, M. Domínguez, F. Masana and A. Rodriguez, "A conduction-convection design for liquid flow sensing," *Sensors and Actuators A: Physical*, vol. 66, no. 1-3, pp. 131-137, April 1998.

[2.11] A.J. van der Wiel, C. Linder, N.F. de Rooij and A. Bezinge, "A liquid velocity sensor based on the hot-wire principle," *Sensors and Actuators A: Physical*, vol. 37, no. 8, pp. 693-697, Jun.-Aug. 1993.

[2.12] L.E. MacHattie, "The transistor as an anemometer," *Journal of Physics E: Scientific-Instruments*, vol. 12, no. 8, pp. 754-760, Aug. 1979.
[2.13] S.S.W. Chan and P.C.H. Chan, "A resistance-variation-tolerant constant-power heating circuit for integrated sensor applications," *IEEE J. of Solid-State Circuits*, vol. 34, no. 4, April 1999.
[2.14] Q. Huang, C. Menolfi and C. Hammerschmied, "A MOSFET-only interface for integrated flow sensors," *Proc. of ISCAS '96*, vol. 4, pp. 372-375, 1996.
[2.15] B.W. van Oudheusden, "Effect of operating conditions on the dynamic response of thermal sensors with and without analog feedback," *Sensors and Actuators A: Physical*, vol. 58, no. 2, pp. 129 -135, Feb. 1997.
[2.16] F. Mayer, O. Paul and H. Baltes, "Influence of design geometry and packaging on the response of thermal CMOS flow sensors," *Digest of Transducers '95*, vol. 1, pp. 548-551, June 1995.
[2.17] F. Mayer, G. Salis, J. Funk, O. Paul and H. Baltes, "Scaling of thermal CMOS gas flow microsensors: experiment and simulation," *Proc. of MEMS '96*, pp. 116-121, Feb. 1996.
[2.18] R.G. Johnson and R.E. Higashi, "A highly sensitive silicon chip micro transducer for airflow and differential pressure sensing applications," *Sensors and Actuators A: Physical*, vol. 11, no. 1, pp. 63-72, Jan. 1987.
[2.19] T.R. Ohnstein et al., "Environmentally rugged, wide dynamic range microstructure airflow sensor," *Proc. of the IEEE Solid-State Sensor and Actuator Workshop*, pp. 158-160, 1990.
[2.20] A. Glaninger, A. Jachimowicz, F. Kohl, R. Chabicovsky and G. Urban, "Wide range semiconductor flow sensors," *Sensors and Actuators A: Physical*, vol. 85, no. 1-3, pp. 139-146, August 2000.
[2.21] F. Mayer, A. Haberli, H. Jacobs, G. Ofner, O. Paul and H. Baltes, "Single-chip CMOS anemometer," *Digest of IEDM 1997*, pp. 895-898, Dec. 1997.
[2.22] F. Mayer, M. Hintermann, H. Jacobs, O. Paul, H. Baltes, "Thermoelectric CMOS anemometers," Proc. SPIE: Micromachined devices and components II, vol. 2882, pp. 236-246, 1996.
[2.23] S. Oda, M. Anzai, S. Uematsu and K. Watanabe, "A silicon micromachined flow sensor using thermopiles for heat transfer measurements," *IEEE Trans. Instr. and Meas.*, vol. 52, no. 4, pp. 1155-1159, Aug. 2003.
[2.24] H.-E. de Bree, H.V. Jansen, T.S.J. Lammerink, G.J.M. Krijnen, M. Elwenspoek, "Bi-directional fast flow sensor with a large dynamic range," *J. Micromech. Microeng.*, vol. 9, no. 2, pp. 186-189, June 1999.
[2.25] B.W. van Oudheusden, "Integrated silicon flow sensors," Ph.D. Thesis, Delft University of Technology, 1989.

[2.26] B.W. van Oudheusden and J.H. Huijsing, "An electronic wind meter based on a silicon flow sensor," *Sensors and Actuators A: Physical*, vol. 22, no. 1-3, pp. 420-424, March 1990.
[2.27] K.A.A. Makinwa, A. Hagedoorn and J.H. Huijsing, "Industrial design of a solid-state wind sensor," *Proc. of SiCon 2001*, pp. 68 - 71, Nov. 2001.
[2.28] B.W. van Oudheusden and J.H. Huijsing, "The thermal modelling of a flow sensor based on differential convective heat transfer," *Sensors and Actuators A: Physical*, vol. 29, no. 2, pp. 93-106, Nov. 1991.
[2.29] B.W. van Oudheusden, "Silicon thermal flow sensor with a two-dimensional direction sensitivity," *Measurement Science and Technology*, vol. 1, no. 7, pp. 565-575, July 1990.
[2.30] B.W. van Oudheusden and A.W. van Herwaarden, "High-sensitivity 2-D flow sensors with an etched thermal isolation structure," *Sensors and Actuators A: Physical*, vol. 22, no. 1-3, pp. 425-430, March 1990.
[2.31] J. Robadey, O. Paul and H. Baltes, "Two-dimensional integrated gas flow sensors by CMOS IC technology," *J. Micromech. Microeng.*, vol. 5, no. 3, pp. 243-250, Sept. 1995.
[2.32] E. Yoon and K.D. Wise, "An integrated mass-flow sensor with on-chip CMOS interface circuitry," *IEEE Trans. on Electron Devices*, vol. 39, no. 6, pp. 1376-1386, June 1992.
[2.33] M. A. Mullins, A. F. P. Van Putten, R. Bayford and J. B. Butcher, "Potential for a smart sensor based on an integrated silicon anemometer," *Sensors and Actuators A: Physical*, vol. 47, no. 1-3, pp. 342-348, Mar.-Apr. 1995.
[2.34] T.S.J. Lammerink, N.R. Tas, G.J.M. Krijnen and M. Elwenspoek, "A new class of thermal flow sensors using $\Delta T = 0$ as a control signal," *Proc. of MEMS 2000*, pp. 525-530, Jan. 2000.
[2.35] K.A.A. Makinwa and J.H. Huijsing, "A wind sensor interface using thermal sigma-delta modulation," *Proc. of Eurosensors XIV*, pp. 249 - 252, Sept. 2000.
[2.36] T.S.J. Lammerink, N.R. Tas, M. Elwenspoek and J.H.J. Fluitman, "Micro-liquid flow sensor," *Sensors and Actuators A: Physical*, vol. 37-38, pp. 45-50, June-Aug. 1993.
[2.37] T.S.J. Lammerink, R.J. Wiegerink and M. Elwenspoek, "Temperature-balance micro flow sensor system based on a free oscillating differential power controller," in *Sensor Technology 2001*, Kluwer Academic Publishers, pp. 19-24, 2001.
[2.38] M. Ashauer et al., "Thermal flow sensor for liquids and gases based on the combination of two principles," *Sensors and Actuators A: Physical*, vol. 73, no. 1-2, pp. 7-13, March 1999.

[2.39] G. Bedo, H. Fannasch and R. Muller, "A silicon flow sensor for gases and liquids using AC measurements," *Sensors and Actuators A: Physical*, vol. 85, no. 1-3, pp. 124-132, Aug. 2000.

[2.40] T.S.J. Lammerink, F. Dijkstra, Z. Houkes and J. van Kuijk, "Intelligent gas-mixture flow sensor," *Sensors and Actuators A: Physical*, vol. 47, no. 1-3, pp. 380-384, March-April 1995.

[2.41] E. Meng and Y.-C. Tai, "A parylene MEMS flow sensing array," *Digest of Transducers '03*, pp. 686-689, June 2003.

[2.42] F. Durst, A. Al-Salayameh and J. Jovanovic, "Theoretical and experimental investigations of a wide-range thermal velocity sensor," *Measurement Science and Technology*, vol. 12, no. 3, pp. 223-237, March 2001.

[2.43] C.Q. Yang and H. Soeberg, "Monolithic flow sensor for measuring millilitre per minute liquid flow," *Sensors and Actuators A: Physical*, vol. 33, no. 3, pp. 143-153, June 1992.

[2.44] H.-J Verhoeven, "Smart thermal flow sensors," Ph.D. Thesis, Delft University of Technology, 1996.

[2.45] T.C. Verster, "P-N junction as an ultralinear calculable thermometer," *Electronics Letters*, vol. 4, no. 9. pp. 175-6, May 1968.

[2.46] G.C.M. Meijer, R. van Gelder, V. Nooder, J. van Drecht and H. Kerkvliet, "A three-terminal integrated temperature transducer with microcomputer interfacing," *Sensors and Actuators A: Physical*, vol. 18, no. 2, pp. 195-206, June 1989.

[2.47] M.A.P. Pertijs and J.H. Huijsing, "Transistor temperature measurement for calibration of integrated temperature sensors," *Proc. of IMTC 2002*, vol. 1, pp. 755-758, May 2002.

[2.48] M.A.P. Pertijs, G.C.M. Meijer and J.H. Huijsing, "Precision temperature measurement using CMOS substrate PNP transistors, *IEEE Sensors Journal*, vol. 4, no. 3, pp. 294-300, June 2004.

[2.49] A.W. van Herwaarden and P.M. Sarro, "Thermal sensors based on the Seebeck effect," *Sensors and Actuators A: Physical*, vol. 10, no. 3-4, pp. 321-346, Nov.-Dec. 1986.

[2.50] O. Paul, M. von Arx and H. Baltes, "Process-dependent thermophysical properties of CMOS IC thin films," *Digest of Transducers '95*, vol. 1, pp. 178-181, June 1995.

Thermal Sigma-Delta Modulators 3

Thermal sigma-delta (TΣΔ) modulators are sigma-delta modulators whose input signals and summing nodes are in the thermal domain. Like their better known electrical counterparts, TΣΔ modulators employ oversampling and noise-shaping techniques to accurately digitize an analog signal, in this case heat flow, with relatively simple circuitry. A major difference, however, is that the loop filter of a TΣΔ modulator incorporates the passive low-pass filter formed by the intrinsic thermal inertia of the summing node. In many cases, this filter is the only one required, a characteristic that greatly simplifies the realization of such modulators, but also limits their performance. Performance can be improved by augmenting the thermal filter with an electrical filter, or by using a multi-bit quantizer. TΣΔ modulators have been used mainly to read out thermal flow sensors, in which application they provide a digital representation of the sensor's flow-dependent heat loss. In this chapter, the properties of TΣΔ modulators will be discussed in detail.

3.1 Single-Ended Thermal Sigma-Delta Modulators

The topology of a single-ended TΣΔ modulator is shown in Fig. 3-1. It consists of a clocked comparator (a comparator and a flip-flop) and a heated thermal mass, whose temperature T_s is monitored by a temperature sensor. Simply put, the modulator attempts to keep the thermal mass at a reference temperature T_{ref} by heating it with pulses derived from its bitstream output *bs*. In order to do this, the comparator periodically compares T_s with T_{ref}. If $T_s < T_{ref}$ the comparator output $bs = 1$, which

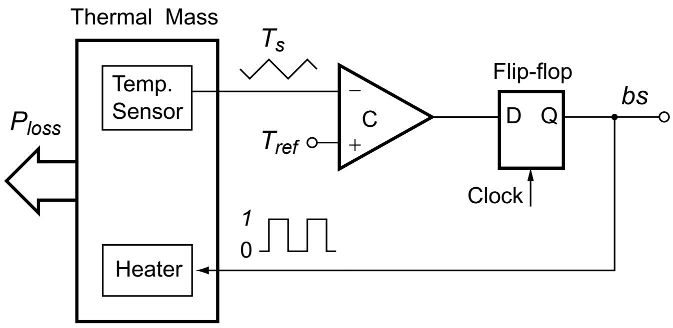

Figure 3-1 *Implementation of a single-ended TΣΔ modulator.*

implies that the thermal mass will be heated with a constant power P_{ref}. However, if $T_s > T_{ref}$ then $bs = 0$, and the thermal mass will be cooled by its heat loss P_{loss} to the surroundings. In this way, the thermal mass will be heated by a stream of heat pulses. These will be low-pass filtered by its thermal inertia, and so T_s will fluctuate around the set point T_{ref}. If the clock frequency is much higher than the bandwidth of the thermal low-pass filter, then $T_s \sim T_{ref}$. In this case, the average power dissipated in the thermal mass will compensate for P_{loss}, and so the bitstream average μ is proportional to P_{loss}/P_{ref}.

The modulator's block diagram may be redrawn to show the two functions of the thermal mass, i.e., summing and filtering, more explicitly. The resulting topology (Fig. 3-2) is functionally identical to that of a single-loop low-pass ΣΔ modulator. The clocked comparator is a 1-bit ADC, and the transition between the thermal and electrical domains is made via the temperature sensor and the heater, which functions as a 1-bit DAC.

Due to the presence of the thermal low-pass filter, the quantization noise introduced by the comparator will be shaped away from DC. By oversampling P_{loss}, i.e., by choosing a clock frequency much higher than the bandwidth of the thermal low-pass filter, the quantization noise in the signal band can be made very small. High-resolution information about P_{loss} can then be obtained by decimating the modulator's bitstream output.

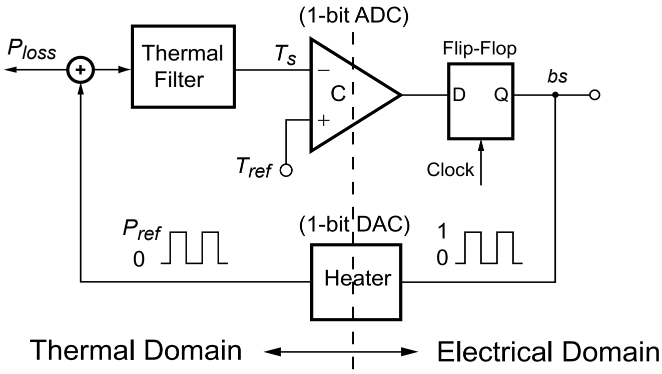

Figure 3-2 *Block diagram of a single-ended TΣΔ modulator.*

The TΣΔ modulator was first proposed in 1989 as an improvement on the thermal duty-cycle modulator [3.1]. This has essentially the same topology as Fig. 3-1, except that the comparator is *not* clocked [3.2, 3.3]. The result is a free-running oscillator, whose duty cycle will be a function of heat loss. Since the output of a duty-cycle modulator is a binary signal, it can be connected directly to a microprocessor. However, it is an asynchronous signal, which means that it must be oversampled at a significantly higher clock frequency in order to accurately determine the duty cycle. Another drawback of the duty-cycle modulator is its tendency to lock on to periodic interference, e.g. from neighbouring digital circuitry. Both these drawbacks are eliminated in a TΣΔ modulator, because the comparator is *clocked*.

Since the TΣΔ modulator of Fig. 3-2 digitizes the total heat loss of the thermal mass, it has been used to interface thermal anemometers for gases [3.4–3.8] and liquids [3.9–3.11]. The main attraction of this topology for such applications is its simplicity. Apart from a heater and a temperature sensor, which are already present in the flow sensor, the only other required component is a clocked comparator. Furthermore, the modulator ensures that on average, the sensor's temperature is kept constant, i.e., that the sensor is operated in CTD mode (Section 2.2.2), which results in improved response times [3.12].

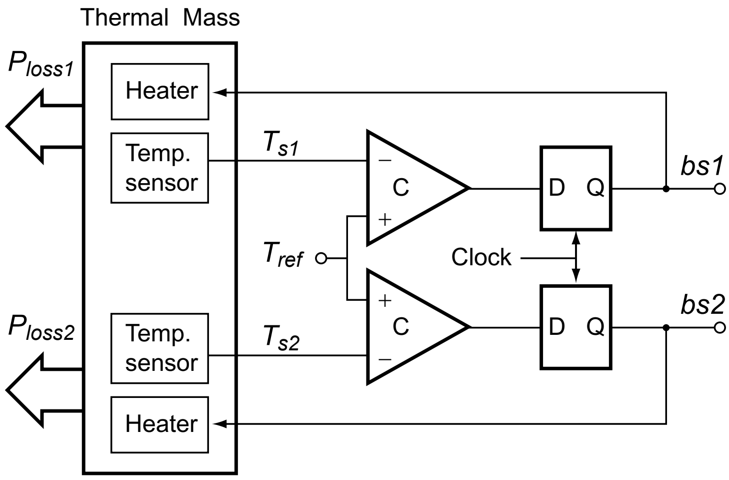

Figure 3-3 *Differential heat loss measurement using two TΣΔ modulators.*

3.2 Differential Thermal Sigma-Delta Modulators

In a calorimetric flow sensor, the parameter of interest is the sensor's differential heat loss δP, which is a function of flow speed and direction. As was suggested in [3.7, 3.13], this can be determined by heating the sensor's thermal mass with two TΣΔ modulators configured as shown in Fig. 3-4, in which case $\delta P = P_{loss1} - P_{loss2}$. The main problem with this approach, however, is that due to temperature-sensor mismatch, $T_{s1} \neq T_{s2}$. This temperature offset will cause heat flow in the thermal mass, which, in turn, will introduce a significant offset in the measured δP.

A better method of digitizing differential heat loss is to use the *differential* TΣΔ modulator shown in Fig. 3-4. The modulator drives two heaters in anti-phase such that the temperature difference δT is cancelled, thus compensating for the differential heat loss, δP. The thermal mass will still function as a thermal low-pass filter, and so $\delta T \sim 0$, provided the clock frequency is high enough. The modulator's bitstream output will then be a digital representation of the differential heat loss. Compared to the topology of Fig. 3-3, only half the circuitry is required. Moreover, the

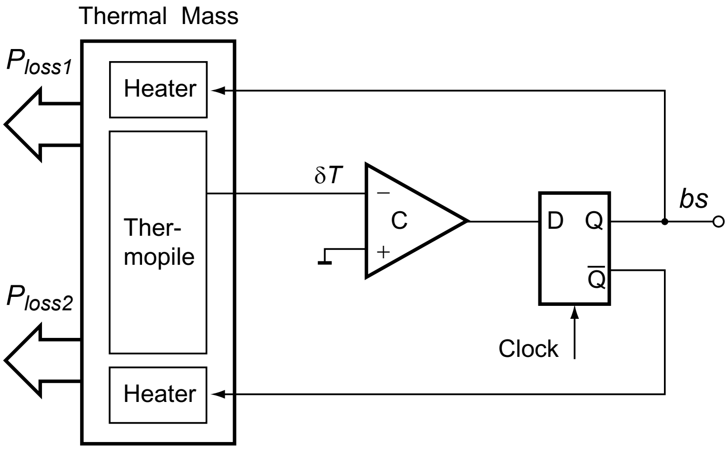

Figure 3-4 *Block diagram of a differential TΣΔ modulator.*

differential temperature measurement can be made with a thermopile, which is intrinsically offset free. Since the thermopile is only used as a null detector, no demands are made on its (process-dependent) linearity and sensitivity.

The differential TΣΔ modulator was first described in [3.14], where it was used to read out a two-dimensional thermal flow sensor. A smart wind sensor employing two differential modulators integrated on the same chip as the flow sensor is described in Chapter 5. By removing the flip-flop in Fig. 3-4, a differential duty-cycle modulator can be realized [3.15, 3.16]. However, this modulator suffers from the same drawbacks as conventional duty-cycle modulators, namely an asynchronous output signal and sensitivity to periodic interference.

3.3 Thermal Filters

The behaviour of a TΣΔ modulator, like that of an electrical ΣΔ modulator, will mainly be determined by the properties of its loop filter. Since this will usually be a *thermal* filter, a brief review of the properties of thermal filters will be presented in this section.

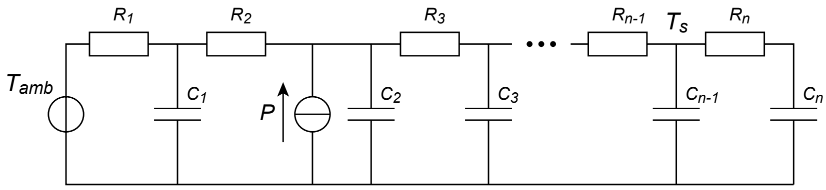

Figure 3-5 *One-dimensional thermal model of a physical structure.*

Using the well-known analogy between the thermal and electrical domains (summarised in Table 3-1), the thermal behaviour of any physical structure can be modelled by subdividing it into a large number of finite elements and then assigning a thermal resistance and capacitance to each element [3.14].

Table 3-1 *Electrical equivalents of thermal parameters*

Thermal Parameter	**Units**	**Electrical Parameter**	**Units**
Temperature	K	Voltage	V
Heat flow	W	Current	A
Heat	J = Ws	Charge	C = As
Resistance	K/W	Resistance	Ω = V/A
Capacitance	J/K	Capacitance	F = As/V

For simplicity, this is illustrated in Fig. 3-5 for a one-dimensional structure, but it can be extended to two- and three-dimensional structures. The voltage source T_{amb} models the ambient temperature. The transfer function Z_{th} relating the power P dissipated at one point in the structure and the temperature T_s measured at some other point, will then be a passive RC impedance. Besides passivity, an added constraint on such filters is the fact that all thermal capacitances have one terminal at ambient temperature, or in other words, floating capacitances do not exist in the thermal domain.

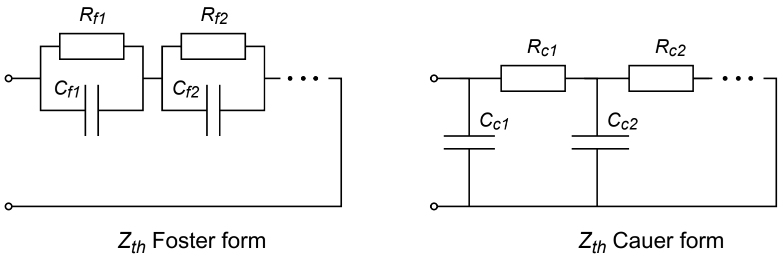

Figure 3-6 *Equivalent realizations of an RC driving-point impedance Z_{th}.*

3.3.1 RC Driving-Point Impedances

If the point at which the structure is heated is the same as the point where the temperature rise is measured, $Z_{th}(s)$ will be a so-called RC driving-point impedance. From basic network theory [3.18, 3.19], such an impedance is a positive real function of s ($= j\omega$) and has the following properties:

- *its poles and zeros are simple and lie on the negative real axis*
- *the residues of the poles are real and positive*
- *its poles and zeros alternate along the negative real axis*
- *the singularity nearest to the origin must be a pole while the singularity nearest to infinity must be a zero*

The first two properties imply that Z_{th}(s) may be expressed as:

$$Z_{th}(s) = \frac{K_1}{(s+\sigma_1)} + \frac{K_2}{(s+\sigma_2)} + \dots \tag{3-1}$$

where both σ_i and K_i are real and positive. From (3-1), Z_{th}(s) can be modelled by connecting a number of RC sections in series (Fig. 3-6); this is known as a Foster network [3.18]. It should be stressed, however, that since floating capacitors do not exist in the thermal domain, this network does not correspond to a physical realization [3.20]. Viewed from the input, however, this network behaves in exactly the same way as the equivalent ladder network (Fig. 3-6), which is known as a Cauer network [3.18], and *does* have a physical meaning. The third and fourth properties, coupled with the fact that floating thermal capacitors do not exist, mean that $Z_{th}(\omega)$ must have a low-pass character with, at most, a first-order roll-off, and thus a -90^{o} phase at high frequencies.

3.3.2 RC Transfer Impedances

In general, the temperature-sensing node will not be the same as the heated node. In this case, Z_{th} will be an RC transfer impedance. Again, from basic network theory [3.18, 3.19], it can be shown that the key properties of such an impedance are as follows:

- *its poles lie on the negative real axis*
- *the residues of the poles are real but can be either positive or negative*
- *the location of the zeros is arbitrary*

The first two properties imply that $Z_{th}(s)$ may again be expressed by (3-1), except that now the residues may be positive as well as negative. By grouping the positive terms together and doing the same with the negative terms, $Z_{th}(s)$ may be expressed as:

$$Z_{th}(s) = Z_{thp}(s) - Z_{thn}(s) \tag{3-2}$$

where $Z_{thp}(s)$ and $Z_{thn}(s)$ are the impedances corresponding to the positive and negative terms in (3-1), respectively [3.21]. The corresponding model for $Z_{th}(s)$ is shown in Fig. 3-7. The important thing to note is that since both these impedances will now have positive residues, they are driving-point impedances. As a result, both of them will be low-pass functions with a first-order roll-off at high frequencies, which implies that at these frequencies, the phase of $Z_{th}(s)$ will be bounded either by $+90^{o}$ (for a high-pass roll-off) or by -90^{o} (for a low-pass roll-off).

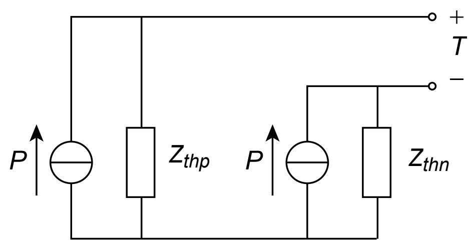

Figure 3-7 *Model of an RC transfer impedance $Z_{th} = T/P$.*

3.4 Properties of Thermal Sigma-Delta Modulators

The fact that thermal filters are essentially passive RC filters means that their poles must be on the negative real axis, which, in turn, severely limits the range of loop filters that can be realized. In addition, all thermal filters will be somewhat "leaky," since a thermal capacitance cannot be completely isolated from its surroundings. In this section, the consequences of these properties on the behaviour of TΣΔ modulators will be discussed.

3.4.1 Loop filter is a Single-Pole Impedance

The simplest useful model of a thermal mass consists of a thermal resistance R_{th} and a capacitance C_{th}. A block diagram of the corresponding TΣΔ modulator is shown in Fig. 3-8. The comparator is clocked at a frequency f_s and its output $bs \in \{0, 1\}$. Denoting the sensor's temperature at the n-th clock instant by $T_s(n)$; the operation of the modulator can be described by the following difference equation:

$$T_s(n) = p \cdot T_s(n-1) + g \cdot (x - Q(T_s(n-1))) \tag{3-3}$$

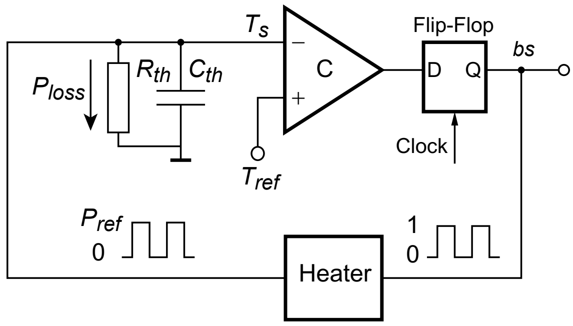

Figure 3-8 *Simplified block diagram of a* TΣΔ *modulator.*

where the constant parameters p and g are given by:

$$\begin{aligned} p &= \exp(-1/(f_s R_{th} C_{th})) \\ g &= R_{th} P_{ref}(1 - \exp(-1/(f_s R_{th} C_{th}))) \end{aligned}, \tag{3-4}$$

$Q(T)$ is a quantizer with a unipolar output:

$$Q(T) = \begin{cases} 0, & T < 0 \\ 1, & T \geq 1 \end{cases}, \tag{3-5}$$

and the modulator's *effective* input signal x is:

$$x = \frac{T_{ref}}{R_{th} P_{ref}}. \tag{3-6}$$

The discrete-time circuit corresponding to (3-3) is shown in Fig. 3-9. It may be recognized as being a first-order ΣΔ modulator with a leaky integrator. The parameter p, where $0 < p \leq 1$, quantifies the degree of integrator leakage, and is equal to one if the integrator is ideal. Since the gain, g, is in series with an ideal quantizer, the dynamics of (3-3) will depend solely on the value of p.

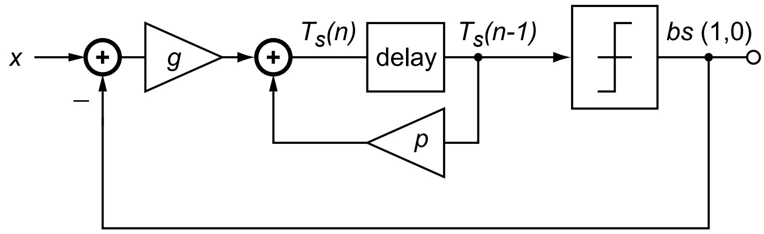

Figure 3-9 *Equivalent discrete-time model of a* TΣΔ *modulator.*

The relationship between the input signal x of the discrete-time model and the continuous-time heat loss P_{loss} (Fig. 3-8) may be obtained by noting that $T_s \sim T_{ref}$ if the clock frequency is high enough. Substituting this into (3-6) yields $x \sim P_{loss}/P_{ref}$, i.e., x corresponds roughly to a normalized version of P_{loss}.

Since P_{loss} will typically be a quasi-static signal, it is of interest to study the modulator's DC transfer function, i.e., the relationship between a DC input x and the bitstream average μ. This has been analytically studied in [3.22], where it is shown that for $p < 1$, the DC transfer function will have a fractal "staircase" structure. This is illustrated in Fig. 3-10 for p = 0.8 and p = 0.99. The steps in the DC transfer function reflect the fact that a modulator with a leaky integrator will generate the *same* sequence of bits for a range of input values. The steps therefore represent a fundamental loss of resolution. This is in contrast with the behaviour of an ideal modulator, which generates a *unique* sequence of bits for every input value. As p approaches 1, the step widths tend towards zero, and the DC transfer function tends towards the ideal straight line. The widest step, and hence the greatest loss of resolution, occurs in the middle of the DC transfer function (when μ = 0.5), and its width, Δx_{max}, is given by:

$$\Delta x_{max} = \frac{(1-p)}{(1+p)}. \tag{3-7}$$

When $f_s R_{th} C_{th} \gg 1$, i.e., when the clock frequency is much larger than the filter's cut-off frequency, $\Delta x_{max} \sim 1/(f_s RC)$. In other words, the

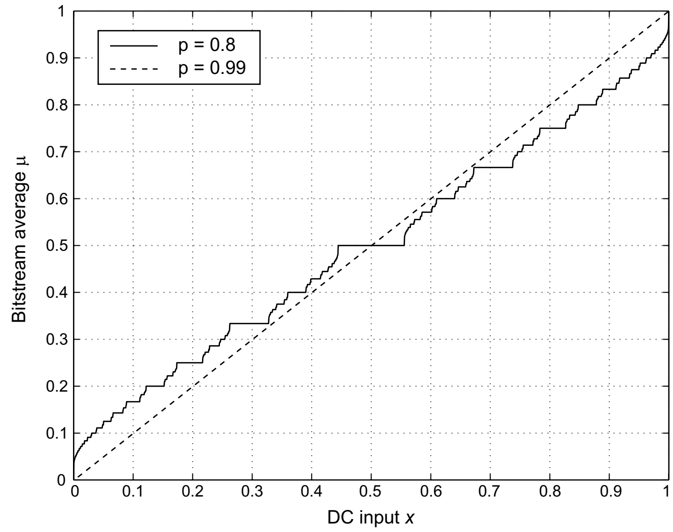

Figure 3-10 *DC transfer function of a TΣΔ modulator.*

modulator's resolution increases with clock frequency. Furthermore, noting that the DC gain A_{DC} of a leaky integrator is *finite* and is given by:

$$A_{DC} = \frac{1}{(1-p)} \sim f_s R_{th} C_{th}, \tag{3-8}$$

then the maximum step width may be expressed as $\Delta x_{max} \sim 1/(2A_{DC})$. This is the basis of the well-known rule of thumb in ΣΔ modulator design which states that the DC gain of the loop filter should be at least equal to the reciprocal of the desired resolution [3.23].

It can also be shown that Δx_{max} is proportional to the amplitude of T_s when $\mu = 0.5$ and the modulator's bitstream output is the sequence "101010..." (see appendix). Thus, increased modulator resolution can only be attained by *decreasing* the amplitude of the comparator's input signal, which, in turn, places greater demands on its resolution.

A further consequence of integrator leakage is a small gain error. In Fig. 3-10, this can be seen as a difference between the centre of each step and the ideal straight line characteristic. However, for $p \sim 1$ the gain error is linear over most of the range [3.22], and can easily be compensated for after decimation.

3.4.2 Loop Filter is a Driving-Point Impedance

In general, a driving-point impedance will have more than one pole, in which case it can be modelled by the generalized Foster network of Fig. 3-6. Since the phase of a *thermal* driving-point impedance is bounded by 0 and -90^{o}, the resulting modulator will be unconditionally stable. It can be shown (see appendix) that its DC transfer function will also have a staircase structure. This is a direct consequence of the fact that the output of the loop filter T_s is a weighted sum of the temperature across a number of leaky integrators. The corresponding difference equation is:

$$T_s(n) = \sum [p_i \cdot T_i(n-1) + g_i \cdot (x - Q(T_s(n-1)))] \qquad (3\text{-}9)$$

where T_i is the temperature across the i-th section of the Foster network, and g_i and p_i are their corresponding parameters. The largest step in the DC transfer function occurs when the bitstream average $\mu = 0.5$ and its width is given by:

$$\Delta x_{max} = \frac{\sum g_i/(1+p_i)}{\sum g_i/(1-p_i)} \qquad (3\text{-}10)$$

As for the one-pole case, the resolution of the modulator will increase with clock frequency, and will be proportional to the amplitude of the comparator's input signal if $\mu = 0.5$.

In conclusion, a TΣΔ modulator whose loop filter is a driving-point impedance will *always* be stable, and is thus robust to the physical dimensions of the thermal mass. However, its DC transfer function will have a staircase structure and exhibit a gain error. For a given filter, the width of the steps can *only* be reduced by increasing the clock frequency. This will improve resolution, but at the expense of a decrease in the amplitude of the comparator's input signal. Circuit non-idealities such as finite comparator gain and electrical crosstalk will then limit the highest practical clock frequency and, in consequence, the modulator's maximum attainable resolution.

3.4.3 Loop Filter is a Transfer Impedance

For a TΣΔ modulator whose loop filter is a transfer impedance, no analytical description of the DC transfer function is known. However, a few general observations may be made. Firstly, for both the single-ended and differential topologies, the loop filter will have a low-pass roll-off, which implies that its phase will tend to -90° at high frequencies (Section 3.3.2). As a result, both topologies will be stable at sufficiently high clock frequencies. Secondly, since a transfer impedance can be modelled by RC sections (Section 3.3.2), the modulator's DC transfer function will have a staircase structure. Modulator resolution can only be increased by increasing the clock frequency. Thirdly, since the constraints on the pole and zero locations of transfer impedances are more relaxed than those on driving-point impedances, more complex filters, with better noise-shaping characteristics, can be realized.

3.5 Thermal Sigma-Delta Modulator Topologies with Enhanced Performance

The resolution of the TΣΔ modulators discussed so far can only be increased by increasing the clock frequency. However, for a given modulator the clock frequency will usually be limited to some maximum by practical considerations, which, in turn, limits the attainable resolution. Further increases in modulator resolution will then require architectural modifications similar to the ones used in *electrical* ΣΔ modulators, such as the use of higher-order loop filters or multi-bit quantizers. These modifications will be discussed in this section.

3.5.1 Higher-Order Loop Filters

Viewed in the frequency domain, the non-linearity of the DC transfer function of a TΣΔ modulator can be regarded as a consequence of the thermal loop filter's finite DC gain. From this point of view, increasing its

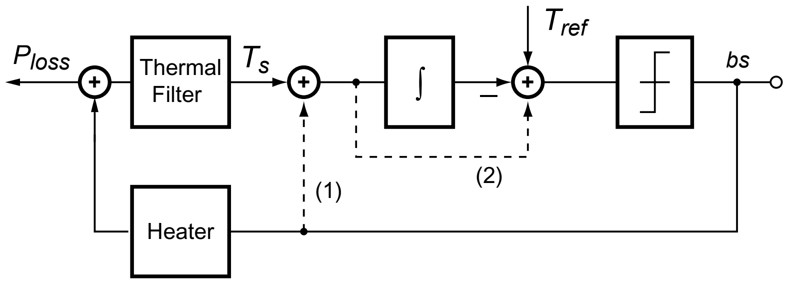

Figure 3-11 *Block diagram of a TΣΔ modulator with an electro-thermal loop filter.*

gain, for instance by increasing the clock frequency, will improve modulator linearity. Another way of increasing the loop filter's DC gain is by inserting an *electrical* integrator in cascade with the thermal filter, as shown in Fig. 3-11. The resulting electro-thermal loop filter has a very high (theoretically infinite) DC gain, which will eliminate the non-linearity of the modulator's DC transfer function. A similar topology has been used to interface a thermal rms converter [3.24, 3.25]

Due to the presence of the integrator, the loop filter will exhibit a second-order roll-off at high frequencies. In principle, the modulator will not become unstable, since the phase of the thermal filter only tends to, but never reaches, -90^{o}. In practice, the presence of other, parasitic, phase shifts may cause instability. In such circumstances, stability can be guaranteed by ensuring that the loop filter has a first-order roll-off at frequencies near $f_s/2$. This can be achieved by adding an extra feedback path (dotted path (1) in Fig. 3-11), or by adding an extra feedforward path (dotted path (2) in Fig. 3-11). These extra feedback paths can also be used to improve the modulator's transient response [3.26, 3.27].

3.5.2 Multi-Bit Quantizers

Another way of increasing the resolution of a ΣΔ modulator is by increasing the resolution of the quantizer (and the thermal DAC in the feedback loop). The dynamics of a first-order modulator with a leaky integrator and an *m*-level quantizer have been investigated in [3.28]. There it is shown that the modulator's DC transfer function will also have a fractal staircase structure, but that the step widths will be reduced by a factor $m - 1$, compared to those resulting from the use of a one-bit quantizer.

The required multi-bit DAC can be simply realized by dividing the heater into a number of segments, or by driving a single heater with an electrical DAC. However, the realization of a multi-bit quantizer for a TΣΔ modulator is a much more difficult task. This is because the sensitivity of typical temperature sensors, e.g. bipolar transistors and thermopiles, is at the millivolt/Kelvin level, which, in turn, means that the quantization levels will usually be at the microvolt level. In addition, due to the finite DC gain of the thermal loop filter, quantizer non-linearity will impact the performance of the modulator. However, given the growing availability of high-resolution smart temperature sensors [3.29], TΣΔ modulators which use such sensors as multi-bit quantizers may be readily implemented at the system level [3.4, 3.7].

3.5.3 Cascaded Modulators

Sigma-delta modulators can be cascaded in order to achieve increased resolution [3.23]. In a cascaded ΣΔ modulator, the input signal is applied to a first ΣΔ modulator, whose quantization errors are then digitized by a second ΣΔ modulator (Fig. 3-12). The output of the second modulator can then be digitally combined with that of the first to improve the overall resolution. The main advantage of this technique is that by using first- or second-order ΣΔ modulators in both stages, higher-order noise shaping can be achieved *without* the stability problems associated with higher-order loop filters. It does, however, require good matching between the transfer functions of the two modulators. This cannot be expected if the first modulator is a *thermal* ΣΔ modulator, while the second is (necessarily) an *electrical* ΣΔ modulator. A further problem is the fact that the comparator's input signal will typically be in the millivolt range, which severely complicates the design of the second modulator. For these reasons, it is not practical to use cascading as a means of improving the resolution of a TΣΔ modulator.

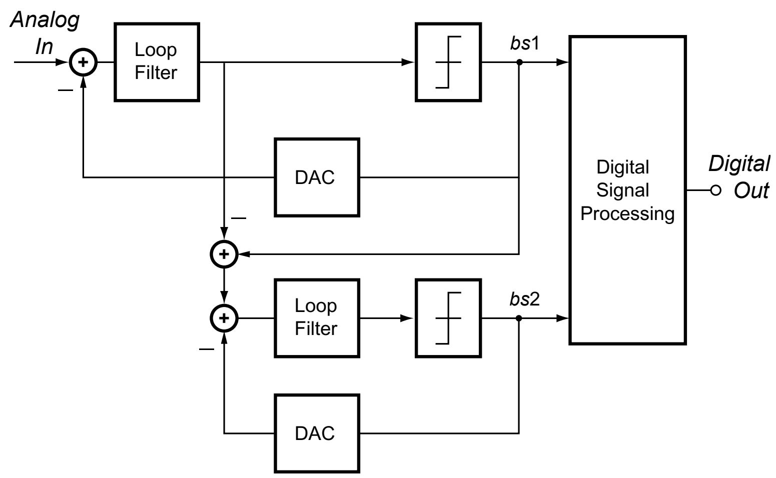

Figure 3-12 *Block diagram of a cascaded ΣΔ modulator.*

3.6 Conclusions

Embedding a thermal sensor in the feedback loop of a TΣΔ modulator is an excellent method of digitizing its heat loss. Such modulators can be realized very simply, because in addition to the elements of the sensor itself, i.e., heaters and temperature sensors, only a clocked comparator is required. No explicit loop filter is required, since the sensor's thermal inertia will function as a low-pass filter in the thermal domain. The output of the modulator is a digital signal, which can be directly interfaced to a microprocessor for further processing. In addition, embedding the sensor in a feedback loop improves its response time.

Using the electro-thermal analogy, the sensor's thermal behaviour can be modelled by a passive RC filter, which exhibits first-order behaviour at high frequencies. In consequence, the resulting modulator will be unconditionally stable, irrespective of the exact structure of the sensor. Because the loop filter is passive, however, there is a direct trade-off between clock frequency and resolution. Since clock frequency will eventually be limited by circuit non-idealities, the resolution of the basic modulator is limited. Improved resolution can be obtained by using a multi-bit quantizer, or by augmenting the thermal filter with an electrical integrator. Due to matching issues, however, it is not practical to use cascaded topologies to improve resolution.

Although TΣΔ modulators have been primarily used to interface thermal flow sensors, they can, in principle, be used to interface other thermal sensors. Examples of such sensors include: thermal pressure sensors, thermal conductivity sensors, thermal radiation sensors, and thermal accelerometers.

3.7 References

[3.1] J.H. Huijsing and F.R. Riedijk, “Integrated semiconductor circuit for thermal measurements,” U.S. Patent No. 5064296.

[3.2] Y. Pan and J.H. Huijsing, “New integrated gas-flow sensor with duty cycle output,” *Electronics Letters*, vol. 24, no. 9, pp. 542-543, April 1988.

[3.3] Y. Pan, F.R. Riedijk and J.H. Huijsing, “A new class of integrated thermal oscillators with duty-cycle output for application in thermal sensors,” *Sensors and Actuators A: Physical*, vol. 21-23, pp. 655-659, Mar. 1990.

[3.4] E.J. Hogenbirk, H.J. Verhoeven and J.H. Huijsing, “An integrated smart sensor for flow and temperature with I^2C bus interface based on thermal sigma-delta modulation,” *Digest of Transducers ‘93*, pp. 792-795, 1993.

[3.5] H.-J Verhoeven and J.H. Huijsing, “An integrated gas flow sensor with high sensitivity, low response time and a pulse-rate output,” *Sensors and Actuators A: Physical*, vol. 41, no. 1-3, pp. 217-220, April 1994.

[3.6] H.-J Verhoeven and J.H. Huijsing, “Design of integrated thermal flow sensors using thermal sigma-delta modulation,” *Sensors and Actuators A: Physical*, vol. 52, no. 1-3, pp. 198-202, April 1996.

[3.7] H.-J Verhoeven, “Smart thermal flow sensors,” Ph.D. Thesis, Delft University of Technology, 1996.

[3.8] M. Domínguez, F. Masana, V. Jimenez, S. Bermejo, J. Amirola, J. Ballester, N. Fueyo and L. Castañer, “Low-cost thermal TΣΔ airflow sensor,” *IEEE Sensors Journal*, vol. 2, no. 5, pp. 453–462, October 2002.

[3.9] L. Castañer, V. Jimenez, M. Domínguez, F. Masana and A. Rodriguez, “Flow measurement hits home,” *IEEE Circuits and Devices Magazine*, vol. 13, no. 1, pp. 14-18, Jan. 1997.

[3.10] L. Castañer, V. Jimenez, M. Domínguez, F. Masana and A. Rodriguez, “A conduction-convection design for liquid flow sensing,” *Sensors and Actuators A: Physical*, vol. 66, no. 1-3, pp. 131-137, April 1998.

[3.11] M. Domínguez and L. Castañer, “Bounding of thermal $\Sigma-\Delta$ modulators’ output for sensors,” *Proc. ISCAS ‘99*, vol. 2, pp. 244-247, June 1999.

[3.12] J. Vink, H.-J Verhoeven and J.H. Huijsing, “Response speed optimization of thermal gas-flow sensors for medical application,” *Digest of Transducers ‘95*, pp. 524-528, June 1995.

[3.13] J.K. Zelisse, F.R. Riedijk and J.H. Huijsing, “Thermal sigma-delta modulator for wind speed and direction measurement,” *Proc. of Eurosensors V*, p. 303, Sept. 1991.

[3.14] K.A.A. Makinwa and J.H. Huijsing, “A wind sensor interface using thermal sigma-delta modulation,” *Proc. of Eurosensors XIV*, pp. 249 - 252, Sept. 2000.

[3.15] T.S.J. Lammerink, N.R. Tas, G.J.M. Krijnen and M.C. Elwenspoek, “A new class of thermal flow sensors using $\Delta T = 0$ as a control signal,” *Proc. of MEMS 2000*, pp. 525-530, Jan. 2000.

[3.16] T.S.J. Lammerink, R.J. Wiegerink and M. Elwenspoek, “Temperature-balance micro flow sensor system based on a free oscillating differential power controller,” in *Sensor Technology 2001*, Kluwer Academic Publishers, pp. 19-24, 2001.

[3.17] F.J. Auerbach, G. Meiendres, R. Muller and G.J.E. Scheller, “Simulation of the thermal behaviour of thermal flow sensors by equivalent electrical circuits,” *Sensors and Actuators A: Physical*, vol. 41, no. 1-3, pp. 275-278, April 1994.

[3.18] F. Kuo, “Network analysis and synthesis,” John Wiley & Sons, 1966.

[3.19] G.C. Temes and J.W. LaPatra, “Introduction to circuit synthesis and design,” McGraw-Hill, 1977.

[3.20] M. Narz and P. Nance, “Thermal modeling of power-electronic systems,” *Infineon Technologies Application Note*, Jan. 1998.

[3.21] V. Székely and M. Rencz, “Thermal dynamics and the time constant domain,” *IEEE Transactions on Components and Packaging Technology*, vol. 23, no. 3, pp. 587-594, Sept. 2000.

[3.22] O. Feely and L.O. Chua, “The effect of integrator leak in $\Sigma-\Delta$ modulation,” *IEEE Trans. on Circuits and Systems*, pp. 1293-1305, vol. 38, no. 11, Nov. 1991.

[3.23] S.R. Norsworthy, R. Schreier and G.C. Temes (Eds.), “Delta-sigma data converters,” New York: IEEE Press, 1997.

[3.24] D. Jaeggi, C. Azeredo Leme, P. O’Leary and H. Baltes, “Improved CMOS power sensor,” *Proc. of Transducers ‘93*, pp. 462-465, June 1993.

[3.25] C. Azeredo Leme, “Oversampled Interfaces for IC Sensors,” Ph.D. thesis, Swiss Federal Institute of Technology, 1993.

[3.26] C. Condemine, M. Belleville, D. Barbier, G. Delhomme and A. Dittmar, “A new sigma-delta thermal conductivity microsystem,” *Proc. of the 1st IEEE EMBS conference*, pp. 188-91, Oct. 2000.

[3.27] N. Delorme, C. Condemine and D. Barbier, “Sigma-delta microsystems for readout and servo control,” *Proc. of the SPIE Conf. on Smart Sensors Actuators and MEMS*, pp. 270-7, May 2003.

[3.28] O. Feely and L.O. Chua, “Multi-level and non-ideal quantization in sigma-delta modulation,” *Int. J. of Circuit Theory and Applications*, pp. 61-83, vol. 21, no. 1, Jan. 1993.

[3.29] R.D. Hughes, “Remote diodes yield accurate temperature measurements,” *EDN*, vol. 48, no. 15, pp. pp. 59-62, July 10, 2003.

4 A Hot-Transistor Anemometer

In this chapter, the design and development of a low-cost thermal anemometer based on a pair of bipolar transistors is described. One of the transistors is self-heated, and is operated in constant temperature difference (CTD) mode by incorporating it in a thermal sigma-delta modulator. In this configuration, the self-heated transistor, doubling as a temperature sensor, measures its own temperature, while the second transistor measures that of the flow. The modulator compensates for the heat loss of the self-heated transistor by heating it with pulses derived from its bitstream output. In this manner, the bitstream average will be proportional to the transistor's heat loss and will, therefore, be a function of flow speed. Different modulator configurations were investigated, the most attractive of which employs an additional electrical integrator to improve modulator performance. Wind tunnel measurements show that robust and inexpensive off-the-shelf transistors can be used to realize sensitive anemometers. Such hot-transistor anemometers are therefore well suited for low-cost flow-sensing applications.

4.1 Transistor-Based Thermal Anemometers

Since they can be used as accurate absolute-temperature sensors, bipolar transistors have often been used to realize thermal anemometers [4.1–4.9]. Such transistor-based anemometers typically employ two transistors: a "hot" transistor, which measures the temperature of the heated surface exposed to the flow, and a "cold" transistor, which measures ambient temperature. The temperature difference between the hot and cold transistors is known as the overheat ΔT, and is related to the power

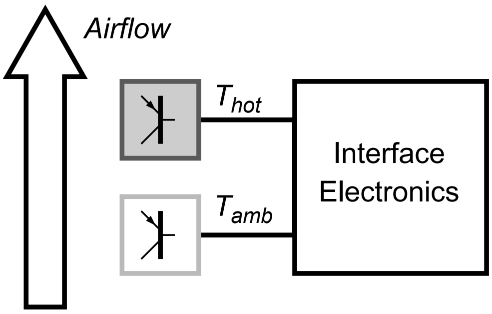

Figure 4-1 *A simple hot-transistor anemometer.*

dissipation P in the sensor and the flow speed U in a well-defined manner. This relationship is known as King's law (Section 2.2) and is given by:

$$P = (A + B\sqrt{|U|})\Delta T \tag{4-1}$$

where A and B are constants defined by the sensor's geometry.

Typically, the hot transistor will be heated by a resistor [4.4–4.8] integrated on the same silicon substrate. Alternatively, it can be *self-heated* by appropriate biasing [4.1, 4.2, 4.3, 4.9]. As shown in Fig. 4-1, a thermal anemometer can then be realized by using two transistors and some interface electronics, this will be referred to as a hot-transistor anemometer (HTA). This approach avoids the extra manufacturing costs usually associated with the packaging of silicon flow sensors, since discrete transistors are readily available at low-cost in small, robust and thermally optimized packages. The latter is important because, for use in a HTA, the transistors must be in good thermal contact with the flow.

Packaging issues are also avoided if a second transistor (on the same substrate) is used as a heater [4.10], since such *double* transistors are also available as off-the-shelf components. For such transistors, however, the range of available packages is rather limited, since they are not nearly as ubiquitous as single transistors.

4.2 Interfacing a Hot-Transistor Anemometer

The interface electronics of a hot-transistor anemometer must bias the transistor in such a way that it can used both as a heater and as a temperature sensor. In addition, it must facilitate the accurate measurement of the hot transistor's power dissipation and overheat, so that flow speed can be computed from King's law. In this section, an interface architecture which meets these requirements will be described.

4.2.1 Transistor Biasing

The collector current used to bias a self-heated hot transistor will usually be much larger than that of the cold transistor, which must *not* be self-heated as this would affect its ability to accurately measure ambient temperature. As a result of this difference in collector current, the two transistors will have very different temperature sensing characteristics (Section 2.5.2), which will cause errors in the computed overheat. For a limited temperature range, such errors can be reduced by trimming the interface electronics at two different temperatures [4.2]. However, this is rather difficult to do in practice, and a better solution is to operate the hot transistor in a time-multiplexed manner, in which it alternately functions as a heater (high collector current) and as a temperature sensor (low collector current) [4.3, 4.9]. By biasing the cold transistor at the same low collector current, the temperature sensing characteristics of the two transistors can be made (at least nominally) identical.

4.2.2 Application of Feedback

As discussed in Section 2.2.2, a HTA can be operated in either constant power (CP) mode or constant temperature difference (CTD) mode. When operated in CP mode, however, its transient response will be determined by the thermal time constant of the hot transistor, which may be several tens of seconds long [4.9]. Much faster transient response can be obtained by operating a HTA in CTD mode, in which the overheat is kept constant. This can be achieved by embedding the HTA in a linear feedback loop [4.1, 4.2], in a duty-cycle modulator [4.3, 4.4], or in a thermal sigma-delta (TΣΔ) modulator [4.5, 4.6]. Of these methods, the use of a TΣΔ modulator is preferred because it provides a direct digital representation of

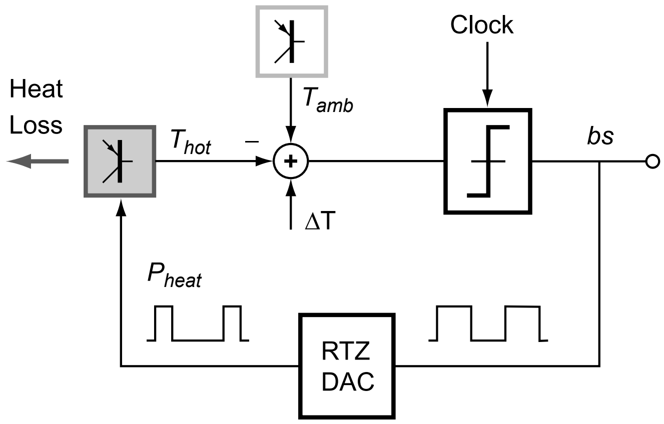

Figure 4-2 *Block diagram of a HTA-TΣΔ modulator.*

the hot transistor's heat loss, without the duty-cycle modulator's sensitivity to periodic interference [4.4], or the stability issues associated with a linear feedback loop [4.12].

A block diagram of a HTA embedded in the feedback loop of a TΣΔ modulator is shown in Fig. 4-2. For want of a better name, this configuration will be referred to as a HTA-TΣΔ modulator. To ensure that there is a well-defined temperature-sensing interval during each clock period, the transistor is heated by a return-to-zero (RTZ) signal (Fig. 4-3). During this interval, the transistor's junction temperature T_j is compared with the sum of the ambient temperature T_{amb} and the desired overheat ΔT. If T_j is less than this set point, a heat pulse is applied to the hot transistor, otherwise, the transistor is cooled by the flow. As shown in Fig. 4-3, T_j will then fluctuate around the desired set point. These fluctuations will be filtered out by the transistor's thermal inertia, provided that the clock frequency is high enough, and so $T_j \sim T_{amb} + \Delta T$. In other words, the modulator regulates the transistor's junction temperature. If the transistor is in a thermally optimized package, i.e., one that ensures good thermal contact with the flow, the temperature of the surface exposed to the flow will also be regulated (indirectly) and so the HTA will operate in CTD mode.

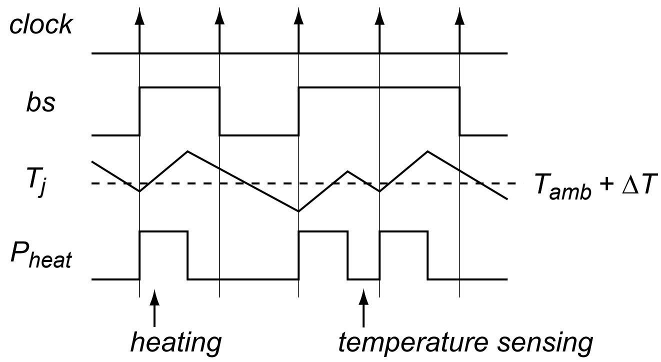

Figure 4-3 *Timing of the HTA-TΣΔ modulator.*

The output of the modulator is a bitstream $bs \in \{0, 1\}$, whose average value μ represents the average heating power required to maintain the overheat constant. If P_{ref} is the average power dissipated by a heat pulse during a clock period, then the average heating power dissipated in the sensor is μP_{ref}, and from King's Law:

$$\frac{\mu P_{ref}}{\Delta T} = (A + B\sqrt{|U|}) . \tag{4-2}$$

Since P_{ref} and ΔT will be fixed by the interface electronics, the flow speed U can then be computed from the bitstream average.

4.3 Choosing a Hot Transistor

From the discussion in the previous section, it is clear that the key component of a HTA-TΣΔ modulator is the hot transistor, which is variously used as a temperature sensor, heater, and loop filter. In this section, the various considerations influencing the choice of a particular transistor from the wide range of available types, will be discussed.

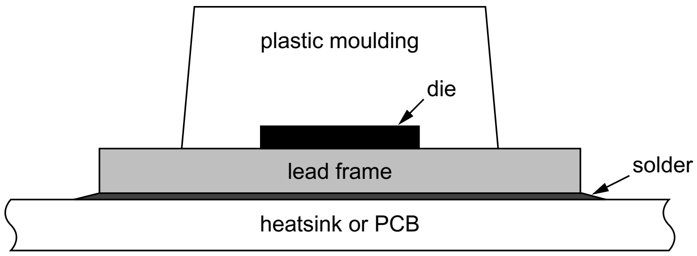

Figure 4-4 *Cross-section of a package for power applications.*

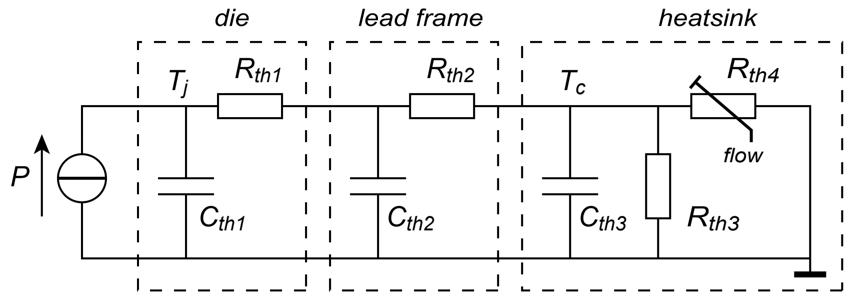

Figure 4-5 *Simplified thermal model of a packaged transistor.*

4.3.1 Flow-Sensing Considerations

For use as a thermal anemometer, the hot transistor should be packaged in such a way that it is in good thermal contact with the flow. In other words, its junction-to-ambient thermal resistance R_{ja} should be as low as possible. This requirement is met by packages intended for power applications, in which the die is bonded directly to an exposed lead frame pad, which, in turn, can be soldered to a PCB or heatsink (Fig. 4-4).

A simplified thermal model of a transistor in such a package is shown in Fig. 4-5. It consists of three thermal RC sections, which model the thermal behaviour of the silicon die, the lead frame and the heatsink, respectively. The current source P models the heat dissipated in the transistor. The choice of a given transistor and heatsink fixes all the model parameters except for the variable thermal resistance R_{th4}, which models the transistor's convective heat loss and will be a function of flow speed. The transistor's conductive heat loss is modelled by the fixed resistor R_{th3}. Usually the thermal capacitance of the lead frame and heatsink will be much larger than that of the (physically smaller) die, and so their time constants will dominate the transistor's transient response.

From this model, a number of important observations can be made. Firstly, for fast transient response, the size of the lead frame and heatsink should be as small as possible. Secondly, since the main aim of the modulator shown in Fig. 4-2 is to (indirectly) regulate the temperature of the heatsink T_c via the transistor's junction temperature T_j, the transistor's junction-to-case resistance $R_{jc} = R_{th1} + R_{th2}$ should be much less than the case-to-ambient resistance $R_{ca} = R_{th3} \| R_{th4}$. Also, the time constants associated with the die and lead frame respectively, should be smaller than that associated with the heatsink. This improves the regulation of T_c, since it means that after a heat pulse, T_j will quickly settle to T_c during the temperature-sensing interval. Finally, the transistor should be mounted such that its heat loss to the surroundings is dominated by convection and not by conduction, e.g., via its leads.

These requirements can be met by choosing a transistor with a small die in the smallest possible package. A bare die suspended by its leads in the flow would, therefore, appear to be ideal for use in a HTA. This is indeed the case; an anemometer using such transistors has been reported [4.2], with a time constant of only "a few milliseconds". However, this approach results in a rather fragile construction. An alternative is to use packages intended for surface-mounting, such as the SOT-89 package (Fig. 4-6), which is small (2.5 x 4.5 x 1.5mm) and widely available. Although smaller packages are available, e.g. SOT-23, these do not have exposed lead frame pads and so have much higher junction-to-case resistances. Chip scale packages would be even better, however, suitable transistors in these packages are (not yet) available.

Different methods of mounting a SOT-89 transistor on a PCB are shown in Fig. 4-7 and Fig. 4-8. The fastest transient response will be obtained by mounting the transistor upside down in a small hole in the PCB, so that its lead frame is directly exposed to the flow (Fig. 4-7). Since the lead frame is only 0.4mm thick, this method of mounting will only disturb the flow

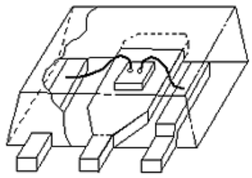

Figure 4-6 *Cutaway view of a transistor in a SOT-89 package*.

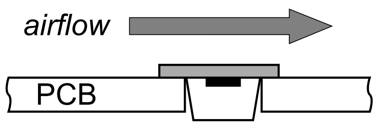

Figure 4-7 *Cross-sectional view of a SOT-89 package mounted for fast transient response*.

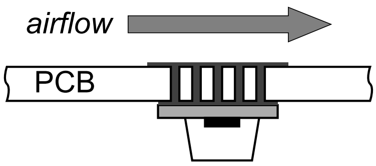

Figure 4-8 *Cross-sectional view of a SOT-89 package mounted for minimum turbulence*.

slightly. To further minimize this disturbance, the transistor can be soldered to one side of the PCB while the flow is passed over a pad on the other side. The use of through-plated PCB vias ensures good thermal contact between the transistor and the flow (Fig. 4-8). Instead of to a PCB, the transistor can be attached to a thermally conducting substrate, such as ceramic, in which case vias are not required. In both cases, however, the transistor's transient response will be significantly slower due to the added thermal capacitance of the substrate.

4.3.2 Temperature Sensing Considerations

To minimize the effect of ambient temperature variations on the overheat, the hot and the cold transistors should both be mounted in the same manner. They will then have identical time constants, and thus be affected in the same manner by changes in ambient temperature [4.1]. Like all thermal anemometers, however, a HTA will exhibit some temperature dependency due to the temperature dependency of the physical properties of the fluid (Section 2.2).

To minimize static overheat errors, both transistors should have identical temperature sensing characteristics. Due to transistor mismatch, however, this will not be the case. The resulting overheat inaccuracy then limits the minimum possible overheat, and thus the anemometer's minimum power dissipation. For a bipolar transistor, a good measure of process spread is the spread on its forward current gain; tight specifications for this parameter usually indicate good process control. Base resistance mismatch will be a further source of error. However, it can be minimized by using transistors with intrinsically low base resistances.

4.3.3 Choice of Transistor

Taken together, the considerations discussed above limit the choice of transistor to so-called small-signal or medium-power types. It was decided to use a PXT3904 transistor, which is a 2N3904-type transistor in a SOT-89 package, because it has a small die size ($0.15mm^2$) and because it is widely recommended for use as a temperature sensor [4.13].

4.4 Thermal Modelling of a Self-Heated Transistor

The behaviour of a HTA-TΣΔ modulator can be investigated experimentally and/or by time-domain simulations. The latter, however, requires an accurate model of the hot transistor's thermal impedance, i.e., the relationship between its heat dissipation and the temperature rise of its base-emitter junction. In literature, this impedance is often referred to as the transistor's thermal *spreading* impedance, Z_{th}, as it describes the spread of heat from the transistor to its surroundings. Due to the close proximity of the heat-generating and heat-sensing regions of a bipolar transistor, Z_{th} can be modelled as an RC driving-point impedance (Section 3.3.1).

4.4.1 Possible Approaches

Various analytical models of Z_{th} have been proposed, in which the heat-generating region of a transistor is treated as a point source [4.14, 4.15], as a sphere [4.16], and as a disc [4.17] located near the surface of a semi-infinite die. The main limitation of such models is that they do not take into account the effect of the transistor's packaging. In a real transistor heat will spread rapidly through the die and eventually encounter the lead frame and package, through which it slowly diffuses to the surroundings. Such analytical models are, therefore, only useful for modelling the first millisecond or so after a heating transient, during which heat flow is confined to the die [4.18].

The thermal behaviour of a real transistor can be accurately modelled using 3-D finite-element analysis. From the results, a compact electrical (RC) model of the transistor can be derived. However, this process is computationally intensive and requires detailed knowledge of the transistor's geometry. Although some semiconductor manufacturers provide such models for power MOS transistors [4.19], no such models are (at present) available for bipolar transistors.

Alternatively, an RC model of Z_{th} can be derived from measurements of the transistor's thermal step response. The advantage of this approach is that it requires no simplifying assumptions, and it also fully incorporates the thermal behaviour of the package and heatsink. It does, however, require experimental characterization of the transistor's step response. This is described in the following section.

4.4.2 Experimental Approach

The hot transistor's thermal step response was determined by measuring its cooling curve. To do this, the transistor was initially heated by a large collector current (100mA) until a steady-state temperature was reached, after which the collector current was abruptly reduced to a low level (100μA). Using V_{be} sensing, the junction temperature was then sampled at 100kHz while the transistor cooled.

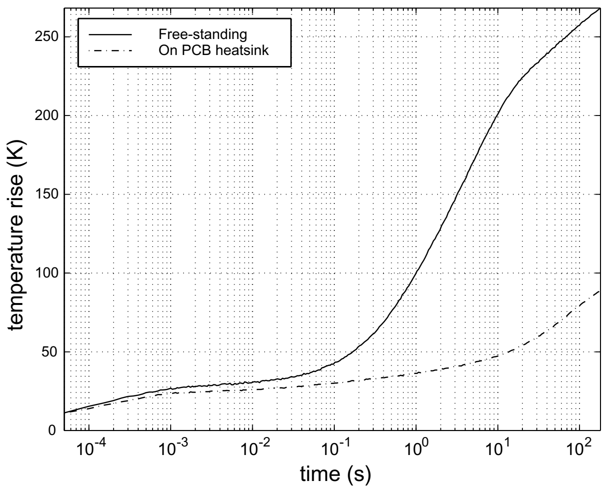

Figure 4-9 *Influence of different mounting methods on the response to a 1W step of a PXT3904 transistor (SOT-89 package).*

The measured step response of a PXT3904 transistor mounted as shown in Fig. 4-7, is shown in Fig. 4-9. In this figure, the input power has been normalized to 1W, which explains the destructively high temperatures that were apparently achieved. Also shown, is the, similarly normalized, step response obtained when the transistor is mounted on a PCB heatsink, as shown in Fig. 4-8. The PCB is 1.57mm thick, and the pad exposed to the flow is circular, with a diameter of 15mm. It may be seen that mounting the transistor in this manner slows down its transient response by two orders of magnitude. In both cases, however, the first few milliseconds of the step response are similar, reflecting the spread of heat through the die and lead frame.

In order to understand the measurement results better, the step response of the free-standing transistor was compared with the results predicted by an analytical model, in which the heat-generating region of the transistor is assumed to be a uniformly heated sphere. This model was chosen because formulae for determining the parameters of an equivalent RC network

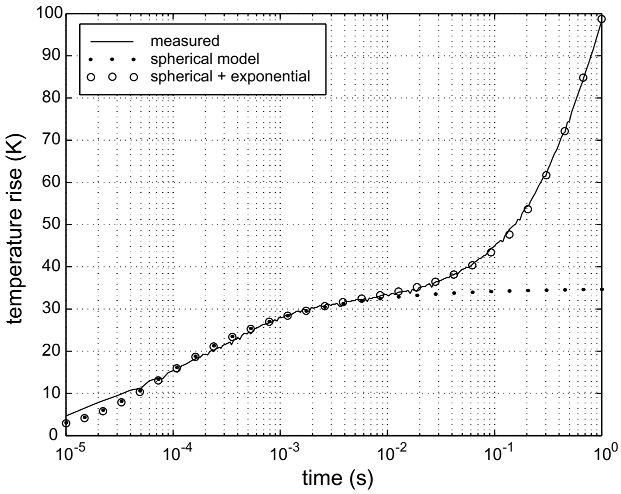

Figure 4-10 *Measured and modelled step responses of a PXT3904 transistor (SOT-89 package).*

have been provided [4.16]. According to this model, the temperature rise T_{sphere} on the surface of a sphere of radius a is given by:

$$T_{sphere}(t, a) = \frac{3R_{th}\alpha t}{a^2}\left[1 - 2\left(i^2 erfc(0) + i^2 erfc\left(\frac{a}{\sqrt{\alpha t}}\right)\right) - \frac{4\sqrt{\alpha t}}{a}\left(i^3 erfc(0) + i^3 erfc\left(\frac{a}{\sqrt{\alpha t}}\right)\right)\right] \tag{4-3}$$

where $R_{th} = 1/4\pi ka$ is the thermal resistance of the sphere, k is the thermal conductivity, $\alpha = k/\rho c$ is the thermal diffusivity, ρ is the density and c is the specific heat capacity. Also, i^2erfc() and i^3erfc() are the second and third integrals of the complementary error function, respectively.

For a given radius, the thermal resistance of the sphere is fixed. After [4.15], however, the accuracy of this model can be improved by treating *both* R_{th} and a as fitting parameters. Even so, the predicted step response (with R_{th} = 35K/W and a = 108µm) only accounts for the first few milliseconds of the measured response (Fig. 4-9). The rest of the step

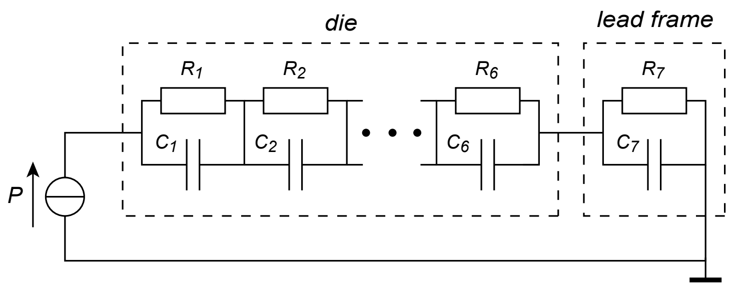

Figure 4-11 *RC equivalent network for* Z_{th}.

response then reflects the thermal behaviour of the lead frame and can be modelled by adding an exponential term to (4-3):

$$T_{step}(t, r) = T_{sphere}(t, r) + R\exp(-t/\tau) . \tag{4-4}$$

With R = 95K/W and τ = 0.9s, this expression models the step response fairly accurately over 5 decades (Fig. 4-9). Since this extra term accurately models the interaction between the lead frame and the outside world, the effects of flow speed on Z_{th} can be modelled, at least qualitatively, by varying the value of R.

Using the formulae provided in [4.16], the parameters of an equivalent 6-segment Cauer RC ladder network were computed. The extra exponential of (4-4) was incorporated by adding an extra RC section to the network's Foster equivalent, as shown in Fig. 4-11. In a final step, the parameters of the network parameters were tweaked so as to improve the fit between the measured and modelled step responses (Fig. 4-12).

The modelled frequency response of Z_{th} is shown in Fig. 4-13. At frequencies below a few Hertz, the filter's response is due to the time constant of the lead frame, and will, therefore, be influenced by variations in the flow speed. The gentle roll-off at frequencies above a few hundred Hertz is due to the thermal inertia of the die.

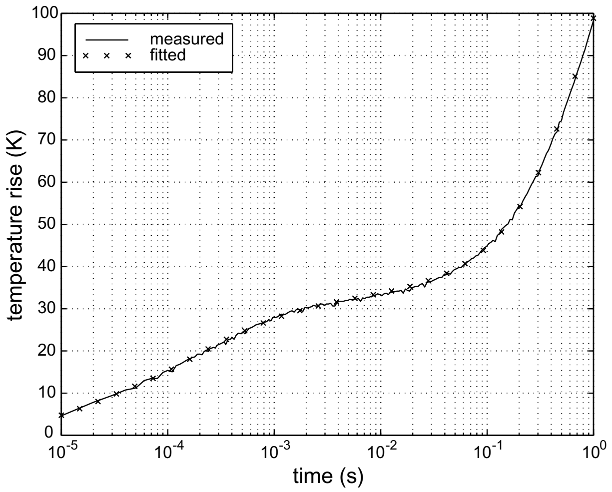

Figure 4-12 *Measured and fitted step responses of a PXT3904 transistor (SOT-89 package).*

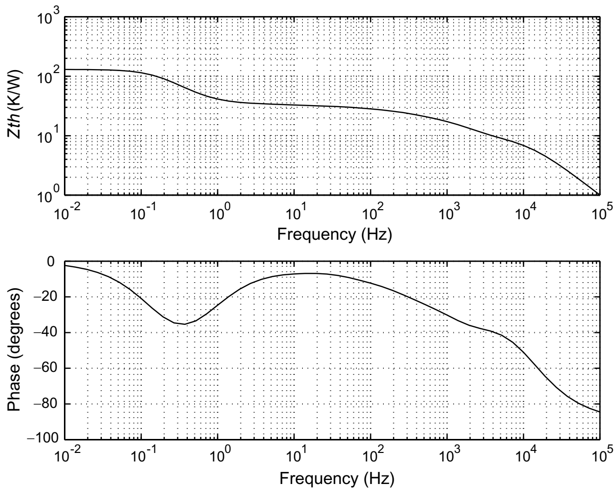

Figure 4-13 *Modelled frequency response of a PXT3904 transistor in a SOT-89 package.*

4.5 Modulator Design

4.5.1 Design Considerations

The primary task of the HTA-TΣΔ modulator shown in Fig. 4-2 is to operate the lead frame of the hot transistor in CTD mode. This requires that the variations in the transistor's temperature are small compared to the overheat ΔT, *and* that the temperature of the base-emitter junction settles to that of the lead frame before the end of the temperature-sensing interval. The first of these requirements means that the clock frequency f_s must exceed the cut-off frequency of the thermal filter Z_{th}, which implies that $f_s > 10\text{kHz}$ (Fig. 4-13). The second requirement means that the temperature-sensing interval should be at least of the same order of magnitude as the time-constant of the die. A significantly shorter interval means that the modulator will regulate the temperature of the base-emitter junction rather than the temperature of the lead frame. From Fig. 4-9, however, it may be inferred that it takes the die at least 100µs after the end of a heat pulse to acquire the temperature of the lead frame, which implies that $f_s < 10\text{kHz}$. A trade-off must thus be made between these two conflicting requirements.

A further design consideration is the modulator's resolution. Since the loop filter is an RC driving-point impedance, its DC transfer function will have a fractal staircase structure (Section 3.4.1). Using equation (A-18), the exact relationship between clock frequency and the modulator's (worst-case) resolution can be computed. The results are shown in Fig. 4-14 for heat pulses with a duty cycle $\delta = 0.5$. At $f_s = 15\text{kHz}$, the worst-case resolution is only about 3.5%. Due to the "plateau" in Fig. 4-14, f_s will have to be made impractically high in order to substantially improve the modulator's resolution.

For a given clock frequency, the modulator's resolution can be increased by increasing the resolution of the quantizer (Section 3.5.2). This is undesirable, however, since it significantly increases the complexity of the interface electronics. A simpler method of increasing resolution is by

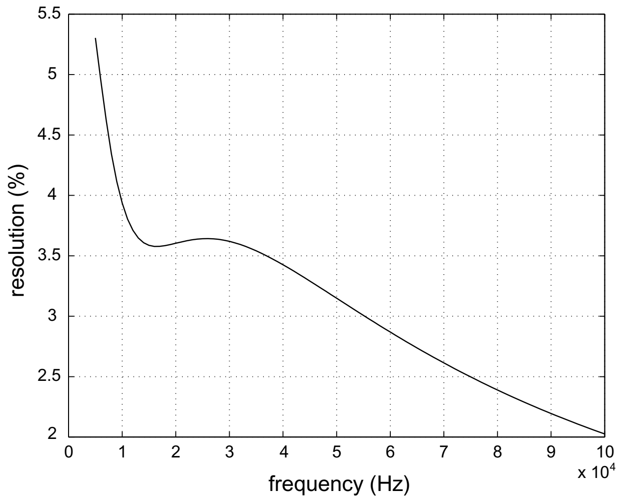

Figure 4-14 *Resolution of the basic HTA-TΣΔ modulator as a function of clock frequency.*

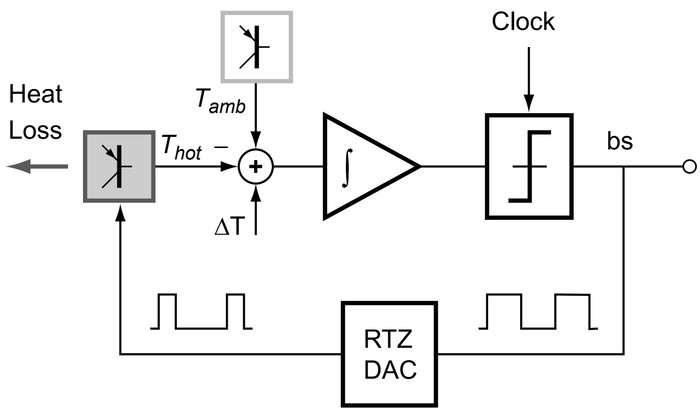

Figure 4-15 *Block diagram of an improved HTA-TΣΔ modulator with an electrothermal loop filter.*

including an electrical integrator in the loop (Section 3.5.1). The resulting electrothermal loop filter (Fig. 4-15) has infinite DC gain, which eliminates the steps in the modulator's DC transfer function. The price for

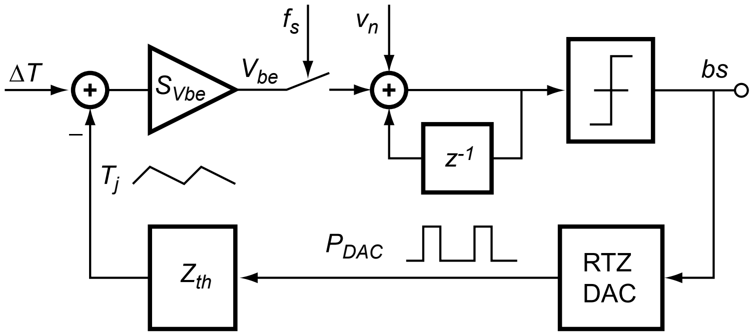

Figure 4-16 *Block diagram of the simulated HTA-TΣΔ modulator.*

this performance improvement is the possibility of modulator instability, since the loop filter's phase shift will tend to 180 degrees at high frequencies. From Fig. 4-13, however, even with an electrical integrator, the resulting modulator will be stable for clock frequencies up to about 10kHz (where the phase lag of Z_{th} is about 45 degrees). Since the phase shift of Z_{th} at these frequencies is entirely due to the thermal inertia of the hot transistor's die, the stability of the improved modulator will not be affected by the way the transistor is mounted or by flow speed changes.

4.5.2 Simulations

The behaviour of the improved HTA-TΣΔ modulator was further investigated by MATLAB simulations. The block diagram of the simulated modulator is shown in Fig. 4-16. Its bitstream output *bs* drives the hot transistor with RTZ heat pulses with a duty cycle δ, which are filtered by the transistor's thermal impedance Z_{th}. The difference between the resulting temperature Tj and the desired overheat ΔT is then sampled and integrated before being applied to the comparator input. The thermal noise of the interface electronics was simulated by adding white noise v_n to the integrator input. This was scaled by the temperature coefficient of V_{be}, denoted by S_{Vbe} and approximately equal to -2.1mV/K, in order to convert it to the thermal domain. The noise acts as a dither signal and breaks up the discrete limit cycles that will otherwise occur in the modulator. The following parameters were also used in the simulations: f_s = 16,384Hz, $\delta = 0.5$, P_{ref} = 164mW, and v_n = 6.4μV.

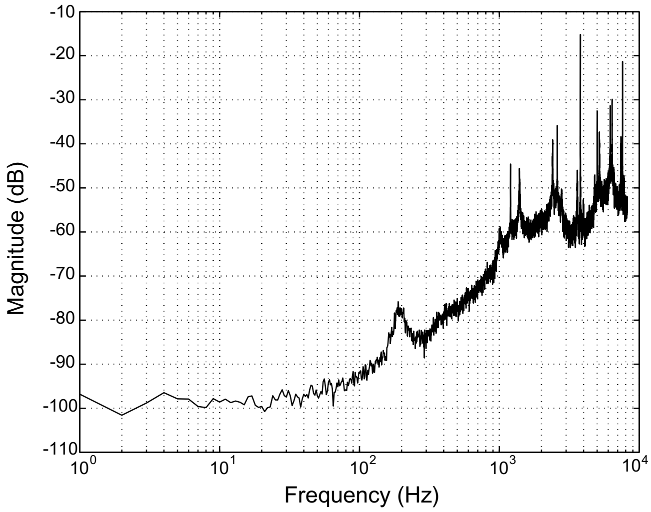

Figure 4-17 *Simulated power spectrum of a differential modulator (Hann windowed average of 6, 64kbit, bitstream segments with 50% overlap).*

The power spectrum of the modulator's bitstream is shown in Fig. 4-17. The noise floor from DC to about 20Hz is due to the added thermal noise. At higher frequencies, the quantization noise exhibits first-order noise shaping (20dB/decade), indicating that the electrical integrator is responsible for most of the noise-shaping. The modulator therefore behaves like a first-order modulator, which explains the pronounced tones visible in the power spectrum. Their amplitude and frequency are not fixed, but vary as a function of the input signal's DC level [4.20].

The first-order noise-shaping means that a sinc^2 filter can be used as a decimation filter. (A simpler sinc filter can also be used, at the expense of approximately 4dB more noise.) Since the only design parameter of such a filter is the length of its impulse response, a trade-off was made between bandwidth limiting (for maximum resolution) and fast transient response. It was decided to use a filter with a 0.25s long impulse response, which at a clock frequency f_s = 16,384Hz corresponds to a 4096-tap filter. With this filter, the modulator's resolution is at the 16 bit level, even with the added electrical noise.

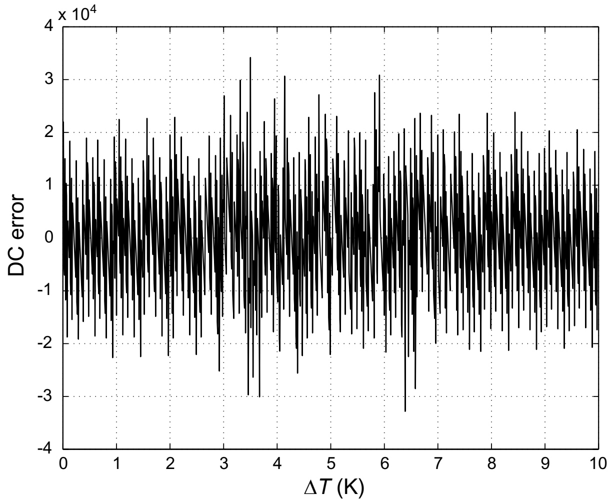

Figure 4-18 *DC error of the improved HTA-TΣΔ modulator.*

In an ideal modulator, the average heating power generated by the DAC will exactly balance the heating power required to maintain the overheat, i.e., $\mu P_{ref} = \Delta T/R_{th}$. Modulator resolution can then be investigated by plotting the DC error $\mu - \Delta T/(R_{th}P_{ref})$ as a function of the overheat ΔT. The results are shown in Fig. 4-18 for the improved modulator, decimated by a 4096-tap sinc^2 filter and with $v_n = 0$. It can be seen that the resolution of the modulator is at the 10-bit level. This is much better than the 3.5% (worst case) resolution exhibited by the basic modulator. (The full DC error plot of this modulator is shown in Fig. A-6.)

Also of interest is the signal swing at the transistor's base-emitter junction and at the output of the integrator. These remain bounded over the full input range, indicating that the modulator behaves more like a first-order modulator than a second-order modulator (Fig. 4-19). The peak-to-peak variation of T_j is about 0.5K, confirming that the modulator effectively regulates its temperature. It should be noted that this is the temperature variation in the die, not that of the surface exposed to the flow. The latter will be much smaller, due to the thermal inertia of the lead frame.

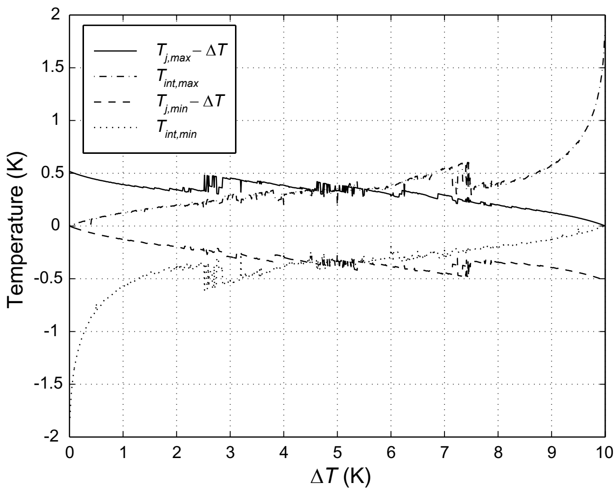

Figure 4-19 *Signal swing in the improved HTA-TΣΔ modulator.*

4.5.3 Circuit Implementation

A block diagram of the implemented HTA-TΣΔ modulator is shown in Fig. 4-20. Two identical PXT3904 transistors, Q_{hot} and Q_{amb}, are used as the hot and cold temperature sensors, respectively. Their temperature is determined by V_{be} sensing. Their emitter currents (and hence their collector currents) are defined by the opamps A_1 and A_2, which ensure that a fixed reference voltage V_{ref} appears across the fixed resistors ($R_1 - R_4$) in their emitter circuits.

As shown in the timing diagram (Fig. 4-21), each modulator clock period T may be divided into two intervals: a heating phase and a temperature sensing phase. During the heating phase, Q_{hot} will be heated if the comparator output is a logical "1," and allowed to cool if its output is a logical "0." Heating is accomplished by closing S_1 and biasing the transistor at a large emitter current I_{heat}.(defined by the sum of R_1 and R_2). During this phase, S_2 is open and the output of the integrator (A_3, R_5 and C_1) remains unchanged.

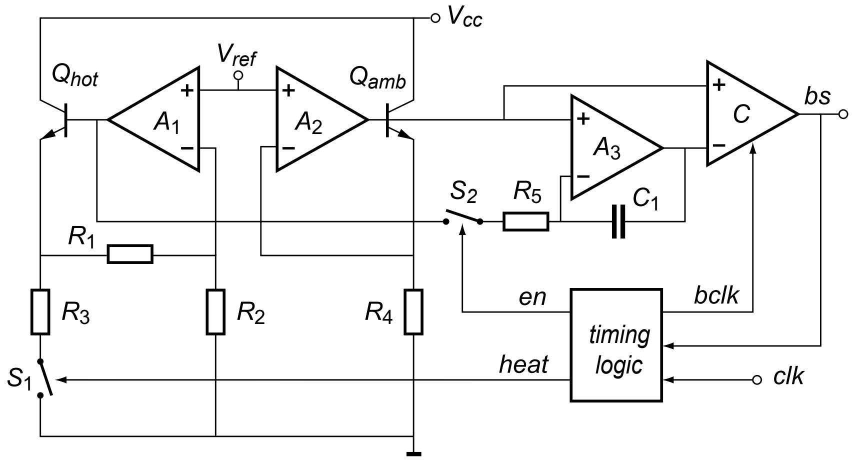

Figure 4-20 *Circuit implementation of a HTA.*

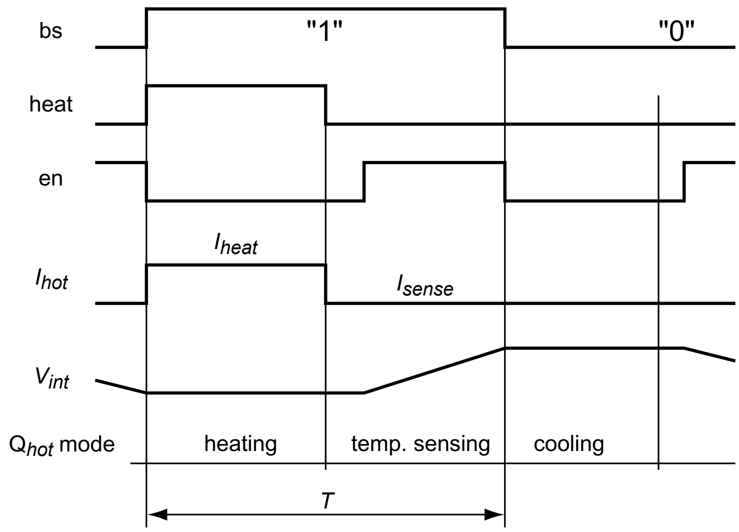

Figure 4-21 *Timing diagram of the implemented HTA*.

During the temperature sensing phase, S_1 is open and both transistors will be biased at an emitter current I_{sense} of about 100μA. This is low enough to prevent significant self-heating. After a short pause, which allows $V_{be,hot}$ to settle, S_2 is closed, and the integrator will be driven by a voltage $V_{be,amb} - I_{sense}R_1 - V_{be,hot}$. Due to the feedback in the thermal domain, Q_{hot} will be heated until this voltage is equal to zero, in which case $V_{be,amb} - V_{be,hot} = IR_1$. This voltage difference corresponds to the required overheat, which can then be expressed as $\Delta T = -IR_1/S_{Vbe}$. For an overheat of 10K, R_1 is therefore about 220Ω.

Even when they are at the same temperature, there will be a V_{be} mismatch between the two transistors. This is mainly due to mismatch in their saturation currents (Section 2.5.2), and can be compensated for by trimming the emitter current of Q_{amb} via R_4. This ensures that both transistor's are biased at the same operating point (Section 2.5.2), and therefore should have similar temperature sensing characteristics.

4.6 Experimental Results

4.6.1 Modulator Performance

The hot transistor was soldered to a PCB in the manner illustrated in Fig. 4-8. The pad exposed to the flow was circular with a diameter of 15mm. The hot transistor was operated at an overheat ΔT of approximately 5K and P_{ref} = 150mW. In still air, the sensor dissipates about 50mW. Under these conditions, the power spectrum of the modulator's bitstream is shown in Fig. 4-22. The noise floor observed below approximately 100Hz is due to the thermal noise of the interface electronics. The noise floor is so low that in order to measure it, the hot transistor had to be shielded from random air currents. In accordance with the simulations, the slope of the quantization noise at higher frequencies is slightly in excess of 20dB/decade. At clock frequencies ranging from 1 to 20kHz, no dead bands or signs of instability were observed.

Also shown in Fig. 4-22 is the power spectrum obtained when the integrator was bypassed, in effect realizing the basic modulator shown in

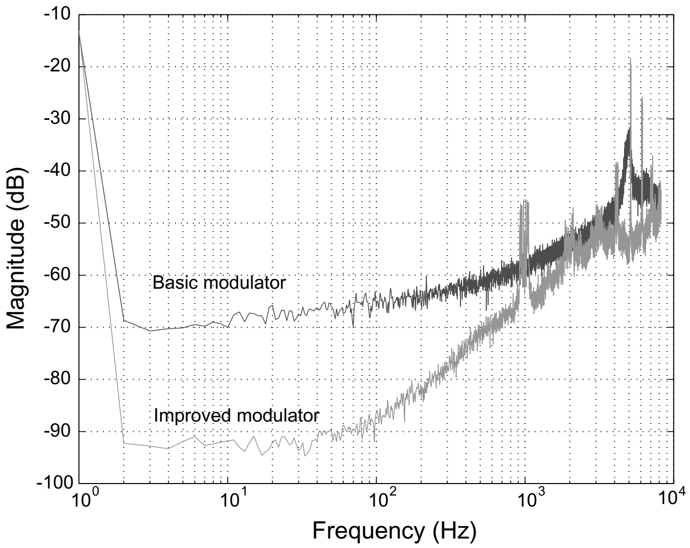

Figure 4-22 *Measured power spectrum of a differential modulator (Hann windowed average of 16, 16kbit segments).*

Fig. 4-2. In this case, the modulator's noise floor is clearly limited by quantization noise, due to the relatively gentle roll-off of the transistor's thermal impedance. During the modulator's start-up transient, the large dead band around $\mu = 0.5$ predicted by both theory and simulations could be clearly seen.

4.6.2 Wind Tunnel Testing

For wind tunnel measurements, the hot transistor, mounted on a circular PCB was built into the aerodynamic housing of a commercial wind sensor. The latter is described in more detail in section 5.1. The resulting sensor characteristic, i.e., the bitstream average as a function of flow speed, is shown in Fig. 4-23. Also shown is the best fit to a square-root-law characteristic, assuming that the sensor obeys King's Law. The agreement between the curves shows that the modulator does indeed operate the HTA in CTD mode. At the maximum flow speed of 15m/s, the modulator's 10-bit resolution corresponds to a flow-sensing resolution of about 0.04m/s.

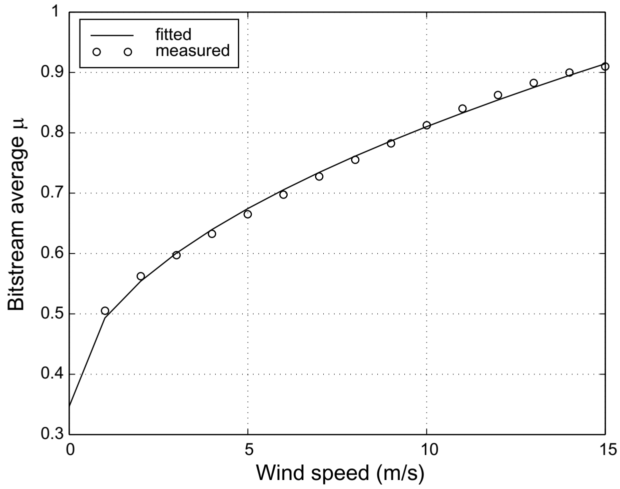

Figure 4-23 *Bitstream average vs. wind speed*.

The transient response of the HTA was measured by manually interrupting the flow. Due to the extra thermal capacitance of the PCB, the HTA takes about a minute to fully settle after a rapid change in flow speed. Much better transient performance was obtained by exposing the transistor directly to the flow, as shown in Fig. 4-7. The resulting step response was then much faster, with a time constant of about 2 seconds (Fig. 4-24).

4.7 Conclusions

Thermal anemometers based on a pair of robust and inexpensive off-the-shelf transistors have been described. One of the transistors is self-heated while the other is used as an ambient temperature sensor. The hot transistor is read out by incorporating it in the feedback loop of a thermal sigma-delta modulator. Since the thermal inertia of the transistor does not provide enough filtering, an electrical integrator was included in the loop. At a clock frequency of 16384Hz, when a 4096-tap sinc^2 decimation filter is used, the modulator's simulated resolution is at the 10-bit level. Wind tunnel measurements showed that the modulator exhibits a square-root-

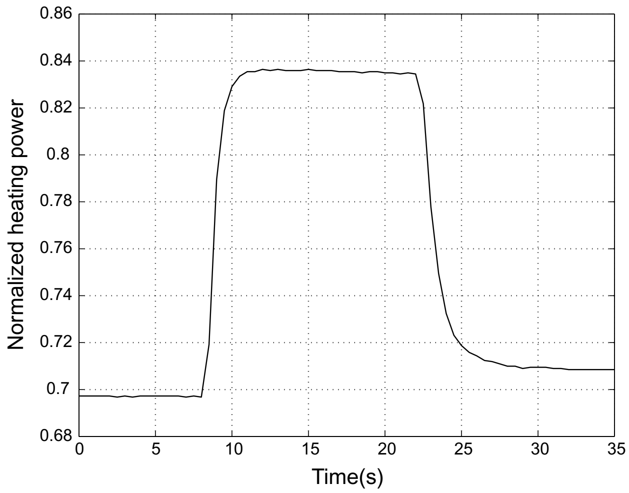

Figure 4-24 *Modulator response to a transient change (of about 5m/s) in flow speed.*

law characteristic, which indicates that the modulator effectively operates the anemometer in CTD mode. The anemometer's transient response is determined by the way the hot transistor is mounted. The time constant of a hot transistor in a free-standing SOT-89 package is about 2 seconds.

4.8 References

[4.1] L.E. MacHattie, "The transistor as an anemometer," *Journal of Physics E: Scientific-Instruments*, vol.12, no.8, pp.754-60, Aug. 1979.

[4.2] L.E. MacHattie, "A transistor anemometer," *Journal of Physics E: Scientific-Instruments*, vol.14, no.1, pp. 80-2, Jan. 1981.

[4.3] S. Woodward, "Self-heated transistor digitizes airflow," *EDN*, vol. 41, no. 6, March 14, 1996.

[4.4] Y. Pan and J.H. Huijsing, "New integrated gas-flow sensor with duty cycle output," *Electronics Letters*, vol. 24, no. 9, pp. 542-543, April 1988.

[4.5] L. Castañer, V. Jimenez, M. Domínguez, F. Masana and A. Rodriguez, "A conduction-convection design for liquid flow sensing," *Sensors and Actuators A: Physical*, vol. 66, no. 1-3, pp. 131-137, April 1998.

[4.6] M. Domínguez, F. Masana, V. Jimenez, S. Bermejo, J. Amirola, J. Ballester, N. Fueyo and L. Castañer, "Low-cost thermal TΣΔ airflow sensor," *IEEE Sensors Journal*, vol. 2, no. 5, pp. 453–462, October 2002.

[4.7] P. Bruschi, D. Navarrini and M. Piotto, "A flow sensor for liquids based on a single temperature sensor operated in pulsed mode," *Sensors and Actuators A: Physical*, vol. 110, no. 1-3, pp. 269-275, Feb. 2004.

[4.8] Analog Devices Inc., "TMP12: Airflow and temperature sensor data sheet," Feb. 2002.

[4.9] J. Christensen, "Low-cost anemometer fights dust," *EDN*, vol. 46, no. 19, pp. 102-103, Aug. 2001.

[4.10] Qin-Yi Tong and Jin-Biao Huang, "A novel CMOS flow sensor with constant chip temperature (CCT) operation," *Sensors and Actuators A: Physical*, vol. 12, no. 1, pp. 9-21, July 1987.

[4.11] M. Domínguez and L. Castañer, "Bounding of thermal Σ–Δ modulators' output for sensors," *Proc. ISCAS '99*, vol. 2, pp. 244-247, June 1999.

[4.12] H.-J Verhoeven, "Smart thermal flow sensors," Ph.D. Thesis, Delft University of Technology, 1996.

[4.13] R.D. Hughes, "Remote diodes yield accurate temperature measurements," *EDN*, vol. 48, no. 15, pp. 59-62, July 10, 2003.

[4.14] R.M. Fox and S.-G. Lee, "Scalable small-signal models for BJT self-heating," *IEEE Electron Device Letters*, vol. 12, no. 12, pp. 649-651, Dec. 1991.

[4.15] D.T. Zweidinger, S.-G. Lee and R.M. Fox, "Compact modeling of BJT self-heating in SPICE," *IEEE Transactions on Computer-Aided Design of Integrated Circuits and Systems*, vol. 12, no. 9, pp. 1368 –1375, Sept. 1993.

[4.16] T. Veijola, "Simple Model for Thermal Spreading Impedance," *Proc. of BEC'96*, pp. 73-76, October 1996.

[4.17] H. Mnif, T. Zimmer, J.L. Battaglia and B. Ardouin, "Modeling the self-heating effect in SiGe HBTs," *Proc. of BCTM 2002*, pp. 96-99, Sept. 2002.

[4.18] M. Glavanovics and H. Zitta, "Thermal destruction testing: an indirect approach to a simple dynamic thermal model of smart power switches," *Proc. of ESSCIRC '01*, pp. 236-239, Sept. 2001.

[4.19] M. Narz and P. Nance, "Thermal modeling of power-electronic systems," *Infineon Technologies Application Note*, Jan. 1998.

[4.20] S.R. Norsworthy, R. Schreier and G.C. Temes, "Delta-sigma data converters," IEEE press, 1997.

A Smart CMOS Wind Sensor 5

This chapter describes the design and development of a smart wind sensor in a standard CMOS process. It is an improved version of a commercially available silicon wind sensor, whose interface electronics was implemented with discrete components and required manual trimming, thereby significantly increasing the size and cost of the total wind sensor system. In contrast, the interface electronics of the smart wind sensor is integrated on the same chip as the sensor and does not require manual trimming. This was done without increasing the sensor's area, and hence its cost, by using a new interface architecture consisting of three thermal sigma-delta modulators. One modulator regulates the sensor’s temperature, while the other two digitize orthogonal components of its flow-dependent heat loss. The bitstream outputs of the latter are decimated by an external microprocessor, and used to compute wind speed and direction. Measurements in a wind tunnel show that the performance of the smart sensor is at least as good as that of its predecessor (errors in wind speed and direction less than ±(0.5m/s +3%) and $\pm 3^{o}$ respectively over the range 0.5 to 25m/s). Since it has no moving parts, and thus requires very little maintenance, this sensor is well suited for meteorological applications.

5.1 A First-Generation Wind Sensor

In previous work, a first generation silicon wind sensor for meteorological applications has been developed and successfully commercialized [5.1, 5.2, 5.3]. Its performance is similar to that of the traditional combination of a cup anemometer and a wind vane, but requires no moving parts. The

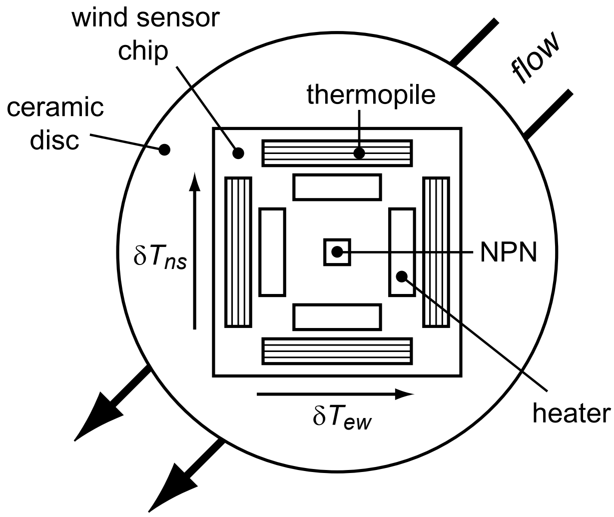

Figure 5-1 *Schematic diagram of a first-generation wind sensor.*

sensor consists of a square chip, on which four heaters, four thermopiles, and an NPN transistor have been integrated (Fig. 5-1). The chip is protected from direct contact with the airflow by bonding it to one side of a thin ceramic disc. By heating the chip, a hot spot is created on the surface of the disc. Airflow over the other side of the disc will then cool it asymmetrically, and thus induce a net temperature gradient $\delta \boldsymbol{T}$ across the chip. The magnitude of $\delta \boldsymbol{T}$ is a function of flow speed, while its direction is that of the flow. Orthogonal components (δT_{ns} and δT_{ew}) of this gradient are measured by the thermopiles, and their outputs used to determine wind speed and direction [5.1]. A more detailed description of the sensor's operation is given in Section 2.3.1.

The sensor is mounted in an aerodynamic housing (Fig. 5-2), which consists of three equiplanar discs: a small inner disc surrounded by two larger outer discs. The ceramic disc bearing the sensor is mounted flush with the upper surface of the inner disc (Fig. 5-3). The two outer discs serve to guide airflow over the inner disc in a well-defined manner and reduce the influence of vertical wind components or sensor tilt on the computed wind speed and direction [5.1].

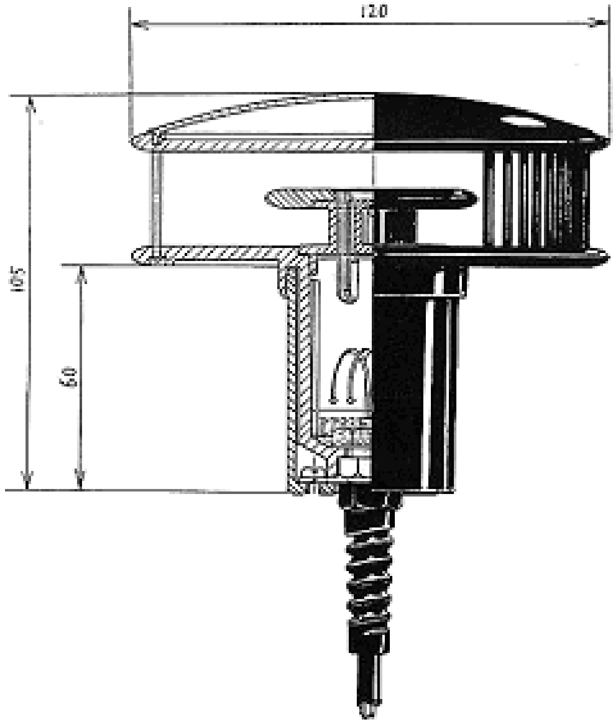

Figure 5-2 *The wind sensor's aerodynamic housing.*

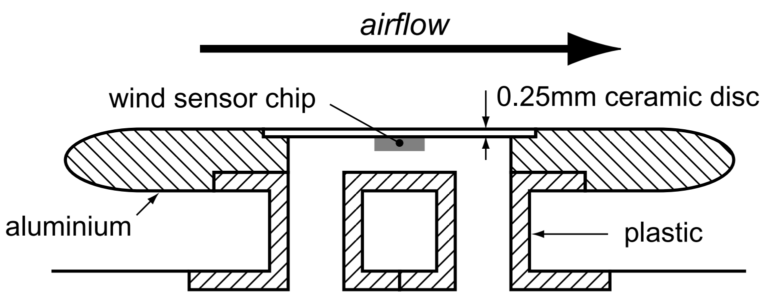

Figure 5-3 *Cross-sectional view of the inner disc.*

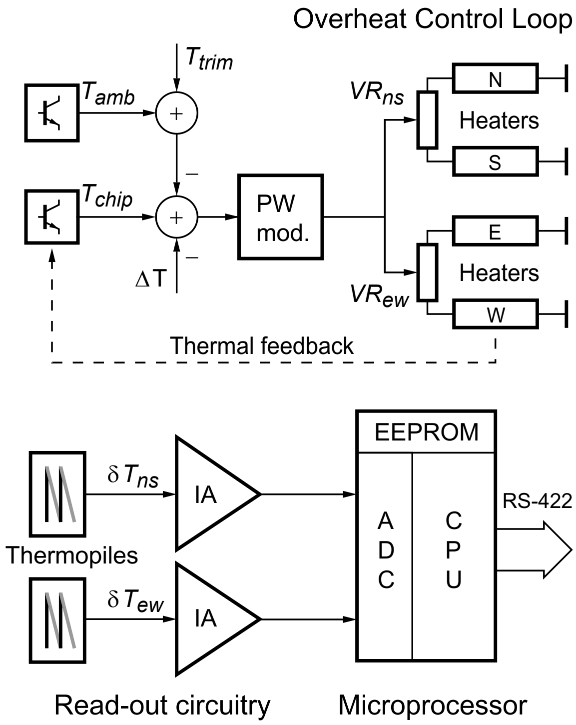

Figure 5-4 *Interface electronics of the first-generation sensor.*

5.1.1 First-generation Interface Electronics

A block diagram of the first-generation wind sensor's interface electronics is shown in Fig. 5-4. It consists of three parts: an overheat control loop, thermopile read-out circuitry, and a microprocessor.

For fast transient response (Section 2.3.2), the overheat control loop maintains the average temperature of the chip T_{chip} at a constant overheat ΔT (~16K) above ambient temperature T_{amb}. Using V_{be} sensing (Section 2.5.2), the absolute temperatures T_{chip} and T_{amb} are measured by the on-chip transistor and an external transistor. Due to the limited accuracy of V_{be} sensing, however, errors of several degrees may occur and therefore, the actual overheat must be set by trimming. The control loop is completed by a pulse-width modulator (PWM) that efficiently drives the heaters with a stream of fixed amplitude pulses. The frequency of these pulses is high enough (~10kHz) to ensure that their AC component is filtered out by the sensor's thermal inertia – which behaves like a low-pass filter in the thermal domain.

The thermopile read-out circuitry digitizes the thermopile signals. Since they measure the same component of the flow-induced temperature gradient, thermopiles on opposite sides of the chip are connected in series. This effectively doubles their output signal. Despite this, the flow-induced temperature differences are quite small (in the millikelvin range) and so are the resulting signals (in the microvolt range). These signals are then boosted by low-offset instrumentation amplifiers before being applied to the microprocessor's ADC. This has an effective resolution of 9-bits, which is sufficient to meet the sensor's inaccuracy specifications.

Although the thermopiles have no intrinsic offset, thermal asymmetry in the packaged sensor will give rise to a zero-flow offset in their output signals [5.4, 5.5]. To compensate for this packaging asymmetry, the heat distribution in the chip is *manually* trimmed via two potentiometers connected to the north-south and east-west heater pairs (Fig. 5-1). These are adjusted such that at zero flow, the thermopile outputs, and hence the temperature differences δT_{ns} and δT_{ew}, are nulled. This process effectively aligns the centre of the hot spot with the geometric centre of the chip.

Other sources of error are the instrumentation amplifiers' offset and gain errors, and the thermopiles' process-dependent sensitivity. To compensate for these errors, each wind sensor is calibrated in a wind tunnel. The calibration data is used to generate a correction look-up table, which is stored in an EEPROM (Fig. 5-4). This information is used by the microprocessor to perform a gain and offset correction on the digitized thermopile signals [5.3]. After this digital trim, the sensor's inaccuracy will be less than ±(0.5m/s +3%) and ±3^{o} respectively over the range 0.5 to 25m/s. The computed wind speed and direction are communicated to the outside world via an RS-422 serial interface.

5.1.2 Why a Smart Wind Sensor?

Although the performance of the first-generation wind sensor is good enough for its intended meteorological application, its interface architecture suffers from a number of drawbacks. Firstly, transferring the microvolt-level thermopile signals off-chip significantly increases their susceptibility to interference, e.g. from parasitic thermocouples or mains pick-up. Secondly, the discrete-component implementation of the required circuitry adds significantly to the size and cost of the sensor system. Finally, and perhaps most significantly, the trimming required to set the overheat and to compensate for packaging asymmetry, significantly increase the sensor's production time, and hence its cost.

The first two drawbacks can be circumvented by integrating the interface electronics on the wind sensor chip, i.e., by designing a smart wind sensor. This approach, however, does not address the third drawback: the need for trimming. This requires an improved interface architecture, the development of which is described in the following section.

5.2 Smart Wind Sensor Design

In the design of a smart wind sensor, the main objectives were to integrate the interface electronics on the same chip as the sensor, and eliminate the need for trimming and *without* compromising the sensor’s performance. For reference, the key specifications of the first-generation wind sensor are given in Table 5-1, [5.6].

Table 5-1 *System specifications of the first-generation wind sensor*

Parameter	Specification
Chip size	4mm x 4mm
Inaccuracy (speed) @ 20ºC	±(0.5m/s +3%)
Inaccuracy (direction) @ 20ºC	±3º
Operating range	0.5 to 25m/s
Operating temperature	−25º to +70º

5.2.1 A CMOS Wind Sensor

The wind sensor's most important specification is its accuracy, which is determined by its size and layout [5.1]. Maintaining this specification, therefore, means that the sensor's layout should not be changed. The interface electronics must then be compact enough to fit into the unused space in the middle of the chip (see Fig. 5-1).

In order to accurately process the thermopile signals, the offset of the interface circuitry must be at the microvolt level. This can only be achieved by using dynamic offset-cancellation techniques, which, in turn, are best implemented in a CMOS process. Since the first-generation sensor was realized in a *bipolar* process, this design choice requires a re-design of the wind sensor.

The absolute temperature of a CMOS wind sensor can again be measured by a bipolar transistor: the substrate PNP transistor available in most CMOS process. Also, p^+silicon/aluminium thermopiles can again be used, as these provide the best signal-to-noise ratio in a CMOS process [5.7]. Another advantage of these thermopiles is the fact that their p^+silicon arms are realized in an n-well, which then serves as an electrostatic shield against substrate noise. Although the heaters can be realized either as diffusion or as polysilicon resistors, the latter are preferable, since they are isolated from the substrate and thus minimize the cross-talk between the (large) heater currents and the thermopiles. Since the insulating oxide is quite thin, the extra *thermal* insulation can be neglected.

The power dissipated by on-chip circuitry may also be a significant source of (thermal) interference. If this is constant, it will simply offset the power dissipated in the heaters. Variations, however, will cause temperature differences in the sensor which are indistinguishable from those induced by the wind. Given the desired accuracy, such variations should be less than a few milliwatts, since the sensor's total heating power is about 0.6W.

5.2.2 A Second-generation Wind Sensor

To investigate the possibility of integrating a (modified) version of the first-generation interface architecture, a CMOS wind sensor with a low-offset instrumentation amplifier was realized [5.8]. It is the same size

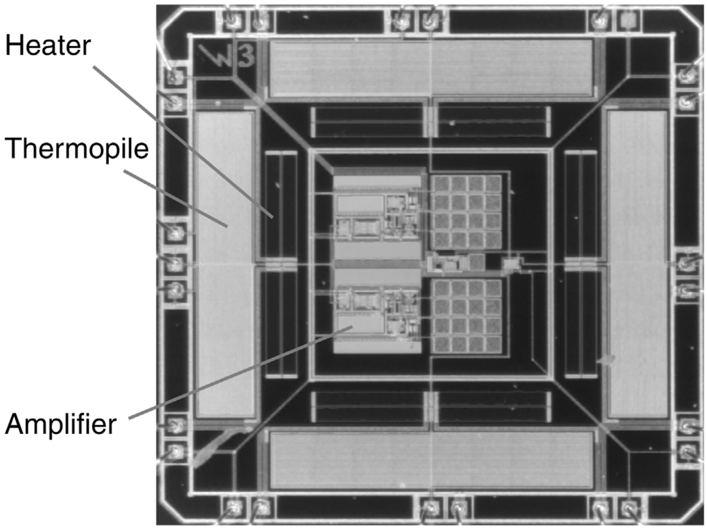

Figure 5-5 Micrograph of a second-generation wind sensor chip.

($16mm^2$) and has the same layout as the first-generation sensor, except for the presence of on-chip circuitry. Since the circuitry is located in a thin layer at the surface of the chip, however, it does not significantly affect heat flow in the sensor, which mainly takes place via the substrate [5.9].

As discussed above, the heaters were realized as polysilicon resistors, each with a nominal resistance of 200Ω. Each thermopile consists of twelve p^+/aluminium thermocouples, and has an estimated sensitivity of 6mV/K and a nominal resistance of 71kΩ. The outputs of the thermopile pairs were connected, via a multiplexer, to the input of the instrumentation amplifier. The amplifier has a gain of 100 and, through the use of chopping, its offset is less than 20μV.

A micrograph of this chip, which was fabricated in a 1.6μm single-poly double-metal CMOS process, is shown in Fig. 5-5. It is clear that no chip area is left to implement the rest (overheat control loop, ADC) of the first-generation interface architecture. Although more circuitry could be implemented by using a denser (and more expensive) process, the problem of trimming would still need to be solved.

5.2.3 An Improved Interface Architecture

One way to eliminate the overheat trim is by operating the sensor in constant power (CP) mode. This will, however, increase the response time of the sensor system and result in a non-square-root law characteristic (Section 2.3.3). The latter is undesirable as it will require significant modification of the microprocessor's signal processing firmware (which was optimized for a square-root-law characteristic).

Another way to eliminate the overheat trim, while still operating the sensor in CTD mode, is by decreasing the temperature sensing errors that make trimming necessary. This can be done by using ΔV_{be} sensing (as opposed to V_{be} sensing) to establish the overheat (Section 2.5.2). Using this technique, overheat errors can be reduced to a few degrees. Although the residual error will cause proportional variations in the sensor's sensitivity (which is proportional to ΔT), such variations are tolerable because (like the first generation sensor) each sensor will be calibrated and digitally trimmed.

The *manual* packaging-asymmetry trim can be eliminated by operating the sensor in temperature balance (TB) mode (Section 2.3.4). In this mode, the heat distribution in the sensor is dynamically adjusted such that any temperature gradients are cancelled, thus automatically centring the hot spot. The heat distribution in the sensor will now be flow-dependent, with an offset representing the heating power required to compensate for packaging asymmetry. This offset can be determined during calibration and eliminated by the sensor's *digital* trim. Using this approach, wind speed and direction can then be determined by measuring the power dissipated in each heater [5.10].

Operation in TB mode requires a control loop that monitors the on-chip temperature gradient and drives the heaters accordingly. As discussed in Section 3.2, such a control loop can be advantageously realized as a *differential* thermal sigma-delta (TΣΔ) modulator. Since the thermopiles sense orthogonal components of an on-chip temperature gradient, two such modulators are required to cancel these components.

In order to obtain a square-root law characteristic, the sensor's overheat must be regulated (Section 2.3.4). This requires an overheat control loop,

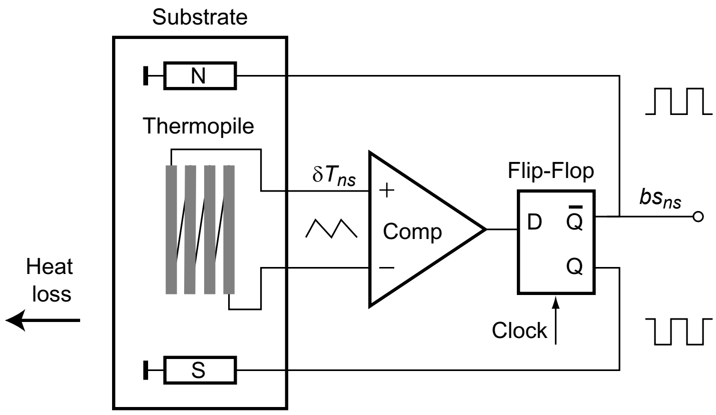

Figure 5-6 The north-south differential TΣΔ modulator.

which can also be implemented as a TΣΔ modulator. This modulator will be referred to as the *common-mode* modulator, since it regulates the sensor's average, or common-mode, temperature.

The main advantage of this TΣΔ modulator-based interface architecture is that it is extremely compact. In addition to the heaters and temperature sensors of the flow sensor itself, the implementation of each modulator only requires the implementation of a clocked comparator (Section 3.1). In addition, the power dissipation of the required circuitry is low, since the heaters are efficiently driven by constant-power pulses.

5.2.4 Operation of the Differential Modulators

A block diagram of the north-south differential modulator is shown in Fig. 5-6. The modulator drives the north-south temperature difference δT_{ns} towards zero by applying constant-power heat pulses to either the north or the south heater. If the clock frequency is high enough, the AC component of these pulses will be filtered out by the sensor's thermal inertia and so $\delta T_{ns} \cong 0$. The differential power dissipation δP_{ns} will then exactly balance the north-south component of the sensor's asymmetric heat loss to the flow. The output of the modulator is a bitstream $bs_{ns} \in \{-1, 1\}$ whose

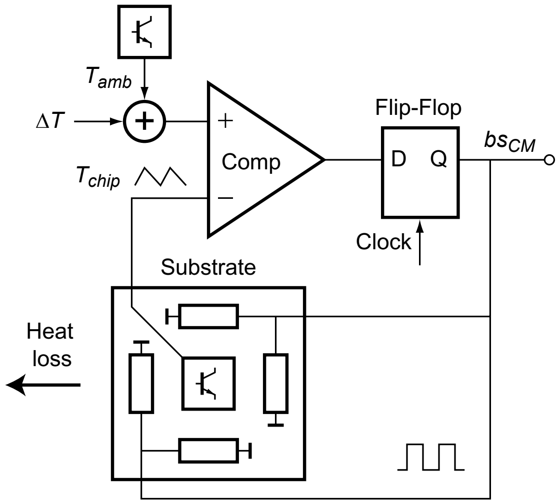

Figure 5-7 Common-mode TΣΔ modulator.

average μ_{ns} represents the normalized differential power $\delta P_{ns}/P_{ref}$, where P_{ref} is the average power dissipated in a heater by a heat pulse.

In a similar manner, the east-west component of the sensor's differential heat loss δP_{ew} can be digitized by a second east-west differential modulator that drives the east and west heaters. Together, the two differential modulators operate the wind sensor in CP mode. This is because during every clock cycle, exactly two heaters will always be driven and therefore the total heat dissipated in the sensor will be constant.

5.2.5 Operation of the Common-Mode Modulator

A block diagram of the common-mode (CM) TΣΔ modulator is shown in Fig. 5-7. Its bitstream output $bs_{cm} \in \{0, 1\}$ drives all four heaters in such a way that the chip's average temperature $T_{chip} \cong T_{amb} + \Delta T$.

The modulator's bitstream average μ_{cm} is then determined by the common-mode heating power $P_{cm} = \mu_{cm} P_{ref,cm}$ required to maintain the overheat, where $P_{ref,cm} = 4P_{ref}$ is the constant power dissipated in the four heaters when $bs_{cm} = 1$. Then from King's Law:

$$\mu_{cm} = \frac{P_{cm}}{P_{ref,\,cm}} = \frac{(C + D\sqrt{U})\Delta T}{P_{ref,\,cm}} \tag{5-1}$$

where U is the wind speed and C and D are experimentally determined constants that depend on sensor geometry and the physical properties of air. From Section 2.3.3, since the sensor is operating in CTD-TB mode, the bitstream averages of the differential modulators are given by:

$$\mu_{ns} = \frac{\delta P_{ns}}{P_{ref}} = \frac{E\sqrt{U_{ns}}\Delta T}{P_{ref}} \tag{5-2}$$

$$\mu_{ew} = \frac{\delta P_{ew}}{P_{ref}} = \frac{E\sqrt{U_{ew}}\Delta T}{P_{ref}} \tag{5-3}$$

where E is a sensor constant. In this mode, the smart wind sensor, like the first-generation sensor, also has a square root law characteristic.

In principle, wind speed could also be determined from μ_{cm}, using (5-1). However, this equation involves a *second* sensor constant and is thus less well defined than (5-2) and (5-3).

5.2.6 Combining the Modulator Outputs

An interesting question is then: how can the bitstream outputs of the CM modulator and differential modulators be combined in order to operate the sensor in CTD mode? The simplest way of doing this is to use the CM bitstream to briefly interrupt the constant power heating of the differential modulators. As shown in Fig. 5-8 for the north-south modulator, this may be achieved by inserting a bitstream multiplier in the feedback loop of each differential modulator. The modulator output will then be a ternary bitstream $bs_{ns,out} \in \{-1,0,1\}$ whose average $\mu_{ns,out}$ is, once more, equal to $\delta P_{ns}/P_{ref}$. In a similar manner, $\delta P_{ew}/P_{ref}$ can be obtained from the output

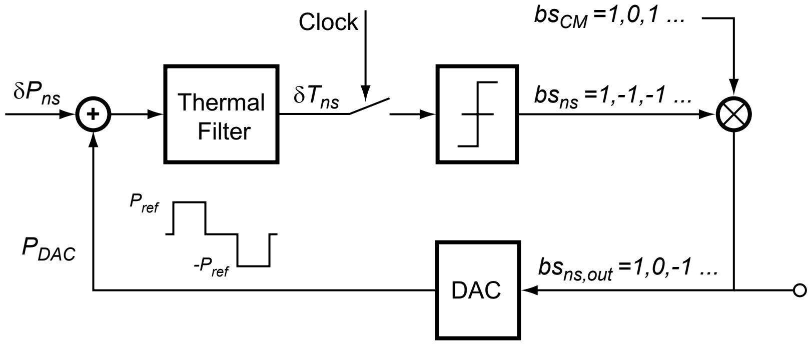

Figure 5-8 Combining the heat pulses of the CM and differential modulators.

of the modified east-west modulator. Then using (5-2) and (5-3) wind speed and direction can again be determined [5.10].

The multiplication of two bitstreams, however, each of which contains large amounts of shaped quantization noise, will result in signal-dependent intermodulation products, some of which may be in the signal band. In turn, these will increase the in-band noise present in $bs_{ns,out}$ at certain (unpredictable) combinations of input signals.

A better way of combining the bitstream outputs of the CM and differential modulators is by time-multiplexing, as shown in Fig. 5-9. Here, the differential modulators drive the heaters during an interval T_d, while the CM modulator drives the heaters during the rest of the clock period T. As before, the bitstream outputs of the differential modulators provide information about the sensor's differential heat loss and from (5-2) and (5-3), wind speed and direction can be determined [5.11].

Ideally, the common-mode heat pulses will not heat the sensor differentially. Due to packaging asymmetry, however, there will be a certain amount of common-mode to differential crosstalk. This will take the form of a small additive noise component, that, furthermore, has been shaped by the CM modulator and then been low-pass filtered by the

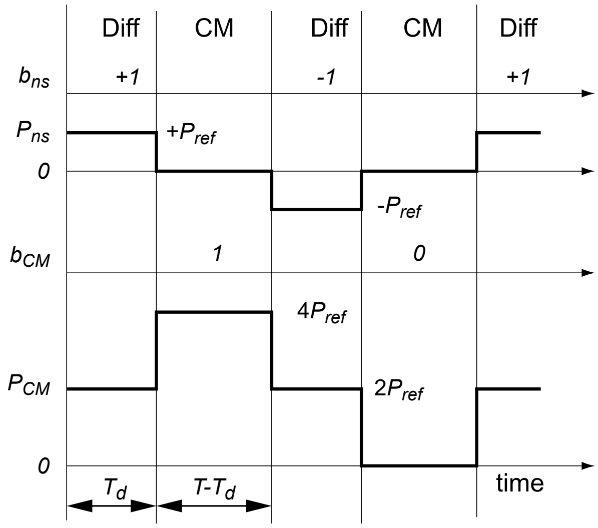

Figure 5-9 Time-multiplexed heater drive.

sensor's thermal inertia. As such, it will not increase the differential modulators' noise floor significantly.

The use of time-multiplexing also provides a means of independently scaling the dynamic ranges of the CM and differential modulators. This can be done simply by adjusting the ratio between T_d and T. Such scaling is necessary in practice, because the sensor's common-mode heat loss is significantly larger than its differential heat loss. From Fig. 5-9, the reference heating power (averaged over one clock cycle) of the differential modulators $P_{ref,d}$ is given by:

$$P_{ref,d} = P_{ref}(T_d/T) \tag{5-4}$$

where P_{ref} is the instantaneous power dissipation in one heater. Similarly, the reference heating power of the CM modulator $P_{ref,cm}$ is given by:

$$P_{ref,cm} = 4P_{ref}(1 - T_d/T) \tag{5-5}$$

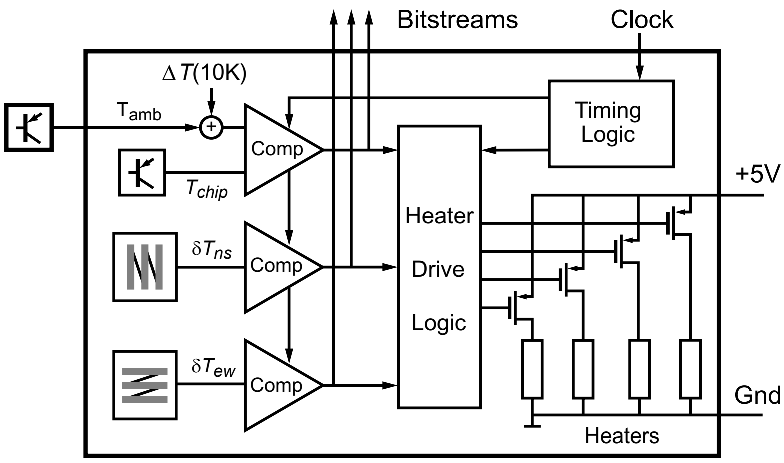

Figure 5-10 *Block diagram of the smart wind sensor.*

Taking into account the fact that the differential modulators' heat pulses also cause (constant) common-mode heating, then the total common-mode heating power dissipated in the sensor P_{cm} is given by:

$$\begin{aligned} P_{cm} &= 2P_{ref,d} + \mu_{cm} P_{ref,cm} \\ &= P_{ref}(2T_d/T + 4\mu_{cm}(1 - T_d/T)) \end{aligned} \quad (5\text{-}6)$$

The constant term in (5-6) implies that the CM modulator can only adjust P_{cm} over a limited range, since $0 < \mu_{cm} < 1$. As long as this range is not too small, this is not a problem, since the heating power required to maintain a given overheat also has a limited range (King's law). Measurements on the first-generation sensor [5.10], show that the heating power at zero flow is about 80% of that required at 25m/s. If, for example, $T_d = T/2$ then $P_{ref,d} = 0.5P_{ref}$, $P_{ref,cm} = 2P_{ref}$ and from (5-6), $P_{ref} < P_{cm} < 3P_{ref}$ which is a wide enough range.

5.2.7 A Smart Wind Sensor

A block diagram of the complete smart wind sensor is shown in Fig. 5-10. As discussed above, two differential TΣΔ modulators cancel the flow-induced temperature differences δT_{ns} and δT_{ew}. Each modulator consists of a latched comparator, connected to the appropriate thermopile pair. The sensor's overheat is regulated by a CM modulator, consisting of a third comparator and two bipolar transistors that sense the temperature of the chip T_{chip} and that of the flow T_{amb}.

Via the heater drive logic, the bitstream outputs of the three modulators drive the heaters in the time-multiplexed manner described in the previous section. To minimize on-chip power dissipation, the heaters are driven from an externally-regulated 5V supply. This also avoids the problem of thermal crosstalk between the heat pulses generated by the modulators and the output of an on-chip reference. For this reason, the overheat is also referred to an external reference voltage.

Variations in the absolute value of the heating resistors affects their power dissipation. This is compensated for by the sensor's (room temperature) calibration. To compensate for resistance variations over temperature, external resistors in series with the heaters can be used (Section 2.5.1) or since they are small, these variations may be simply tolerated.

The output of the smart wind sensor consists of the bitstream outputs of the three modulators. The output of the differential modulators represent orthogonal components of wind velocity, these are fed to an external microprocessor for decimation and computation of wind speed and direction. Although the output of the CM modulator is not used for flow sensing purposes, it provides information about the operation of the overheat control loop and may be used in future for self-testing purposes, as for instance in [5.12].

5.3 Modelling and Simulation of the Differential Modulators

The performance of the time-multiplexed interface architecture (Section 5.2.6) will mainly be determined by the performance of the differential modulators. This, in turn, will be determined by the oversampling ratio (OSR) and the degree of noise shaping provided by its loop filter. (The performance of the CM modulator is not a limiting factor, since its loop filter has a significantly smaller bandwidth than that of the differential modulators, and thus has better noise-shaping properties). As is the case for all sigma-delta modulators, modulator behaviour (resolution, linearity, signal swing at the comparator input etc.) can best be investigated by time-domain simulations. However, this requires an accurate model of the modulator's loop filter.

The loop filter of a differential modulator may be modelled as a thermal low-pass filter in cascade with an electrical low-pass filter. The thermal filter is the result of the thermal network formed by the sensor's geometry, while the electrical filter is the result of the resistances and parasitic capacitances of the thermopiles. In practice, the thermal filter has a much smaller bandwidth than the electrical filter, and so the loop filter is a predominantly thermal filter. In the following sub-sections a model of this electro-thermal loop filter will be determined.

5.3.1 Thermopile frequency response

Since the wind sensor's thermopiles are rather large (0.7mm^2), their parasitic capacitance significantly affects their frequency response. Each thermopile consists of N thermocouples, each of which generates a thermoelectric voltage v_{tc}. To a first approximation, the thermocouple's distributed capacitance C_{tc} can be modelled by two capacitances with values $C_{tc}/2$ located at either end of its lumped resistance R_{tc}. The resulting model of a thermopile is shown in Fig. 5-11. Since the thermocouples generate the same voltage, this model can be simplified by replacing each voltage source and resistance by its Norton equivalent (Fig. 5-11). From the result, the thermopile's output voltage v_o may be expressed in terms of the total thermoelectric voltage $v_{tp} = Nv_{tc}$ and the circuit's input impedance $Z_{line}(N, f)$ as:

$$v_o = (v_{tp}/R_{tp})Z_{line}(N,f) = v_{tp}H(N,f) \tag{5-7}$$

where R_{tp} is the total resistance of the thermopile. The generated thermoelectric voltage v_{tp} will therefore be filtered by the transfer function $H(N, f)$. For the thermopiles used in the wind sensor $N = 12$, $R_{tp} = 71\text{k}\Omega$, $C_{tc} = 32\text{pF}$ and the corresponding frequency response $H(12, f)$ is shown in Fig. 5-12. It is a low-pass filter with a gentle roll-off that begins at about

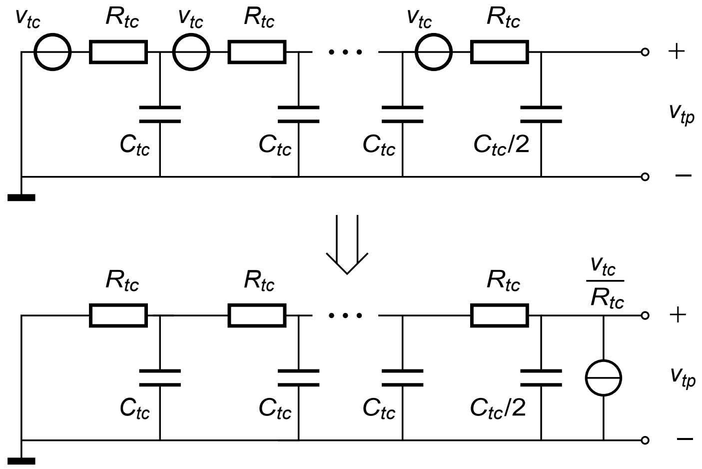

Figure 5-11 *Equivalent circuit of an integrated thermopile.*

10kHz, and a phase lag that remains relatively constant at 45^{o} over a wide range of frequencies.

By regarding a thermopile as an RC transmission line, a more accurate expression for its input impedance Z_{tp} may be obtained. From [5.13]:

$$Z_{tp} = \sqrt{\frac{R_{tp}}{j\omega C_{tp}}}\left(\frac{1 - e^{-2\sqrt{j\omega R_{tp} C_{tp}}}}{1 + e^{-2\sqrt{j\omega R_{tp} C_{tp}}}}\right) \qquad (5\text{-}8)$$

where C_{tp} is the thermopile's total capacitance. However, unlike the lumped component model, this result is not suitable for use in circuit simulators. Since a transmission line consists of an infinite number of lumped components, the accuracy of the lumped component model can be estimated by comparing $Z_{line}(12, f)$ with Z_{tp}, or equivalently by comparing $H(12, f)$ with $H(\infty, f)$. From Fig. 5-12, it can be seen that the lumped component model is accurate for frequencies ranging from DC up to a few hundred kilohertz, which is good enough for our purposes.

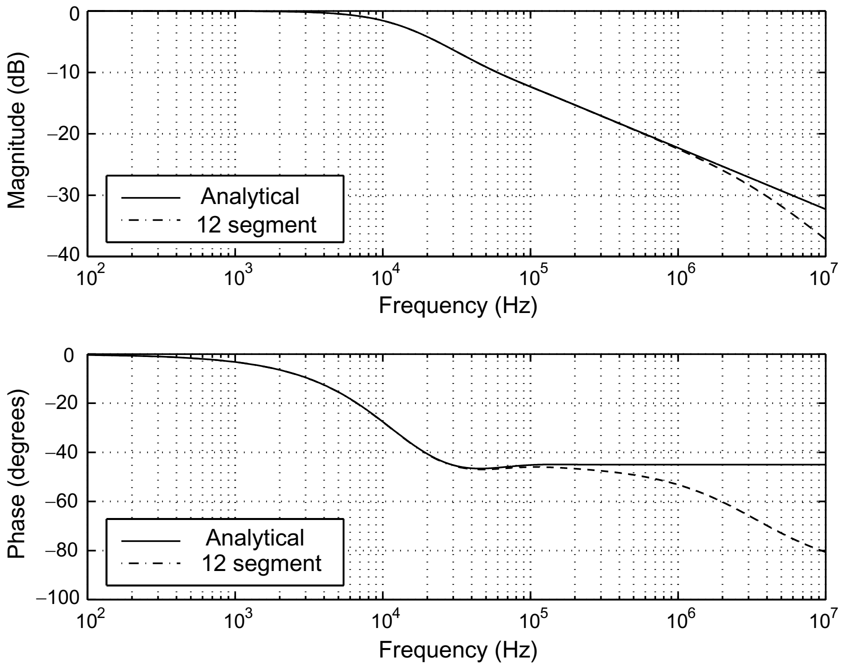

Figure 5-12 *Frequency response of an integrated thermopile.*

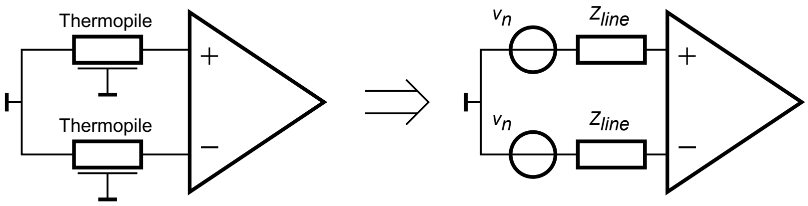

Figure 5-13 *Thermopile noise equivalent circuit.*

The equivalent noise resistance of the transmission line may be obtained by computing the real part of Z_{line}. This results in the equivalent circuit of Fig. 5-13, where the thermal noise v_n generated by the line is given by:

$$v_n^2 = 4kT\int_0^{\infty} Re(Z_{line}(f))df \tag{5-9}$$

By evaluating (5-9) numerically, the total noise contribution of both thermopiles at the input of the amplifier was calculated to be about 16µVrms. This is significantly higher than the 3.3µVrms predicted by a single-pole RC model, for which the noise would be given by kT/C_{tp}.

5.3.2 Modelling the Loop Filter

The main component of the differential modulators' loop filter is the thermal impedance Z_d that relates the heat dissipated in a heater to the temperature difference measured by the appropriate thermopile pair (Fig. 5-6). An analytical determination of this impedance is quite complicated, due to the fact that the distance between the heaters and the thermopiles is much larger than the thickness of the substrate and as a result, heat flow in the (thermally significant) ceramic disc must also be taken into account. Because of this, it was decided to derive a model of the loop filter experimentally, based on step-response measurements. An advantage of this approach is that it accurately incorporates all aspects of the sensor's thermal and electrical behaviour.

Since the thermopile signals are susceptible to external interference, the step-response measurements were made by using a wind sensor with an on-chip low-offset amplifier: the second-generation wind sensor described in Section 5.2.2. A heat step was applied to one of the heaters and the response of the appropriate thermopile pair was measured. The resulting step response is shown in Fig. 5-14 and is clearly that of a low-pass filter. From the step response, a compact model of the corresponding filter was derived using a special-purpose software tool: THERMODEL [5.14].

THERMODEL models a thermal filter as a distributed RC network having a continuous spectrum of time constants. An unknown filter's time constant spectrum is computed from its measured step response by a process of deconvolution, and the results used to derive the parameters of a compact electrical model. According to THERMODEL, the measured step response is the output of a passive *transfer* impedance. This is a natural consequence of the fact that the thermopiles measure a temperature difference between two points in the sensor (Section 3.3.2). The corresponding filter model is shown in Fig. 5-15, 20 RC sections were

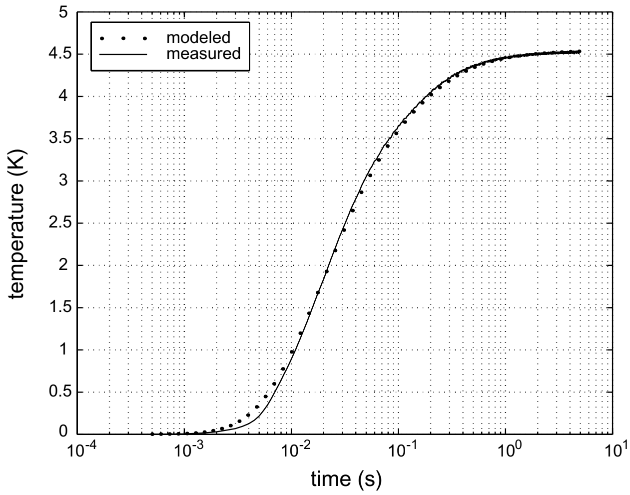

Figure 5-14 *Measured and modelled thermal step-response.*

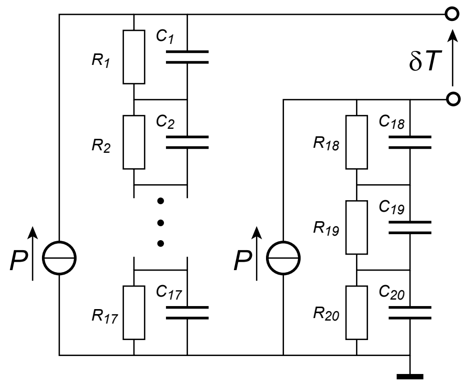

Figure 5-15 *Compact electrical model of the thermal filter Z_d.*

required to accurately model the measured step response. The current sources represent the power P dissipated in the heater, and the temperature difference ΔT is the output of the thermopile.

The measured and modelled unit-step responses of Z_d are compared in Fig. 5-14. They agree quite well, although some differences may be seen

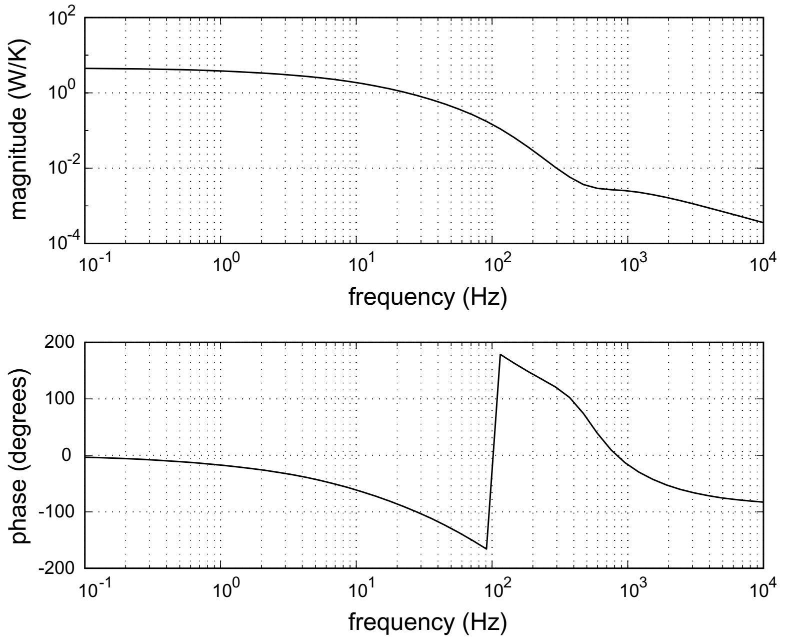

Figure 5-16 *Frequency response of the thermal filter Z_d.*

at the beginning of the step response. These are probably due to the influence of the 4kHz electrical low-pass filter used to remove artefacts at harmonics of the on-chip amplifier's 5kHz chopping frequency, or due to the finite resolution of the deconvolution process itself [5.15].

The frequency response obtained from the compact model is shown in Fig. 5-16. At DC, the thermal impedance Z_d has a finite value, while at high frequencies (above about 2kHz) it exhibits first-order roll-off. Examination of the phase plot shows that the filter exhibits first-order behaviour at frequencies above a few hundred hertz. Consequently, when clocked at these frequencies, the corresponding differential modulator will behave like a first-order modulator and will therefore be stable.

The phase lag introduced by the compact model at high frequencies must tend asymptotically to 90^{o}, since it consists of two RC impedances. This means that the extra phase shift introduced by the thermopile's low-pass

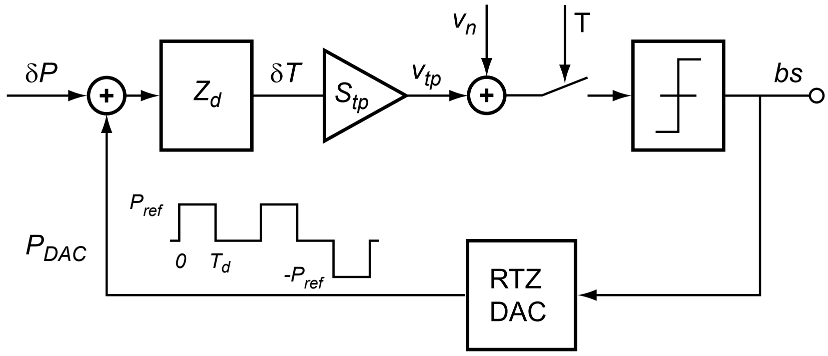

Figure 5-17 *Block diagram of the simulated differential modulator.*

characteristics at frequencies above approximately 10kHz (Fig. 5-12) will not be adequately modelled. However, since the highest frequency of interest in a TΣΔ modulator is at half the clock frequency i.e., $f_s/2$, the compact model can be used for simulations at clock frequencies up to about 20kHz. As will be seen in the following section, this is good enough for our purposes.

5.3.3 Simulation results

The compact model of the thermal filter Z_d shown in Fig. 5-15 was incorporated into a MATLAB simulation of a differential modulator (Fig. 5-17). The filter's input is the sum of a DC input signal δP and the output of the modulator's heaters (modelled as a DAC generating RTZ heat pulses). The resulting temperature difference δT is converted to the electrical domain by the sensitivity S_{tp} ~ 12mV/K of the series-connected thermopiles. To simulate the effect of thermal noise generated by the thermopiles and the comparator, white noise v_n was added to the comparator input. In addition, P_{ref} = 125mW, T_d = $T/2$, and the clock frequency $f_s = 1/T$ = 8192Hz.

The power spectrum of the simulated bitstream bs_{ns} is shown in Fig. 5-18. It can be seen that the thermal loop filter provides significant noise shaping at frequencies up to about 100Hz, where a pronounced peak occurs. This corresponds to the frequency at which the filter's phase

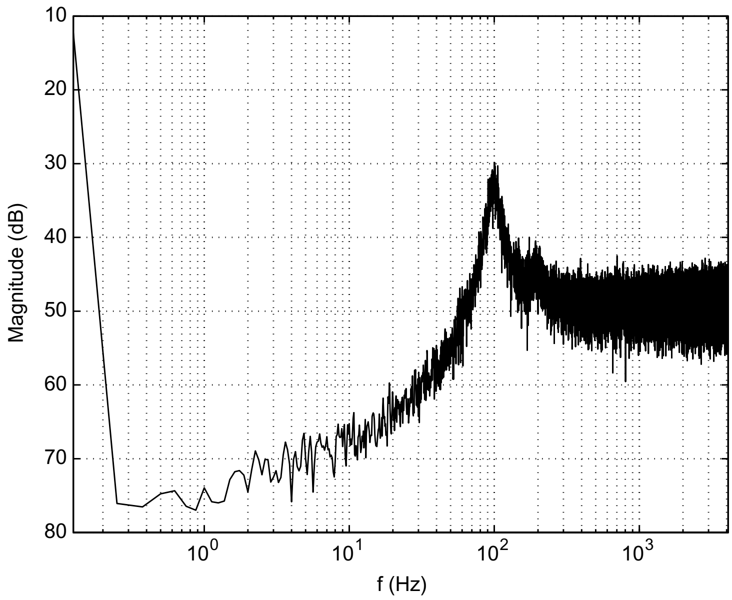

Figure 5-18 *Simulated power spectrum of a differential modulator (Hann windowed average of 6, 64kbit, bitstream segments with 50% overlap).*

response goes through -180^o (Fig. 5-16). The noise floor near DC is mainly determined by the added thermal noise. (This was set to 64μV (rms), a value which corresponds to the level in the implemented modulator.) This choice ensures that the thermal noise acts as a dither signal and breaks up unwanted baseband tones [5.16].

To obtain a bitstream average, the modulator output must be decimated by a digital low-pass filter. To maximize signal-to-noise ratio, the bandwidth of this filter should be minimized without, however, significantly slowing down the transient response of the sensor system. The dominant time-constant of the first-generation sensor's transient response is in the 1-2 second range [5.1, 5.6]. This is mainly due to the thermal inertia of the ceramic disc, and thus, should be the same for the smart sensor. Considering this, it was decided to limit the length of the filter's impulse response to 0.5 seconds.

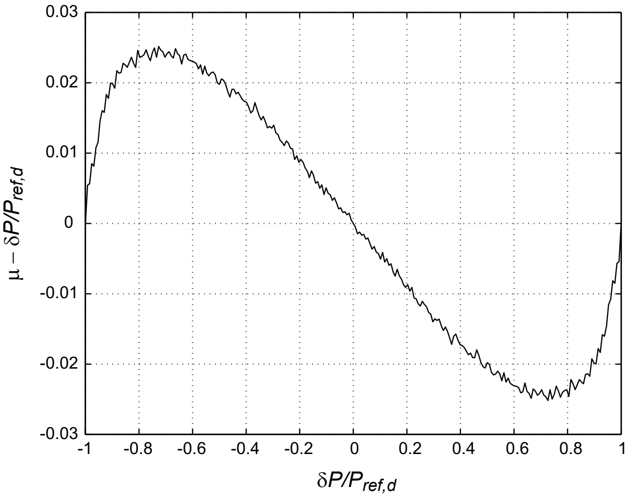

Figure 5-19 *Differential modulator non-linearity.*

Given this constraint, however, the peak in the modulator's NTF will not be sufficiently attenuated by a simple sinc^1 (rectangular) filter. Better results, are obtained with a sinc^2 (triangular) filter. Filtering the bitstream with a 4096-tap sinc^2 filter results in an estimated SNR of 63dB relative to $P_{ref,d}$. This is only 1dB less than the SNR obtained when an ideal brickwall filter with the same noise bandwidth is used. These results correspond to a modulator resolution of about 10-bits, taking into account the fact that the modulator's DC input range is $2P_{ref,d}$. This is enough to satisfy the wind sensor's inaccuracy specification (Section 5.2).

The modulator's DC transfer function was also examined, since this may be expected to exhibit some non-linearity due to integrator leak (Section 3.4). The the bitstream was decimated by a 4096-tap sinc^2 filter, and the simulations were done in the absence of thermal noise. The resulting quantization error $\mu - \delta P/P_{ref,d}$ is shown in Fig. 5-19. It may be seen that the modulator's DC characteristic is linear over a limited range around $\delta P = 0$, and in addition, exhibits a small gain error. This can be corrected for by applying a constant gain factor $\alpha = 1.045$ to the decimated modulator output, as shown in Fig. 5-20. It may be seen that the modulator

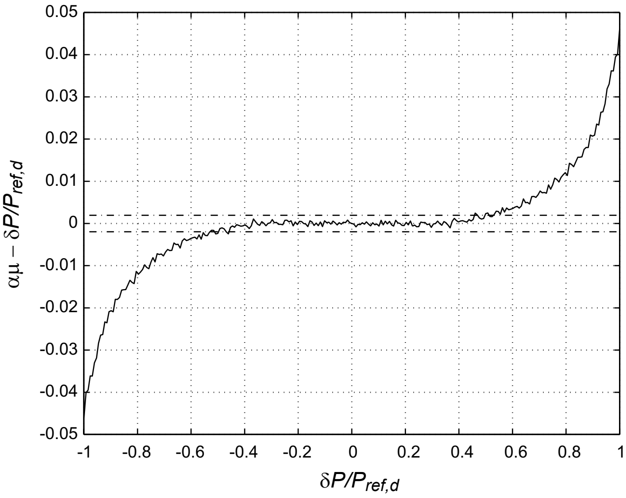

Figure 5-20 *Differential modulator non-linearity after gain correction, the dotted lines indicate the maximum deviation corresponding to 9-bit linearity.*

only achieves the required 9-bit resolution over roughly half of its input range. Added thermal noise at the comparator's input, however, acts as a dither signal [5.17], and increases the modulator's useful dynamic range to about 90% of the input range (Fig. 5-21).

The swing at the output of the thermal filter was also investigated. The simulation results (with the noise switched off) are shown in Fig. 5-22. Over the modulator's useful dynamic range, the amplitude of the thermal filter's output swing is only about 20mK, or 240μV at the output of the thermopiles. Compared to the sensor's 10K overheat, this small temperature swing confirms that the differential modulators will indeed operate the sensor in the TB mode.

5.4 Differential Modulator Design

As discussed in Section 5.2, the size and layout of the sensor chip are fixed by the flow sensor's specifications. As a result, its thermal filtering

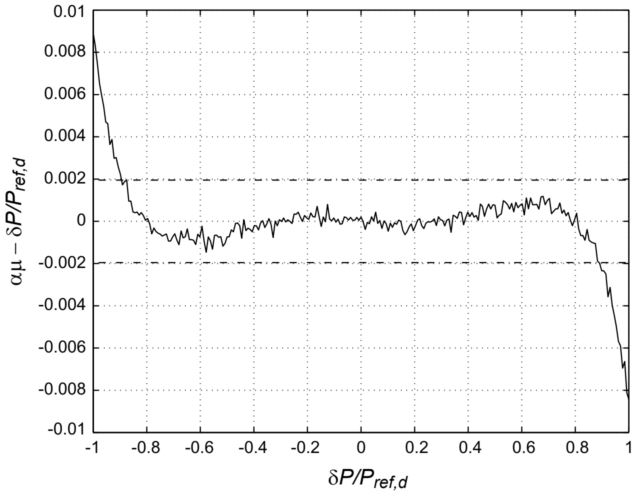

Figure 5-21 *Modulator non-linearity after dithering and gain correction, the dotted lines indicate the maximum deviation corresponding to 9-bit linearity.*

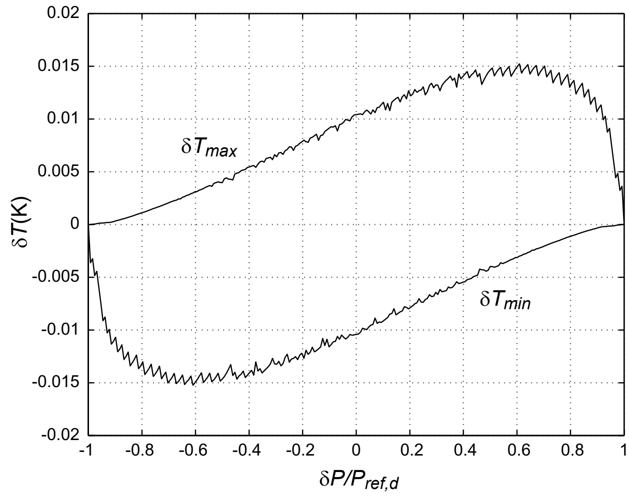

Figure 5-22 *Temperature swing at the output of the thermal filter.*

characteristics are also fixed. In this case, the only component of a differential modulator that requires design is the comparator. This must be done carefully, however, since the thermal filter's finite DC gain means that the comparator non-idealities, such as offset and hysteresis, will affect modulator performance.

Since the modulator is a feedback loop, comparator offset results in a temperature offset in the thermal domain. Comparator offset in the north-south and east-west modulators will thus result in an on-chip temperature gradient, or in other words, an eccentrically located hot spot. This, in turn, will give rise to errors in the computed wind speed and direction [5.5]. The question then arises: what is the maximum tolerable offset? This can be estimated by noting that a similar effect occurs in trimmed first-generation sensors as a result of offset in the instrumentation amplifiers (Fig. 5-4). In this case, offset voltages less than 25µV resulted in satisfactory performance. Since the sensitivity of the smart sensor's thermopiles is similar to that of the first-generation sensor [5.7], the comparator's offset should also less than 25µV.

The comparator's offset will, in general, have a non-zero temperature coefficient. As a result, its offset will be modulated by the heat pulses generated by the various modulators. This may be regarded as a form of inter-symbol interference that will reduce modulator resolution. Such interference can be minimized by autozeroing the comparator before every comparison. The comparator's residual offset can then be reduced below the 25µV level and, as an added advantage, its $1/f$ noise will also suppressed [5.18].

The comparator's gain should be large enough to resolve the microvolt-level thermopile signals. The worst-case situation occurs when the modulator's output is a limit cycle at $f_s/2$. With f_s = 8192Hz, P_{ref} = 0.125W and $T_d = T/2$, the resulting signal amplitude is only about 1µV (rms). A gain of 134dB is then required to produce the 5V swing necessary to drive the heaters. On the other hand, the thermopile signals are dithered by thermal noise with an amplitude of about 64µV (rms) which indicates that a gain of 98dB should suffice. In both cases, the high gain required indicates the use of a multi-stage comparator topology e.g. one consisting of a preamp and a regenerative latch [5.19, 5.20, 5.21].

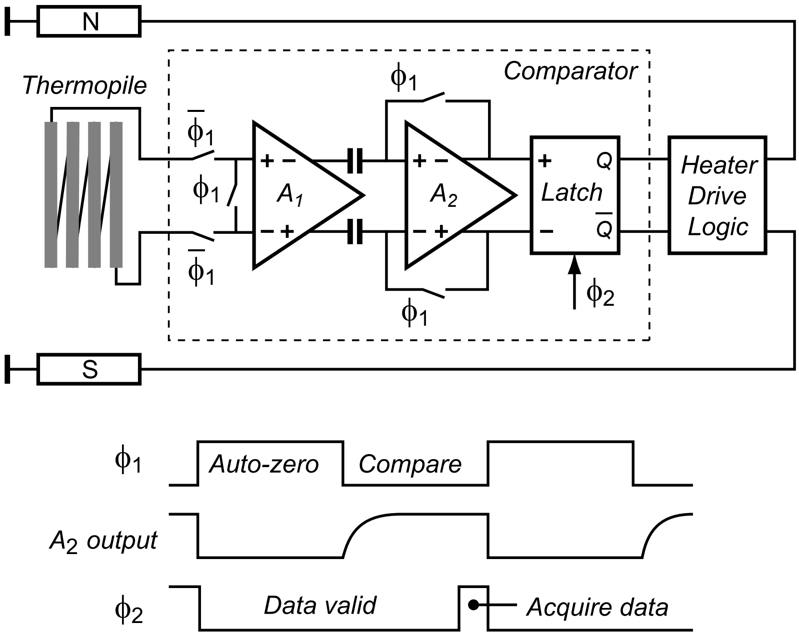

Figure 5-23 *(a) Block diagram of the north-south modulator (b) timing diagram.*

5.4.1 Comparator Architecture

The block diagram of the implemented low-offset multi-stage comparator is shown in Fig. 5-23. A fully differential topology was used to cope with the expected ground "bounce" produced by the large heater currents. In this classic architecture [5.22], the output-referred offset of the first amplifier A_1 and the input-referred offset of the second A_2 are stored on two capacitors during an autozero phase ϕ_1. During the following compare phase, the amplified thermopile output is applied to the input of a regenerative latch, which provides the rest of the required gain and generates logic-level outputs. The comparator's output state is stored by an S-R latch until the following compare phase. The latch output is applied to the heater drive logic, which shares the heaters between the common-mode and differential modulators in a time-multiplexed manner (Section 5.2.6).

The residual offset of the Fig. 5-23 topology will be determined mainly by the offset of the second amplifier V_{os2} and the latch V_{os3}, and by the differential charge injection δQ (due to mismatch) produced by the switches around it. The comparator's offset V_{os} may then be expressed as:

$$V_{os} = \frac{V_{os2} + V_{os3}}{A_1 A_2} + \frac{\delta Q}{A_1 C} \tag{5-10}$$

where C is the capacitance of an autozeroing capacitors. Since V_{os2} and V_{os3} will be in the millivolt range, the first term of (5-10) can easily be reduced to the microvolt level by ensuring that $A_1 A_2 > 1000$. Reducing the magnitude of the second term is, however, more difficult. In principle, for a given level of (process dependent) differential charge injection, it can be made arbitrarily small by increasing the value of the product $A_1 C$. However, A_1 cannot be made too large otherwise the first amplifier will be driven into saturation by its own offset. Also, in the digital process used, area considerations limit the value of linear capacitors to a few picofarads. With minimum size switches, 10% mismatch, C = 2pF and A_1 = 100, SPICE simulations indicate that the value of the second term is about 12μV. In the realized comparator, this will be the dominant source of residual offset.

5.4.2 Circuit Realization

The first amplifier A_1 of the low-offset comparator is shown in Fig. 5-24. It is a cascade of two differential amplifiers with cross-coupled MOSFET loads. The two stages have a combined gain of about 40dB. Since this gain may be expressed as the ratio of two PMOS transconductances multiplied by the ratio of two NMOS transconductances, it will be insensitive to process spread. In order to achieve low noise and low initial offset, the input transistors M_1–M_2 are large PMOS devices. The amplifier's bandwidth is limited to about 1MHz by the low-pass filter formed by the second-stage's output impedance and the autozero capacitors. This limits

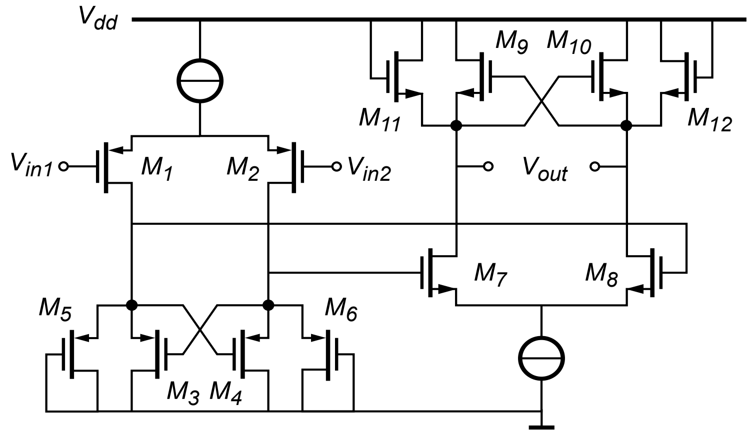

Figure 5-24 *Low offset comparator: First amplifier A_1.*

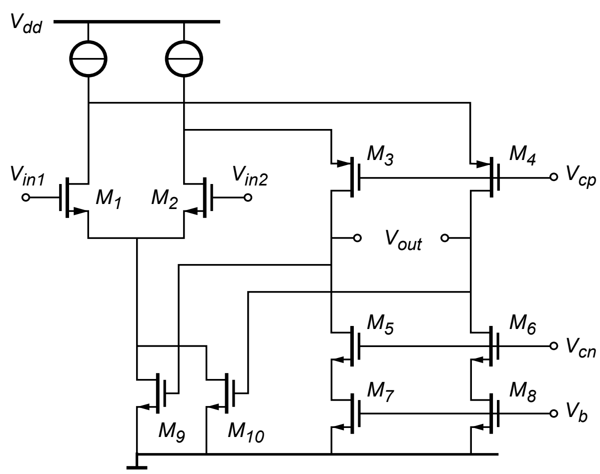

Figure 5-25 *Low offset comparator: Second amplifier A_2.*

the amount of noise that folds back to baseband as a result of the undersampling inherent to autozeroing [5.18].

The second amplifier A_2 of the comparator is a folded-cascode-like amplifier, shown in Fig. 5-25, which provides a gain of 50-60dB. The

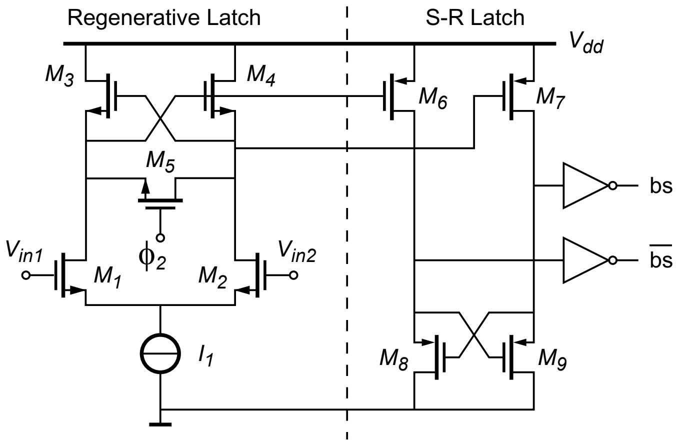

Figure 5-26 *Low offset comparator: latch.*

amplifier is unity-gain stable, which is a fundamental requirement of the Fig. 5-23 topology. Common-mode regulation is achieved by transistors M_9–M_{10} which are biased in the linear region.

The regenerative latch is shown in Fig. 5-26. It consists of a preamp M_1–M_2 that drives a cross-coupled PMOS latch M_3–M_4. The flip-flop is reset by ϕ_2 until shortly before the end of the compare phase, at which time an imbalance at the preamp input will drive it into one state or the other. The current source I_1 ensures that the power consumption of the latch is constant, thus preventing current spikes during regeneration which may be coupled back to the input of the comparator. The regenerative latch is followed by an S-R latch M_8–M_9. The transistors M_6–M_7 are dimensioned so that the state of the flip-flop remains unchanged when the regenerative latch is reset. The outputs of the latch are buffered by two inverters.

5.5 Common-Mode Modulator Design

As discussed in Section 5.2.3, the temperature of the chip T_{chip} and that of the flow T_{amb} should be determined by ΔV_{be} sensing. The inputs of the CM comparator will then be the PTAT voltages generated by two

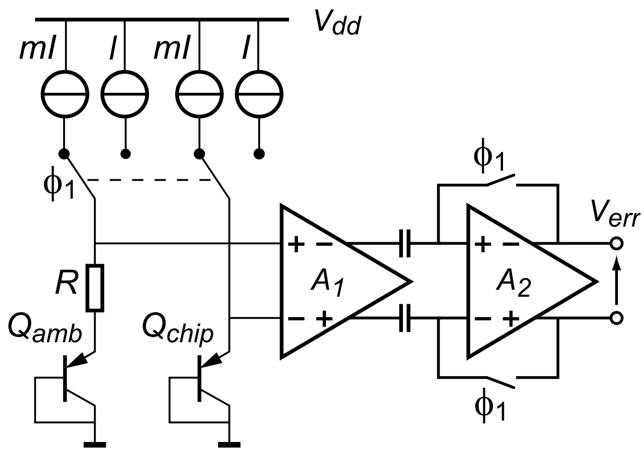

Figure 5-27 *Block diagram of the input stage of the CM comparator.*

temperature-sensing transistors Q_{chip} and Q_{amb} (Fig. 5-7). Since these voltages will have a temperature coefficient of about 200μV/K, the comparator's offset should be in the microvolt range to avoid introducing significant temperature errors. This can be achieved by reusing the autozeroed comparator described in the previous section.

A block diagram of the first two stages of the CM comparator is shown in Fig. 5-27. During the autozero phase, the transistors' emitter current is set to *I*, and during the compare phase it is increased to *mI*, where *m* is a constant. At the end of the compare phase, the output of the second amplifier V_{err} will be proportional to the *change* in the differential input voltage of the first amplifier, and thus:

$$V_{err} \propto \Delta V_{be,\,amb} + (m-1)IR - \Delta V_{be,\,chip} \tag{5-11}$$

Since the temperature-sensing transistors are in a thermal feedback loop, V_{err} will be driven to zero, which implies that:

$$\frac{n_{chip}kT_{chip}}{q}\ln(m) - \frac{n_{amb}kT_{amb}}{q}\ln(m) = (m-1)IR \tag{5-12}$$

where n_{chip} and n_{amb} are the transistors' non-ideality factors and their current gain has been assumed to be constant. If the transistors are identical then $n_{chip} = n_{amb} = n$, and:

$$\Delta T = \left(\frac{q(m-1)}{nk\ln(m)}\right)IR \quad . \tag{5-13}$$

In which case the overheat will be a function of circuit and device parameters only. In practice, R will have a non-zero temperature coefficient. This can be compensated for by generating the bias current I from a reference voltage V_{ref} and a reference resistor R_{ref} with the same temperature coefficient such that I = V_{ref}/R_{ref}. In that case, (5-13) becomes:

$$\Delta T = \left(\frac{q(m-1)}{nk\ln(m)}\right)\left(\frac{RV_{ref}}{R_{ref}}\right) \tag{5-14}$$

The overheat depends only on the reference voltage and well-defined ratios and will thus be temperature independent. In practice, however, there will be some mismatch in the non-ideality factors. Denoting this mismatch as $\Delta n = n_{chip} - n_{amb}$ then (5-14) may be rewritten as:

$$\Delta T = \left(\frac{q(m-1)}{nk\ln(m)}\right)\left(\frac{RV_{ref}}{R_{ref}}\right) - \left(\frac{\Delta n T_{amb}}{n_{chip}}\right) \tag{5-15}$$

While the first term is temperature independent, the second term is PTAT and mismatch dependent. It can be minimized by using an external transistor manufactured in the same process as the sensor, or more realistically, by measuring and compensating for the mismatch that occurs when an off-the-shelf type is used. However, process spread will cause some residual error. Unfortunately, no information about the spread of n was available for the process used. However, an *estimate* can be made based on the specifications for the temperature-sensing transistor of a microprocessor [5.23]. These indicate that the spread on n will lead to overheat errors of about 0.6K at room temperature. At a nominal overheat of 10K, this corresponds to a 6% variation in the sensor's sensitivity at room temperature (5-15). Although the sensor's digital trim will compensate for this error at room temperature, its PTAT nature will cause a worst-case temperature coefficient of 0.2%/K. However, this is of the same order as the expected temperature coefficient of the wind sensor itself [5.24] and is thus acceptable.

The effective value of R will be influenced by the series resistance of the wires connecting Q_{amb} to the chip, and by mismatch in the emitter resistances of Q_{amb} and Q_{chip}. Since the temperature coefficients of these parasitic resistors will not match that of R_{ref}, (5-14) will become slightly temperature dependent. Such errors can be minimized by making R as large as possible, which for a given overheat means that m and I should be minimized.

However, neither m nor I can be made arbitrarily small: m because it determines the amplitude of the *effective* voltage swing at the input of the comparator and hence the signal-to-noise ratio of the CM modulator, I because it must be significantly larger than the leakage currents of the output protection diodes. Values of $m = 8$ and $I = 2.5\mu A$ were chosen as a reasonable compromise between signal-to-noise ratio and resistor accuracy. With an overheat of 10K, $R \sim 100\Omega$.

5.5.1 Circuit Realization

The temperature-sensing transistors are biased by an array of cascaded current mirrors (Fig. 5-28). These are switched between the transistors and ground to minimize supply current changes that might modulate the residual offset of the comparator. Also, to minimize the effect of process spread on the desired 8:1 ratio, the current mirrors were arranged in a common centroid layout and with a ring of dummy cells around the periphery. It is expected that the remaining spread in m will then be less than 0.5%, resulting in a negligible 0.03K worst-case temperature error.

The first amplifier of the CM comparator is shown in Fig. 5-29. It consists of a single differential pair with a resistive load. Compared to the amplifier of Fig. 5-24, it has a much larger linear range, which is necessary in order to handle the expected large spread (±100mV) in the absolute value of the transistors' base-emitter voltages. The increased range is achieved at the expense of gain: the amplifier only has a gain of

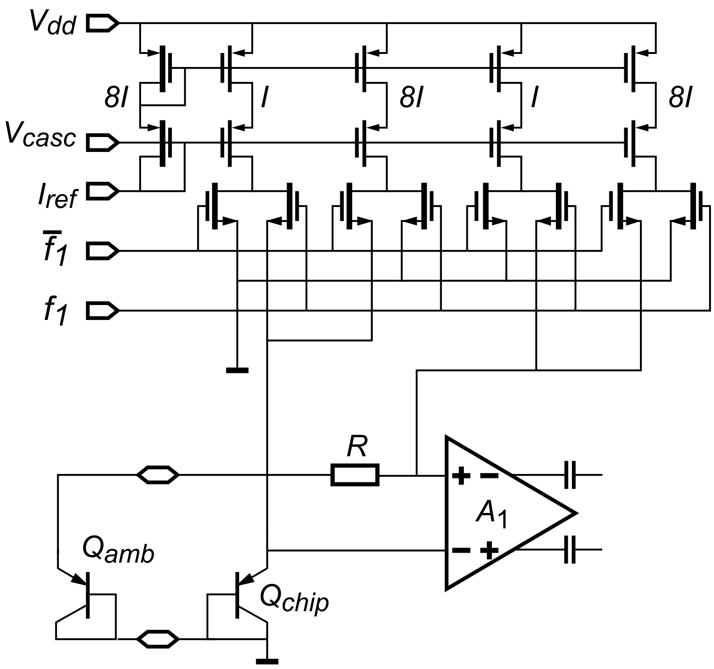

Figure 5-28 *Input stage of the common-mode modulator.*

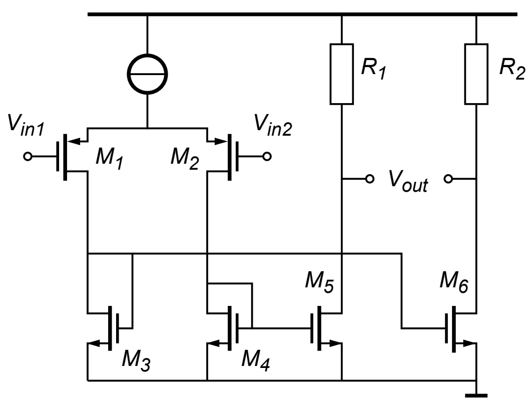

Figure 5-29 *Input stage of the common-mode modulator.*

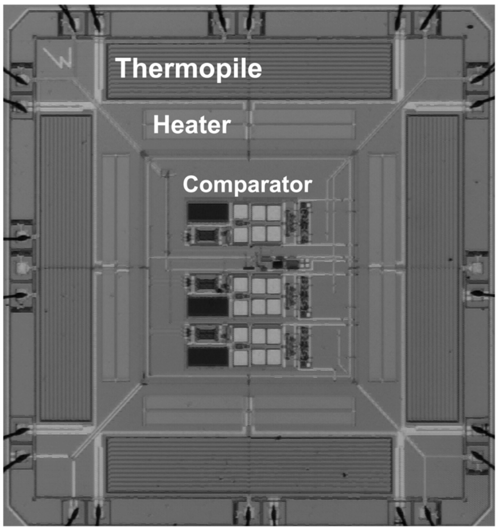

Figure 5-30 *Micrograph of a prototype smart wind sensor.*

about 10. To partially compensate for the increase in residual offset due to differential charge injection, the autozero capacitances where doubled in size. This results in a dominant offset contribution of about 60μV, or a temperature error of 0.3K. The rest of the comparator is essentially the same as that of the differential modulator.

5.6 CMOS Realizations

Two realizations of the smart wind sensor were made; a proof-of-concept prototype and a final design. Both chips were realized in a standard 1.6μm single-poly double-metal CMOS process. The proof-of-concept prototype, consisted of a CMOS wind sensor and three, identical, auto-zeroed comparators (Fig. 5-30). One of the comparators was used to implement the CM modulator, while the other two were used to implement the differential modulators. For simplicity, the CM modulator, like the first-generation sensor, employed V_{be} sensing, while for flexibility, the heater drive logic was implemented off-chip. Using this chip, the feasibility of the TΣΔ modulator-based interface architecture was demonstrated [5.5].

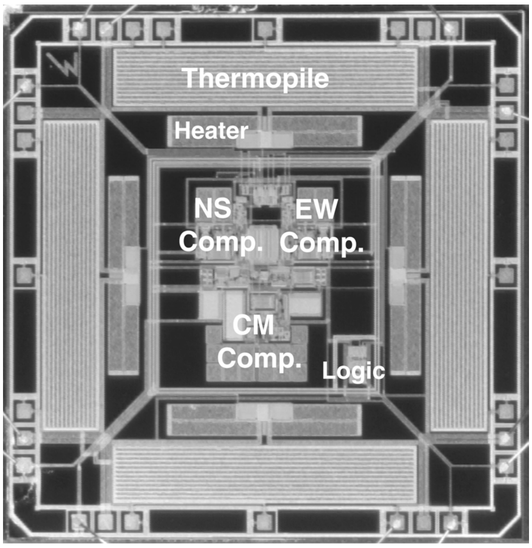

Figure 5-31 *Micrograph of the smart wind sensor.*

A micrograph of the final smart wind sensor is shown in Fig. 5-31. In addition to the three auto-zeroed comparators, all the heater drive circuitry and a more accurate ΔV_{be} sensing scheme were implemented. The interface circuitry, excluding the heaters, consumes 7.5mW from a 5V supply. In contrast, the heaters dissipate 450mW at the nominal overheat of 10K and zero flow. Therefore, the heat dissipation of the interface circuitry has a negligible effect on the sensor's operation.

To minimize thermal crosstalk between the heaters and the circuitry, sensitive circuits such as the input stages of the comparators and the current mirror array were located near the centre of the chip, where thermal gradients are least. Also the PMOS heater drivers (Fig. 5-31), which, due to their finite on-resistance R_{on}, dissipate a significant amount of power, are embedded in the layout of the corresponding heaters. Since these transistors are rather large (for a low $R_{on} < 20\Omega$), PMOS, rather than NMOS types, were used because the former are realized in an n-well,

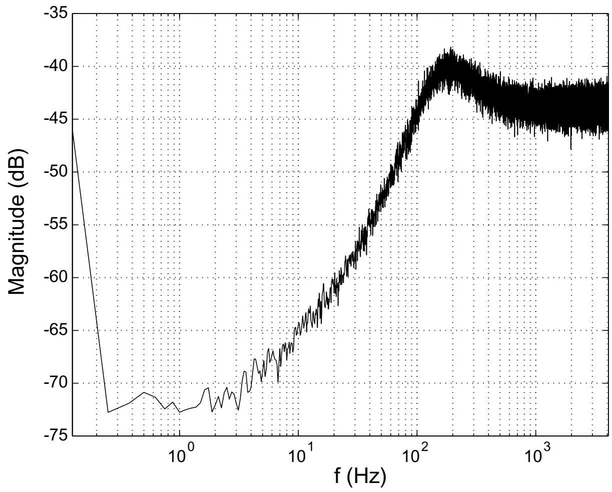

Figure 5-32 *Measured power spectrum of a differential modulator (Hann windowed average of 16, 32kbit, bitstream segments).*

which is connected to the positive supply and thus minimizes the substrate noise caused by the transistor's switching.

5.7 Measurement Results

5.7.1 Modulator Performance

When operated in CP mode, i.e., with the CM modulator disabled, the measured power spectrum of the output of a differential modulator is shown in Fig. 5-32. The spectrum was obtained at zero flow, and with a clock frequency of 8192Hz. It is quite similar to that predicted from simulations (Fig. 5-18), the main difference being that the peak around 100Hz is more subdued. Since the total bitstream power is constant, however, this means that more quantization noise is present at other frequencies. Despite this, the modulator's resolution after decimation by a 8192-tap sinc^2 filter, is still about 10 bits. Enabling the CM modulator changes the shape of the power spectrum slightly, without, however, impacting the noise level near DC. The effectiveness of the autozeroing

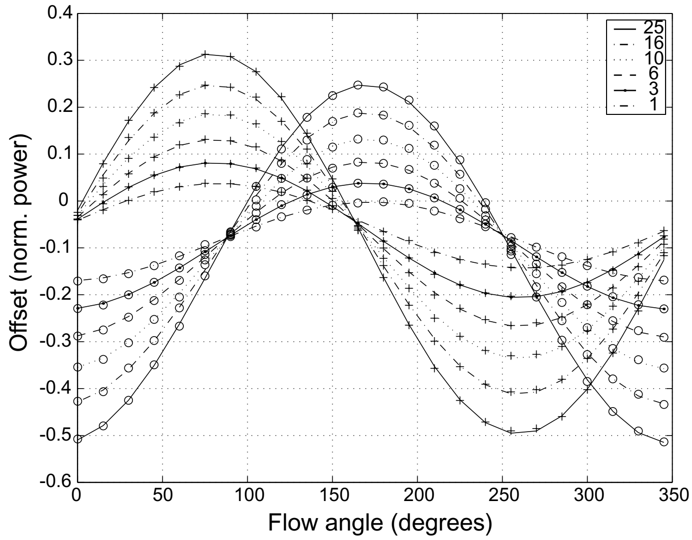

Figure 5-33 Measured output of the north-south (o) and east-west (+) modulators.

scheme used is demonstrated by the fact that no 1/*f* noise is visible in the power spectrum. The large DC offset is due to the packaging asymmetry in the sensor.

5.7.2 Wind Tunnel Testing

The smart wind sensor was built into the aerodynamic housing of the first-generation sensor (Fig. 5-2) and tested in a wind tunnel. The output of the differential modulators was decimated by a 5000-tap sinc^2 filter, followed by an extra 10-tap moving-average filter to further suppress noise.

In CTD mode, the decimated outputs of the differential modulators are sinusoidal functions of wind direction, Fig. 5-33. As expected, the amplitude of these sinusoids is proportional to the square root of flow speed (Fig. 5-34). Unfortunately, their offset (due to packaging asymmetry) is not constant but is a function of flow speed. The first-generation sensor also exhibited similar behaviour [5.5]. Unlike the first-generation sensor, however, the offset of the smart sensor obeys a well-

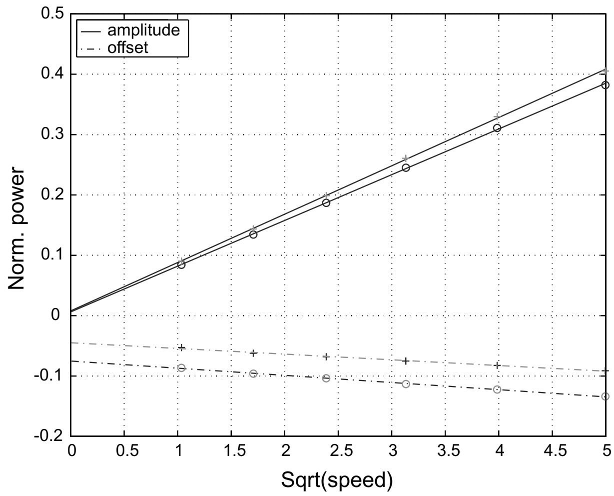

Figure 5-34 *Differential modulator output: Amplitude and offset.*

defined square-root law. This improved offset behaviour is probably due to the fact that the flow-induced temperature differences in the smart wind sensor are dynamically cancelled.

The decimated modulator outputs μ_{ns} and μ_{ew} may then be expressed as:

$$\begin{aligned} \mu_{ns} &= A_{ns}\sin(\Phi_{ns}-\varepsilon_{ns})-b_{ns} \\ \mu_{ew} &= A_{ew}\sin(\Phi_{ew}-\varepsilon_{ew})-b_{ew} \end{aligned} \quad (5\text{-}16)$$

where the amplitude A and the offset b depend on the square-root of flow speed, and ε is a constant phase shift reflecting the orientation of the sensor with respect to the wind-tunnel. Using these relationships, wind speed and direction were computed from the modulator outputs [5.10]. Since (5-16) only approximates the sensor's behaviour, there will be errors in the computed wind speed and direction. Typical results are shown in Fig. 5-35. The errors are less than ±5% and ±3^{o} in wind speed and direction, respectively, for wind speeds between 1 and 25m/s. At wind speeds below 1m/s, it was difficult to make accurate measurements because the sensor's output then requires several minutes to settle fully.

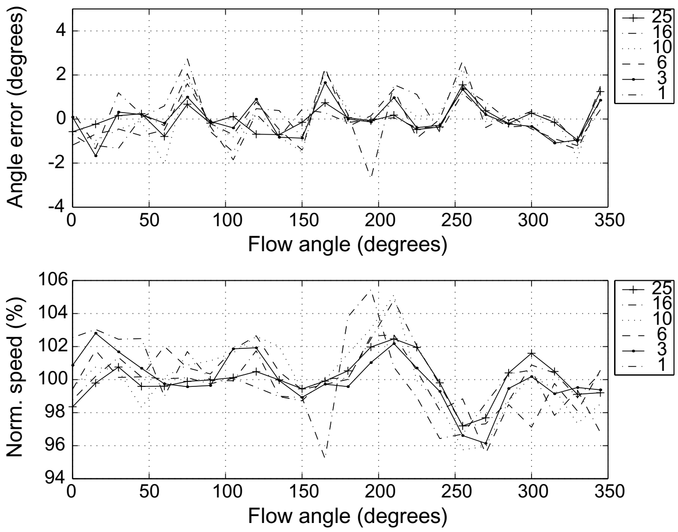

Figure 5-35 *Smart sensor inaccuracy.*

These results are similar to the performance of its predecessor [5.3] and demonstrate that the TΣΔ interface architecture and the presence of on-chip electronics does not degrade sensor performance.

5.7.3 CP versus CTD Mode

As was noted earlier (Section 5.2.4), the differential modulators operate the wind sensor in CP mode. As shown in Section 2.3.4, the bitstream averages μ_{ns}, μ_{ew} are then also a function of wind speed *U*:

$$\mu_{ns} = \frac{\delta P_{ns}}{P_{ref}} = \frac{\sqrt{U_{ns}}}{A + B\sqrt{U_{ns}}} \tag{5-17}$$

$$\mu_{ew} = \frac{\delta P_{ew}}{P_{ref}} = \frac{\sqrt{U_{ew}}}{A + B\sqrt{U_{ew}}} \tag{5-18}$$

where, *A* and *B* are experimentally determined constants that depend on sensor geometry and the physical properties of the flow. From these

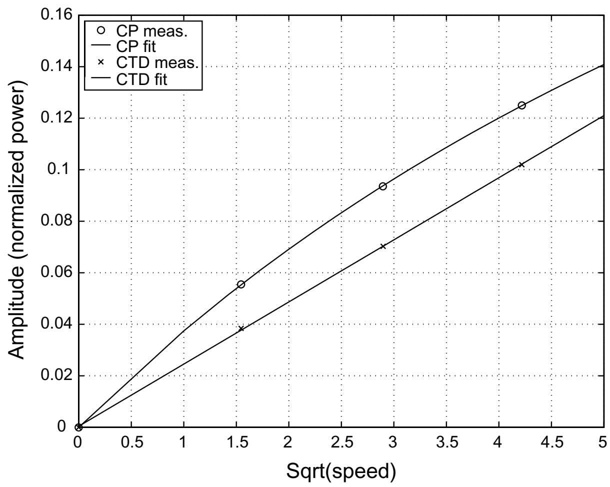

Figure 5-36 *Amplitude A_{ns} vs. square root of wind speed.*

equations, it may be seen that apart from variations in *A* and *B*, the bitstream averages will be independent of variations in ambient temperature.

The amplitude characteristic of the prototype smart wind sensor prototype [5.25] operated in both CP and CTD modes is shown in Fig. 5-36. Also shown are curves obtained by fitting the measurements to (5-17) and (5-18) for CP mode, and to (5-17) and (5-18) for CTD mode. These curves agree well with the measurements indicating the validity of the sensor model. In CP mode, however, the sensor's sensitivity is significantly larger at low flow speeds. This is because the sensor is always heated with the maximum available power, resulting in a larger overheat at low flow speeds. In both modes, however, the errors in wind speed and direction computed from (5-16) are similar.

Since the wind sensor's overheat in CP mode will change with flow speed, its transient response might be expected to be slower than when it is operated in CTD mode. However, from (5-17) and (5-18), the bitstream averages do not depend on the overheat and therefore such changes should only have a second-order effect. In practice, no significant transient response differences were observed between the two modes. In both cases, the sensor responded within a few seconds to transient changes in flow velocity, and then slowly settled to its final value. The settling time increases with decreasing flow speed and was several minutes long at flow speeds below 1m/s. However, the accuracy of these observations is limited by the fact that the transient response of the decimation filter used was about 0.5s long.

Compared to operation in CTD mode, the main advantage of operation in CP mode is that it does not require overheat regulation. As a result, the CM modulator is no longer required, and, more importantly, nor is the external ambient-temperature-sensing transistor. Furthermore, the amount of heat dissipated in the sensor can be significantly reduced (depending on the desired resolution), since it is no longer limited by temperature-sensing inaccuracy. Between the two modes, the speed of the sensor's transient response was not measurably different. Compared to CTD mode, the main drawback of CP mode is that an extra sensor constant must be determined for each component of wind speed. This may result in increased inaccuracy.

5.8 Conclusions

A smart wind-sensor has been realized in standard CMOS technology. The on-chip interface electronics uses thermal sigma-delta modulation techniques to control, and simultaneously digitize the two-dimensional flow-dependent heat distribution in the sensor. This interface architecture is low power and area efficient, and does not interfere thermally with the sensor's operation or increase the required chip area. The interface's bitstream output is decimated off-chip and used to determine wind speed and direction. The results are accurate to within ±4% and $\pm 2^{o}$ in wind speed and direction respectively, over the range 1 to 25m/s.

The interface architecture can operate the sensor in either CTD or CP modes. Although CTD mode is compatible with the signal processing of the first-generation sensor, operating the sensor in CP mode greatly simplifies the electronics while offering the same level of performance.

5.9 References

[5.1] B.W. van Oudheusden, “Integrated silicon flow sensors,” Ph.D. Thesis, Delft University of Technology, 1989.

[5.2] H.-J Verhoeven, “Smart thermal flow sensors,” Ph.D. Thesis, Delft University of Technology, 1996.

[5.3] K.A.A. Makinwa, A. Hagedoorn and J.H. Huijsing, “Industrial design of a solid-state wind sensor,” *Proc. of SiCon 2001*, pp. 68 - 71, Nov. 2001.

[5.4] S.P. Matova, K.A.A. Makinwa and J.H. Huijsing, “Compensation of packaging asymmetry in a 2-D wind sensor,” *IEEE Sensors Journal*, vol. 3, no. 6, pp. 761 - 765, Dec. 2003.

[5.5] B.W. van Oudheusden, “Silicon thermal flow sensor with a two-dimensional direction sensitivity,” *Measurement Science and Technology*, vol. 1, no. 7, pp. 565-575, July 1990.

[5.6] Mierij Meteo B.V., “Product data sheet MMW-005,” http://www.mierijmeteo.nl.

[5.7] K.A.A. Makinwa, S.P. Matova and J.H. Huijsing, “Thermopile design for a CMOS wind-sensor,” in *Sensor Technology 2001*, Kluwer Academic Publishers, pp. 77 - 82, 2001.

[5.8] K.A.A. Makinwa and J.H. Huijsing, “A wind sensor with an integrated low-offset instrumentation amplifier,” *Proc. of ICECS 2001*, vol. 3, pp. 1505-508, Sept. 2001.

[5.9] J. Altet, A. Rubio, E. Schaub, S. Dilhaire, W. Claeys, “Thermal coupling in integrated circuits: application to thermal testing,” *IEEE J. Solid-State Circuits*, vol. 36, no.1, pp. 81- 91, Jan. 2001.

[5.10] K.A.A. Makinwa and J.H. Huijsing, “A wind sensor interface using thermal sigma-delta modulation techniques,” *Sensors and Actuators A: Physical*, vol. 92, no. 1-3, pp. 280 - 285, August 2001.

[5.11] K.A.A. Makinwa and J.H. Huijsing, “A smart wind sensor using time-multiplexed thermal sigma-delta modulators,” *Proc. of ESSCIRC '01*, pp. 460-463, Sept. 2001.

[5.12] E. Yoon and K.D. Wise, “An integrated mass-flow sensor with on-chip CMOS interface circuitry,” *IEEE Trans. on Electron Devices*, vol. 39, no. 6, pp. 1376-1386, June 1992.

[5.13] G.S. Almasi and G.C. Feth, “Thermal noise from long sense lines,” *IEEE Trans. Magnetics*, pp. 64-70, vol. 5, no. 1, March 1969.

[5.14] V. Székely, “THERMODEL: a tool for compact dynamic thermal model generation,” *Microelectronic Journal*, vol. 29, 1998, pp. 257-267.

[5.15] V. Székely, “Identification of RC Networks by deconvolution: Chances and limits,” *IEEE Trans. on Circuits and Systems-I. Theory and applications*, vol. 45, no. 3, March 1998, pp. 244-258.

[5.16] C. Dunn and M. Sandler, "Linearizing sigma-delta modulators using dither and chaos," *Proc. ISCAS 1995*, pp. 625-628, 1995.

[5.17] P. Benabes and R. Kielbasa, "Passive sigma-delta converter design," *Proc. of IMTC 2002*, pp. 469-474, May 2002.

[5.18] C.C. Enz and G.C. Temes, "Circuit techniques for reducing the effects of opamp imperfections: autozeroing, correlated double sampling, and chopper stabilization," *Proc. of the IEEE*, vol. 84, no. 11, pp. 1584-1614, Nov. 1996.

[5.19] F. Chen and B. Leung, "A 0.25mW low-pass passive sigma-delta modulator with built-in mixer for a 10MHz IF input," *IEEE J. Solid-State Circuits*, vol. 32, no.6, pp. 774- 782, June 1997.

[5.20] F. Chen, S. Ramaswamy and B. Bakkaloglu, "A 1.5V 1mA 80dB passive sigma-delta ADC in 0.13um digital CMOS process," *ISSCC Dig. Tech. Papers*, pp. 54-55, Feb. 2003.

[5.21] U. Roettcher, H.L. Fielder and G. Zimmer, "A compatible CMOS-JFET pulse density modulator for interpolative high-resolution A/D conversion," *IEEE J. Solid-State Circuits*, vol. 21, no. 3, pp. 446-452, June 1986.

[5.22] D.J. Allstot, "A precision variable-supply CMOS comparator," *IEEE J. Solid-state Circuits*, vol. 17, no. 6, pp. 1080-1087, 1982.

[5.23] Intel Corporation "Intel Pentium 4 processor with 512-kB L2 cache on 0.13 micron process datasheet," pp. 70, June 2003.

[5.24] S. Oda, M. Anzai, S. Uematsu and K. Watanabe, "A silicon micromachined flow sensor using thermopiles for heat transfer measurements," *IEEE Trans. Instr. and Meas.*, vol. 52, no. 4, pp. 1155-1159, Aug. 2003.

[5.25] K.A.A. Makinwa and J.H. Huijsing, "Constant power operation of a two-dimensional flow sensor," *IEEE Trans. Instr. & Meas.*, vol. 51, no. 4, pp. 840 -844, Aug. 2002.

Conclusions 6

In this thesis, the application of thermal sigma-delta (TΣΔ) modulators to the interfacing of thermal anemometers and calorimetric flow sensors has been investigated. The main conclusions are as follows:

- *TΣΔ modulators can be advantageously used to interface both thermal anemometers and calorimetric flow sensors.*
- *If the thermal inertia of a thermal flow sensor is used as the loop filter of a TΣΔ modulator, the resulting modulator will be stable at practical clock frequencies.*
- *The DC transfer function of a TΣΔ modulator with a thermal loop filter will be non-linear, due to the filter's finite DC gain.*
- *Modulator linearity can be improved either by increasing the clock frequency, or by using an electrical filter in conjunction with the thermal filter.*
- *For the design of TΣΔ modulators, the filter characteristics of a thermal flow sensor may be obtained to sufficient accuracy by measuring its thermal step response.*

These conclusions will be expanded upon in the following.

Interfacing Thermal Flow Sensors with TΣΔ Modulators

Interfacing a thermal flow sensor by embedding it in the feedback loop of one (or more) TΣΔ modulators results in a simple and compact interface architecture (Chapter 1). Compared to an open-loop approach, the accuracy and response speed of the resulting system are enhanced due to the application of feedback (Chapter 2). In addition, the output of a TΣΔ modulator is a digital signal, which can be easily connected to a computer for further processing.

TΣΔ modulators were used to interface a thermal anemometer (Chapter 4) and a 2-D calorimetric flow sensor (Chapter 5). In the latter case, the use of a TΣΔ modulators resulted in a compact architecture, with made it possible to integrate the required circuitry on the same chip as the sensor, despite the use of a relatively coarse 1.6μm CMOS process.

Stability of TΣΔ Modulators

The *thermal* inertia of a thermal flow sensor can be used as the thermal loop filter of a TΣΔ modulator. The characteristics of this thermal filter can be investigated by modelling the sensor as a passive network of *thermal* resistances and capacitances. Using this approach it is shown (Chapter 3) that the filter characteristics of a thermal anemometer are such that the corresponding TΣΔ modulator is unconditionally stable. The filter characteristics of calorimetric flow sensors, however, are such that the modulator is only stable at sufficiently high clock frequencies. In practice, this is not a serious limitation, since such clock frequencies are also necessary for good linearity and resolution.

Linearity of TΣΔ Modulators

Since it is a passive network, a thermal filter will have a finite DC gain. When used as the loop filter of a TΣΔ modulator, the result will be a non-linear DC transfer function. It can be shown (Chapter 3) that for all thermal filters, this non-linearity decreases with increasing clock frequency. In the case of thermal anemometers, a new analytical result has been derived which describes the trade-off between clock frequency and linearity as a function of the anemometer's filter characteristics. For the more complex case of calorimetric flow sensors, an analytical expression for this trade-off could not be derived. For such sensors, modulator linearity must be determined by time-domain simulations. An equivalent discrete-time model was developed with which fast time-domain simulations of modulator behaviour can be made. In the case of a 2-D wind sensor based on a square silicon chip (Chapter 5), 9-bit resolution was obtained.

For practical reasons though, the clock frequency of a TΣΔ modulator cannot be increased indefinitely. Extra resolution can be achieved by the use of an electrical integrator in cascade with the thermal filter. In this manner, 12-bit resolution was obtained with a thermal anemometer based on a self-heated transistor (Chapter 4). Modulator resolution can also be improved by the use of multi-bit quantizers, however, this significantly complicates the complexity of the required circuitry.

Design of TΣΔ Modulators

The detailed design of a TΣΔ modulator requires a good model of its thermal loop filter. An equivalent RC network can be derived by measuring the filter's thermal step response and fitting it to an analytical model (Chapter 4) or by using special-purpose software (Chapter 5). In both cases, the models derived using this approach are accurate enough for design purposes.

It should be noted, however, that for the interfacing of existing thermal flow sensors a simpler approach can be used. This is based on the fact that when the sensor is used as a loop filter, the resulting modulator will be stable (at least at high clock frequencies). The modulator is then simply clocked at a frequency high enough to obtain sufficient linearity and resolution. Modulator design is then reduced to the task of designing a comparator with sufficient speed and resolution. Depending on the sensor's filter characteristics, however, this approach may require impractically high clock frequencies (Chapter 4). In such cases, the same performance, but at a lower clock frequency, can be obtained by using a multi-bit quantizer or an electro-thermal loop filter. In the latter case, however, a model of the sensor's filter characteristics will be required to evaluate the stability of the resulting modulator.

6.1 Future Work

In the hot-transistor anemometer described in Chapter 4, a TΣΔ modulator maintains a self-heated transistor at a constant temperature above that of a reference transistor. This temperature *difference* is determined by V_{be} sensing, and must be trimmed to compensate for the inevitable mismatch between the transistors. However, the need for trimming can be eliminated by using the, more accurate, differential ΔV_{be} sensing technique described in Chapter 5. The increased complexity of the required interface electronics can be handled by the development of a dedicated IC. In addition, the interface electronics could then be re-configured to digitize the reference transistor's temperature, using ΔV_{be} sensing and an *electrical* sigma-delta modulator [6.1]. The resulting sensor would then be able to measure both flow speed and temperature, which represents a significant increase in functionality.

The main drawback of the smart wind sensor described in Chapter 5 is its power dissipation. However, this can be at least *halved* by halving the sensor's overheat and the thermal noise floor of the interface electronics. Both these requirements can be easily met in a sensor redesign, without changing the basic architecture of the interface electronics. Taking advantage of developments in IC technology, this redesign could be made in a more advanced CMOS process, which would make it possible to integrate more functions, such as on-chip decimation and a bus-interface, with little or no increase in the sensor's manufacturing cost.

6.2 Other Applications

Apart from thermal flow sensors, TΣΔ modulators can be used to digitize the information-bearing heat flows that occur in other thermal sensors, e.g. thermal conductivity sensors [6.2], thermal accelerometers [6.3], thermal pressure sensors [6.4] and thermal vacuum (Pirani) sensors [6.5]. Many of the results described in this thesis will also be applicable to the interfacing of such sensors.

The theory of TΣΔ modulators developed in Chapter 3 can also be applied to the design of so-called *passive* sigma-delta (ΣΔ) modulators. These are electrical ΣΔ modulators that employ a loop filter made from passive components. The main motivation for using such filters is that they do not require a power supply. Passive ΣΔ modulators are used in ultra-low-power applications such as battery monitoring [6.6], or in high frequency applications such as in radio receivers, where active filters are either impractical or dissipate too much power [6.7].

6.3 References

[6.1] A. Bakker, "High-accuracy CMOS smart temperature sensors," Kluwer Academic Publishers, 2001.

[6.2] M. Arndt, "Micromachined thermal conductivity hydrogen detector for automotive applications," Proc. of IEEE Sensors 2002, pp. 1571-1575, June 2002.

[6.3] U. Dauderstadt, P.M. Sarro and S. Middelhoek, "Temperature dependence and drift of a thermal accelerometer," Digest of Transducers 97, pp. 1209-1212, June 1997.

[6.4] A. Haberli, O. Paul, P. Malcovati, M. Faccio, F. Maloberti and H. Baltes, "CMOS integration of a thermal pressure sensor system," Proc. of ISCAS 96, vol. 1, pp. 377-380, May 1996.

[6.5] J.J. van Baar, R.J. Wiegerink, T.S.J. Lammerink, E. Berenschot, GJ.M. Krijnen, M. Elwenspoek, "Combined Pirani/bending membrane-pressure sensor," MEMS 2002, pp. 328 - 331, 20-24 Jan. 2002.

[6.6] P. Benabes and R. Kielbasa, "Passive sigma-delta converter design," Proc. of IMTC'02, vol.1, pp. 469-474, May 2002.

[6.7] F. Chen, S. Ramaswamy and B. Bakkaloglu, "A 1.5V 1mA 80dB passive modulator in a 0.13mm digital CMOS process," Digest of Technical Papers ISSCC 2003, vol. 1, pp. 54-55 and 477, Feb. 2003.

Appendix

A.1 DC Non-Linearity in Thermal Sigma-Delta Modulators

The DC transfer function of a thermal sigma-delta (TΣΔ) modulator whose loop filter is a leaky integrator is known to have a fractal staircase structure. The steps in the transfer function represent a fundamental loss of resolution. For this modulator, an exact description of the transfer function is known. However, only loose bounds are known for the case when the modulator's loop filter is an *M*-pole RC impedance. In this appendix it is shown that in that case, an exact description of the transfer function can be derived by extending the results obtained for the leaky integrator.

A.2 Modulator with a Single-pole RC Impedance

The block diagram of a TΣΔ modulator whose loop filter is based on a single-pole thermal RC impedance is shown in Fig. A-1. The thermal resistance R models the loss off heat P_{loss} from the summing node, which is usually the input signal of interest. Changes in P_{loss}, modelled by changes in R, will then change the characteristics of the loop filter. To investigate modulator dynamics for a given loop filter, it is convenient to regard the comparator's reference T_{in} as being the modulator's input signal. For generality, the output of the thermal DAC P_{heat} is considered to be bipolar, i.e., $P_{heat} \in \{+1, -1\}$. The bounds obtained in this case are easily scaled to cover the case of a unipolar DAC.

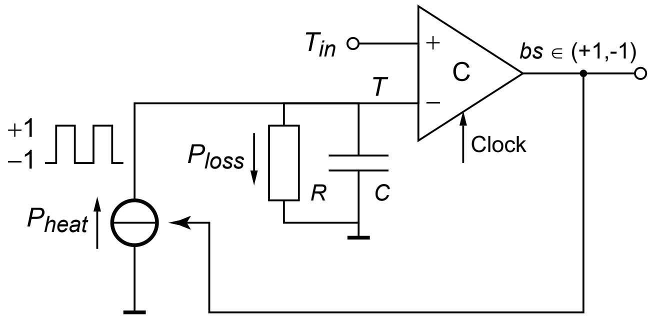

Figure A-1 *Simplified block diagram of a* TΣΔ *modulator with a single-pole impedance as a loop filter.*

A.2.1 Discrete-Time Representation

Denoting the capacitor's state at the *n*-th clock instant by *T*(*n*), the modulator of Fig. A-1 may be described by the difference equation:

$$T(n+1) = g\,\mathrm{sgn}(T_{in} - T(n)) + pT(n) \qquad \text{(A-1)}$$

where $g = R(1-p)$, $p = \exp(-1/(fRC))$ and *f* is the modulator's clock frequency. The corresponding block diagram is shown in Fig. A-2. As shown, this can be transformed so that the input signal and the quantizer output are applied to a common summing node. The corresponding difference equation is:

$$T(n+1) = g(x - \mathrm{sgn}(T(n))) + pT(n) \qquad \text{(A-2)}$$

where:

$$x = T_{in}(1-p)/g = T_{in}/R\,. \qquad \text{(A-3)}$$

The transformed block diagram may be recognized as being a first-order modulator with a leaky integrator, the non-linear dynamics of which have been extensively studied in the seminal work of Feely and Chua [A.1].

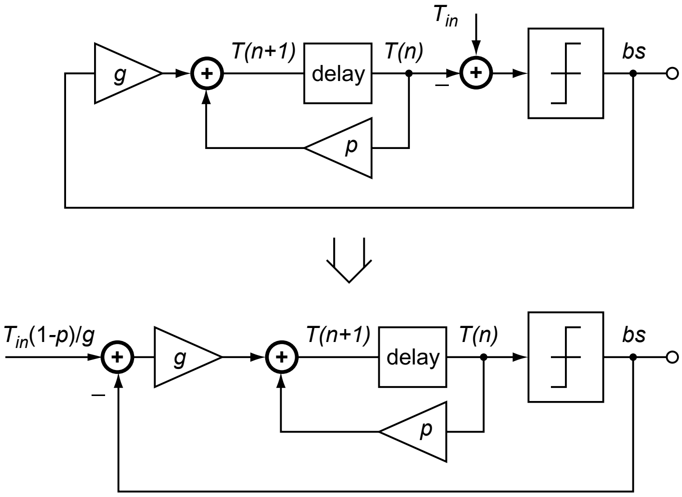

Figure A-2 *Discrete-time equivalent of a TΣΔ Modulator.*

A.2.2 Bounding the Modulator's Input

In order to bound the range of inputs which can give rise to a given limit cycle (and thus to a step in the modulator's DC transfer function), the quantizer is *assumed* to generate a given limit cycle. Consideration of the filter's output then leads to a bound on the range of T_{in} over which the quantizer output will indeed correspond to the given limit cycle. This is known as Tsypkin's method [A.1]. A simplified version of this approach has been used for the m-pole case, the resulting bounds are, however, rather loose [A.2].

For a modulator with a leaky integrator, it has been shown [A.1] that limit cycles of the form "100...0" or "011...1" exist, where the quantizer output is represented symbolically by 1 (+1) and 0 (-1). Such limit cycles will be referred to here as *simple* limit cycles. Also in [A.1], it has been shown that for a given period N, such limit cycles correspond to the widest steps in the modulator's DC transfer function. The width of the steps decreases with increasing N. The widest step occurs in the middle of the transfer function (bitstream average $\mu = 0$) and corresponds to the limit cycle "10". The next widest step corresponds to the limit cycles "100" and "011" and

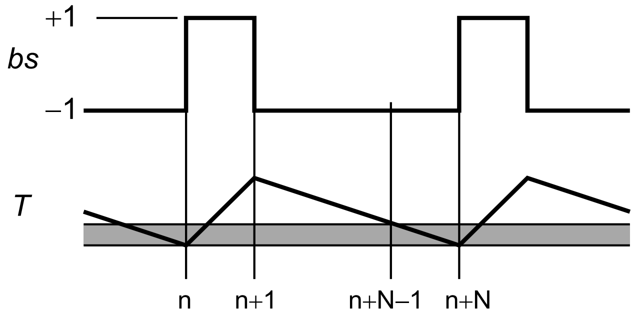

Figure A-3 *A simple limit-cycle.*

so on. These limit cycles correspond to the greatest loss of modulator resolution and will be studied further.

Consider the response of the single-pole filter to the "100...0" limit-cycle of period N shown in Fig. A-3. In this case, the bitstream average $\mu = (2-N)/N$. From (A-1), the maxima $T(n+1)$ and minima $T(n+N)$ of the output waveform are given by:

$$T(n+1) = R(1-p) + pT(n) \tag{A-4}$$

$$T(n+N) = p^{N-1}T(n+1) - R(1-p^{N-1}). \tag{A-5}$$

Since the limit cycle is periodic, $T(n+N) = T(n)$ and so:

$$T(n) = \frac{-R(p^N - 2p^{N-1} + 1)}{(1-p^N)} \tag{A-6}$$

$$T(n+1) = \frac{R(p^N - 2p + 1)}{(1-p^N)} \quad . \tag{A-7}$$

In order for the quantizer to generate this limit cycle, the input signal T_{in} *must* lie in the shaded region of Fig. A-3, that is:

$$T(n) < T_{in} < T(n+N-1). \tag{A-8}$$

From (A-1) and (A-6) it may be shown that:

$$T(n+N-1) = \frac{R(p^N - 2p^{N-1} + 2p^{N-2} - 1)}{(1-p^N)}. \qquad \text{(A-9)}$$

Using (A-3), the bounds given in (A-8) can then be expressed in terms of the input x of the equivalent discrete-time modulator as:

$$x_{min} < x < x_{max} \qquad \text{(A-10)}$$

where:

$$x_{min} = \frac{-(p^N - 2p^{N-1} + 1)}{(1-p^N)} \qquad \text{(A-11)}$$

$$x_{max} = \frac{(p^N - 2p^{N-1} + 2p^{N-2} - 1)}{(1-p^N)}. \qquad \text{(A-12)}$$

By symmetry, the bounds on x for simple limit-cycles of the form "011...1" ($\mu = (N-2)/N$) are obtained by multiplying (A-10) by -1.

The difference between the bounds given in (A-10) is the step width $\Delta x(N)$ corresponding to a simple limit cycle of period N:

$$\Delta x(N) = \frac{2(1-p)^2 p^{N-2}}{(1-p^N)}, \qquad \text{(A-13)}$$

which, using the identity:

$$1 - p^N = (1-p)(p^{N-1} + p^{N-2} + \ldots + 1), \qquad \text{(A-14)}$$

exactly agrees with the conclusions of [A.1].

The widest step corresponds to the “10” limit cycle, its width is given by:

$$\Delta x(2) = \frac{2(1-p)}{(1+p)} \sim \frac{1}{fRC} \qquad \text{(A-15)}$$

for $fRC \gg 1$. In other words, the resolution of a given modulator with a leaky integrator can only be improved by increasing the clock frequency.

A.3 Modulator with an *M*-pole RC Impedance

The block diagram of a TΣΔ modulator whose loop filter is an *M*-pole driving-point impedance is shown in Fig. A-5. The output of the filter may then be seen to be equal to the sum of the outputs of the individual sections. The equivalent discrete time modulator is shown in Fig. A-5, where T_i is the output of the *i*-th RC section and g_i and p_i are the corresponding parameters.

It has been shown [A.3, A.4, A.5], that such a modulator will always be stable provided g_i and p_i are positive, which is the case. Also, bounds on

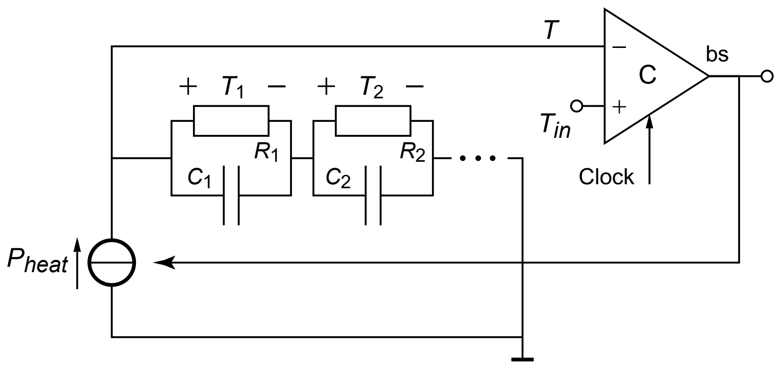

Figure A-4 *Simplified block diagram of a* TΣΔ *modulator with an m-pole loop filter.*

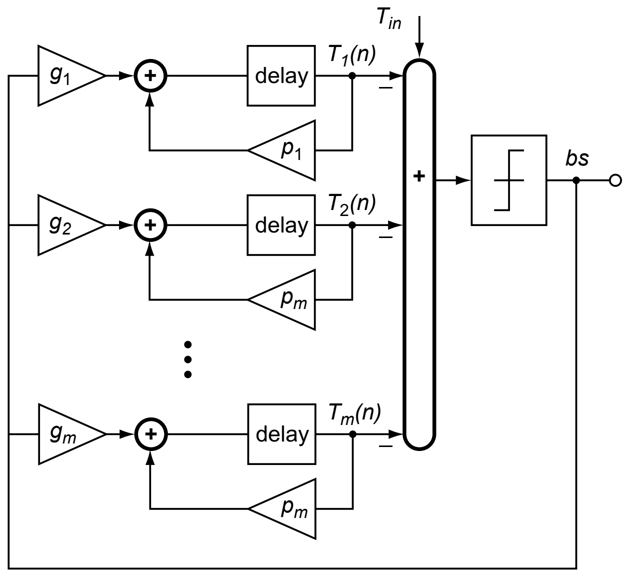

Figure A-5 *Discrete-time equivalent of a TΣΔ Modulator.*

the outputs of the individual sections T_i will exist. Bounds on T_{in} can then be obtained by summing the bounds of the individual sections:

$$\sum_i T_i(n) < T_{in} < \sum_i T_i(n+N-1) \tag{A-16}$$

and so this limit cycle can also exist in the modulator of Fig. A-5. Using (A-10) and scaling by the DC gain of the individual sections $A_i = g_i/(1-p_i)$ yields bounds on the input x:

$$\frac{\sum_i A_i x_{min,\,i}}{\sum_i A_i} < x < \frac{\sum_i A_i x_{max,\,i}}{\sum_i A_i} \tag{A-17}$$

where $x_{min,i}$ and $x_{max,i}$ are the bounds for the individual sections. Once more the widest step corresponds to the “10” limit cycle. The width of the corresponding step $\Delta x(2)$ is given by:

$$\Delta x(2) = \frac{2\sum_i g_i/(1+p_i)}{\sum_i g_i/(1-p_i)} \tag{A-18}$$

Using this equation, the worst-case resolution of the Fig. A-5 modulator can be directly computed.

This approach can be generalized by noting that for every filter section, and for *every* possible limit cycle, bounds $x_{min,i}$ and $x_{max,i}$ can be computed using the methods presented in [A.1]. Equation (A-17) can then be used to compute the corresponding bounds on the input *x*. In this way, the modulator’s entire DC transfer function can be analytically determined.

A.3.1 Example

As an example, we will consider the basic HTA-TΣΔ modulator described in Chapter 4. Its loop filter is a self-heated transistor, which is modelled by a 7-pole thermal impedance. The modulator’s quantizer has a unipolar output i.e., $bs \in \{0, 1\}$, and so the bounds on *x* given in (A-17) must be scaled by a factor 1/2 and then shifted by the same amount. Also, the modulator’s DAC outputs a RTZ pulse, which must be taken into account when determining the gain factors g_i.

The modulator’s DC transfer function (under the conditions described in Chapter 4) was obtained by simulating its response to 2000 values of *x* evenly spaced over the interval $-1 < x < 1$. The bitstream average μ was obtained from 4096 bits. As shown in Fig. A-6, the bounds computed from (A-17) are in excellent agreement with the simulation results.

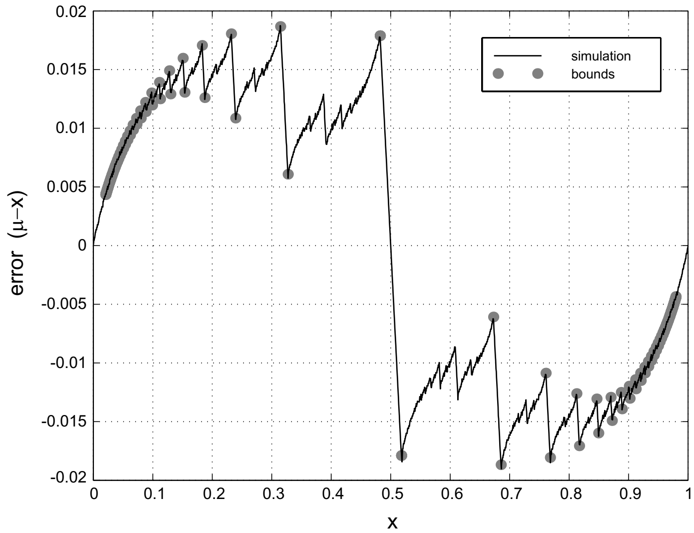

Figure A-6 *Simulated error and predicted bounds of a HTA-TΣΔ modulators.*

A.4 Modulator with an RC Transfer Impedance

What happens when the modulator's filter is a passive *transfer* impedance $H(s)$? In this case the filter's poles will still be real and negative, but their residues may now be negative, which in turn implies that some of the g_i in Fig. A-5 will also be negative. In this case, some of the maximal limit cycles discussed so far may *not* exist. If they do exist, however, bounds on the input x can be obtained using (A-17).

A.4.1 Example 1

As an example we will consider the passive second-order filter:

$$H(s) = \frac{3.12s + 1}{1035s^2 + 71s + 1} \tag{A-19}$$

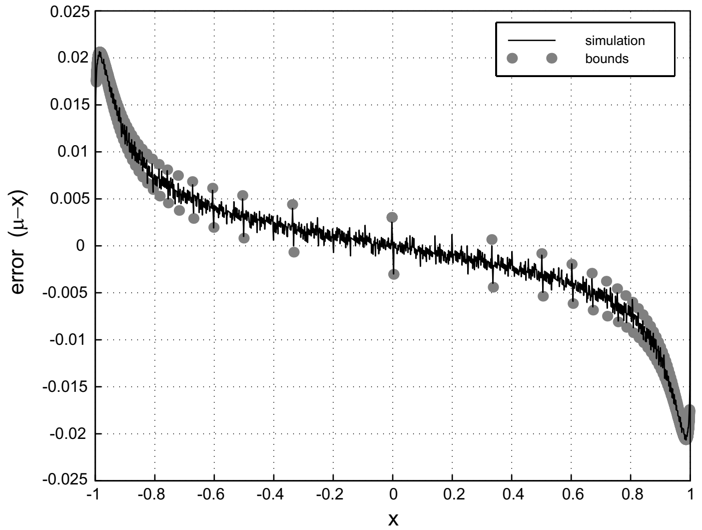

Figure A-7 *Simulated error and predicted bounds of a HTA-TΣΔ modulators.*

proposed in [A.6]. The simulated modulator employs a bipolar DAC and operates at a sample rate of 0.5s. Its DC transfer function was obtained by simulating its response to 2000 values of *x* evenly spaced over the interval $-1 < x < 1$. The bitstream average μ was obtained from 4096 bits. Once more, the bounds computed from (A-17) are in excellent agreement with the simulation results (Fig. A-7), For this modulator, all the simple limit-cycles of period $2 < N < 100$ apparently exist.

A.4.2 Example 2

The differential TSD modulator discussed in Chapter 5 is an example of a modulator in which many of the simple duty cycles do *not* necessarily exist. Due to the leakiness of the various sections, however, the DC transfer function of this modulator will also have a staircase structure with a gain that will be less than one (except when the input *x* is 0, 1 or -1). These observations are borne out by the results of simulation (Fig. 5-19).

A.5 Conclusions

A method for exactly determining the DC transfer function of a ΣΔ modulator whose loop filter is an m-pole passive impedance, has been presented. The resulting transfer function is shown to exhibit a fractal staircase structure. The limit cycles that generate some of the largest steps in the transfer function are known *a priori*, and for this class of *simple* limit cycles, analytical expressions for the location of the resulting steps have been derived. The widest step, and thus the largest loss of resolution occurs when the modulator output takes the form of a "10" limit cycle, and has an average value of zero. In this case, the bounds on T_{in} correspond to the amplitude of the filter's output. We conclude that:

> *The resolution of a ΣΔ modulator whose loop filter is a passive impedance is proportional to the amplitude of the filter's output in response to the "10" limit cycle.*

Since the filter has a low-pass characteristic, modulator resolution can be improved by increasing the clock frequency.

In the general case, when the loop filter is an RC transfer impedance, the simple limit cycles may not exist. It can be stated, however, that the DC transfer function of such a modulator will have a staircase structure and a gain less than one (except when the input is 0, 1 or -1). Both of these phenomena will be mitigated by increasing the clock frequency.

A.6 References

[A.1] O. Feely and L.O. Chua, "The effect of integrator leak in Σ−Δ modulation," *IEEE Trans. on Circuits and Systems*, pp. 1293-1305, vol. 38, no. 11, Nov. 1991.

[A.2] M. Domínguez and L. Castañer, "Bounding of thermal Σ−Δ modulators' output for sensors," Proc. ISCAS '99, vol. 2, pp. 244-247, June 1999.

[A.3] P. Steiner and W. Yang, "Stability of high order sigma-delta modulators," *Proc. of ISCAS '96*, vol. 3, pp. 52-55, May 1996.

[A.4] P. Steiner and W. Yang, "A framework for analysis of high order sigma-delta modulators," *IEEE Trans. on Circuits and Systems II*, vol. 44, no. 1, vol. 44, Jan. 1997.

[A.5] M. Valeri, H. Hans and A. v Roermund, "On the stability analysis of high-order sigma-delta modulators," *Analog Integrated Circuits and Signal Processing*, vol. 36, pp. 47-55, July 2003.

[A.6] P. Benabes and R. Kielbasa, "Passive sigma-delta converter design," *Proc. of IMTC'02*, vol. 1, pp. 469-474, May 2002.

Summary

Thermal sigma-delta modulators are analog-to-digital converters that directly convert an analog heat flow into a digital signal. This thesis describes their application to the interfacing of thermal flow sensors. The digitized heat flow will then be the sensor's heat loss, from which the speed, and in some cases, the direction of a fluid flow can be determined.

In Chapter 1, an introduction to the interfacing of thermal flow sensors is given. This is usually done using either open-loop or closed-loop approaches. The latter results in faster response and better accuracy, but usually at the expense of more complex circuitry. It is shown that a particularly simple implementation of the closed-loop approach can be obtained by embedding a thermal flow sensor in the feedback loop of a sigma-delta (ΣΔ) modulator. In this configuration, the sensor's thermal inertia, acting as a low-pass filter in the thermal domain, is re-used as the modulator's loop filter, greatly simplifying its implementation. The output of the resulting *thermal* sigma-delta (TΣΔ) modulator is a digital signal whose average value is proportional to the sensor's flow-dependent heat loss, and which can be easily connected to a microprocessor.

In Chapter 2, an introduction is given to the two main classes of thermal flow sensors: thermal anemometers and calorimetric flow sensors. The former determine flow speed by measuring total heat loss, while the latter determine both flow speed and direction by measuring differential heat loss. An overview is given of their main characteristics, the various modes in which they can be operated and their implementation in silicon. Based on a literature review, it is shown that for both thermal anemometers and calorimetric flow sensors, the use of closed-loop operating modes does indeed lead to improved performance.

In Chapter 3, the properties of TΣΔ modulators are described. Single-bit single-loop modulator topologies are described with which both thermal anemometers and calorimetric flow sensors can be interfaced. In these topologies, the modulator's loop filter is the sensor's thermal inertia. In general, a thermal filter can be modelled as a distributed RC network, and will therefore have a first-order roll-off at high frequencies and a finite DC gain. Its first-order roll-off means that the resulting modulator will be stable, provided that it is operated at sufficiently high clock frequencies. However, as a result of the filter's finite DC gain, the modulator will have a non-linear DC characteristic. In the specific case when the loop filter is the thermal inertia of a thermal anemometer, an analytical description of this non-linearity has been derived (see Appendix). For the general case, for instance when the loop filter is the thermal inertia of a calorimetric flow sensor, a similar result could not be derived, and so modulator non-linearity must be evaluated by time-domain simulations. These can be efficiently done by simulating the modulator's discrete-time equivalent. For a given thermal loop filter, the degree of modulator non-linearity can be decreased either by increasing the clock frequency, or by making topological modifications to the modulator such as the use of electrical filters and/or multi-bit quantizers.

In Chapter 4, the design and development of a low-cost thermal anemometer based on a pair of standard bipolar transistors is described. Since such transistors are already packaged, this approach considerably simplifies the sensor's mechanical construction. One of the transistors is self-heated, and is maintained at a constant temperature above ambient temperature by a TΣΔ modulator. In this configuration, the self-heated transistor also senses its own temperature, while the second transistor senses that of the flow. A model of the transistor's thermal filtering characteristics was obtained by measuring the transistor's cooling curve. Using this model, it was found that the resulting TΣΔ modulator would have insufficient DC linearity at the clock frequencies of interest. To improve linearity, an extra electrical integrator was used in conjunction with the transistor's thermal inertia. With this electro-thermal loop filter, simulations show that the modulator's linearity is at the 12-bit level. Measurements in a wind tunnel on an anemometer realized with standard bipolar transistors show that it has a well-defined square-root-law characteristic, and a time constant of about two seconds.

In Chapter 5, the design and development of a smart wind sensor in a standard CMOS process is described. It is an improved version of a commercially available wind sensor, which is based on a 2-D calorimetric flow sensor implemented on a square silicon chip. The sensor's interface electronics was implemented with discrete components, which required manual trimming, and therefore significantly increased the size and cost of the complete sensor system. In contrast, the interface electronics of the smart wind sensor is integrated on the same chip as the sensor and does not require manual trimming. This was done without increasing the sensor's area, and hence its cost, by using a new interface architecture consisting of three TΣΔ modulators. One modulator maintains the sensor at a constant temperature above ambient temperature (the overheat), while the other two digitize orthogonal components of its (flow-dependent) differential heat loss. The bitstream outputs of the latter are decimated by an external microprocessor, and used to compute wind speed and direction. An accurate model of the thermal loop filter of these modulators was extracted from step response measurements made with a specially designed test chip. Simulations using this model show that the modulator's DC linearity is at the 9-10 bit level, which is high enough not to compromise the wind sensor's performance. To eliminate the need for trimming, the overheat is determined by bipolar transistors, read out using a new differential ΔV_{be} sensing technique, which significantly reduces errors due to transistor mismatch. Measurements in a wind tunnel show that the performance of the smart sensor is at least as good as that of its predecessor (errors in wind speed and direction of less than ±(0.5m/s +3%) and ±3^{o} respectively over the range 0.5 to 25m/s). Since it has no moving parts, and thus requires very little maintenance, this sensor is well suited for meteorological applications.

Samenvatting

Thermische sigma-delta modulators zijn analoog-naar-digitaal omzetters die rechtstreeks een warmtestroom naar een digitaal signaal converteren. Dit proefschrift beschrijft hoe ze kunnen worden toegepast voor het uitlezen van thermische stromingssensoren. Het gedigitaliseerd signaal is dan het warmteverlies van de sensor, waaruit de snelheid en, in sommige gevallen, de richting van een stroming bepaald kan worden.

In hoofdstuk 1 wordt een introductie gegeven tot het uitlezen van thermische stromingssensoren. Meestal worden zulke sensoren uitgelezen met of zonder gebruik van terugkoppeling. Terugkoppeling resulteert in een snellere respons en een betere nauwkeurigheid, wat gewoonlijk ten koste gaat van complexere schakelingen. Aangetoond wordt dat een bijzonder eenvoudige realisatie van een teruggekoppeld systeem kan worden verkregen wanneer een thermische stromingssensor in de terugkoppellus van een sigma-delta modulator wordt geplaatst. In deze configuratie fungeert de thermische traagheid van de sensor als een laagdoorlaatfilter en tevens als het lusfilter van de modulator, wat de implementatie ervan aanzienlijk vereenvoudigt. Het uitgangssignaal van de resulterende *thermische* sigma-delta modulator is een digitaal signaal waarvan de gemiddelde waarde evenredig is met het stromingsafhankelijke warmteverlies van de sensor; deze signaal kan gemakkelijk op een microprocessor aangesloten worden.

In hoofdstuk 2 wordt een introductie gegeven tot de twee hoofdklassen van thermische stromingssensoren: thermische anemometers en calorimetrische stromingssensoren. De eerste bepalen de snelheid van een stroming door het totale warmteverlies te meten, terwijl de laatste zowel de snelheid als de richting van een stroming bepalen door een differentieel warmteverlies te meten. Er wordt een overzicht gegeven van hun hoofdeigenschappen, de verschillende modi waarin ze gebruikt kunnen

worden en hun implementatie in silicium. Op basis van een literatuuronderzoek wordt aangetoond dat voor zowel thermische anemometers als voor calorimetrische stromingssensoren het gebruik van terugkoppeling inderdaad tot betere prestaties leidt.

In hoofdstuk 3 worden de eigenschappen van thermische sigma-delta modulatoren beschreven. Er worden één-bits modulator topologieën met een enkele lus beschreven, waarmee zowel thermische anemometers als calorimetrische stromingssensoren kunnen worden uitgelezen. In deze topologieën is het lusfilter van de modulator de thermische traagheid van de sensor. Een thermisch filter kan in het algemeen worden gemodelleerd als een gedistribueerd RC netwerk en zal daarom een eerste-orde afval bij hoge frequenties en een eindige DC versterking hebben. Deze eerste-orde afval betekent dat de resulterende modulator stabiel zal zijn, mits hij wordt gebruikt bij voldoende hoge klokfrequenties. Ten gevolge van de eindige DC versterking zal de modulator echter een niet-lineaire DC karakteristiek hebben. Voor het specifieke geval dat het lusfilter wordt gevormd door de thermische traagheid van thermische anemometer is een analytische beschrijving van deze niet-lineariteit afgeleid (zie appendix). In het algemene geval, waartoe de thermische traagheid van een calorimetrische stromingssensor behoort, kon een dergelijk resultaat niet worden afgeleid. De stabiliteit van de modulator moet dan worden geëvalueerd met behulp van tijddomein simulaties. Deze kunnen op een efficiënte manier gedaan worden door de equivalente discrete-tijd modulator te simuleren. Voor een gegeven thermisch lusfilter kan de mate van niet-lineariteit worden verminderd door de klokfrequentie te verhogen of door wijzigingen aan te brengen in de topologie van de modulator, zoals het gebruik van elektrische filters en/of multi-bit kwantisatoren.

In hoofdstuk 4 wordt het ontwerp en de ontwikkeling van een goedkope thermische anemometer beschreven die is gebaseerd op een tweetal standaard bipolaire transistoren. Aangezien zulke transistoren al in een behuizing zitten, vereenvoudigt deze aanpak de mechanische constructie van de sensor aanzienlijk. Eén van de transistoren verwarmt zichzelf en wordt op een vaste temperatuur boven de omgevingstemperatuur gehouden met behulp van een TΣΔ modulator. In deze configuratie meet deze transistor ook zijn eigen temperatuur, terwijl de andere transistor die van de stroming meet. Een model van de thermische filterkarakteristiek van de transistor is verkregen door de afkoelingscurve van de transistor te meten. Met behulp van dit model is vastgesteld dat de resulterende TΣΔ modulator onvoldoende DC lineariteit zou hebben bij de beoogde klokfrequenties. Om de lineariteit te verbeteren is een extra elektrische integrator gebruikt in combinatie met de thermische traagheid van de transistor. Simulaties laten zien dat de lineariteit met dit elektro-thermische lusfilter ongeveer 12 bits is. Metingen in een windtunnel aan een anemometer met standaard bipolaire transistoren vertonen een goed gedefinieerde wortelkarakteristiek en een tijdsconstante van ongeveer twee seconden.

In hoofdstuk 5 wordt het ontwerp en de ontwikkeling van een slimme windsensor in een standaard CMOS proces beschreven. Het is een verbeterde versie van een commercieel beschikbare windsensor, die is gebaseerd op een 2-D calorimetrische stromingssensor die is geïmplementeerd op een vierkante siliciumchip. De uitleeselektronica van deze sensor is geïmplementeerd met discrete componenten die handmatig moeten worden afgeregeld, wat het complete sensorsysteem aanzienlijk groter en duurder maakt. De uitleeselektronica van de slimme windsensor daarentegen is geïntegreerd op dezelfde chip als de sensor en vereist geen handmatige afregeling. Dit werd bereikt zonder het oppervlak van de sensor te vergroten - en dus zonder een hogere kostprijs - door gebruik te maken van een nieuwe uitleesarchitectuur bestaande uit drie TΣΔ modulatoren. Eén modulator houdt de sensor op een constante temperatuur boven de omgevingstemperatuur, terwijl de andere twee de orthogonale componenten van zijn (stromingsafhankelijke) differentiële warmteverlies digitaliseren. De bitstream uitgangssignalen van laatstgenoemde modulatoren worden gedecimeerd door een externe microprocessor en gebruikt om de windsnelheid en windrichting te berekenen. Een nauwkeurig model van het thermisch lusfilter van deze modulatoren is geëxtraheerd uit de stapresponsie, gemeten met een speciaal daarvoor ontworpen testchip. Simulaties met dit model tonen aan dat de DC lineariteit van de modulator 9-10 bits bedraagt. Dit is voldoende om de prestaties van de windsensor niet negatief te beïnvloeden. Om afregelen overbodig te maken, wordt de temperatuurverhoging gemeten ten opzichte van die van de omgeving met behulp van bipolaire transistoren die worden uitgelezen met een nieuwe differentiële ΔV_{be} meettechniek. Dit verkleint fouten ten gevolge van ongelijkheid van de transistoren aanzienlijk. Metingen in een windtunnel tonen aan dat de prestaties van de slimme sensor minstens zo goed zijn als die van zijn voorganger (fouten in windsnelheid en windrichting kleiner dan ±(0.5m/s +3%) en ±3^o respectievelijk over een bereik van 0.5 tot 25m/s). Aangezien de sensor geen bewegende delen heeft en daardoor erg weinig onderhoud behoeft, is hij zeer geschikt voor meteorologische toepassingen.

Acknowledgments

There is an old saying, "no man is an island," and indeed this thesis would not have been written without the encouragement and support of many people. In this section, I wish to acknowledge their contributions.

In the first place, I want to thank Prof. Han Huijsing for giving me the opportunity of achieving a lifelong ambition and for his unswerving support and encouragement.

My special thanks go to my roommates Michiel and Martijn for their critical proofreading, "instant" translations and many interesting discussions about life, the universe and everything else. My thanks also go to Lucien, Ovidiu, Svetla, Paulo and Frerik for their support and encouragement. I am especially indebted to Anton Bakker for his friendship and practical support.

I would like to thank all my colleagues at the Electronic Instrumentation Laboratory for their individual contributions towards a great working environment. In particular, I want to thank Willem, Jeff, Ger, Piet, Jeroen, Maureen, Harry, Ourang, Antoon, Evelyn, Inge and Trudie for their willingness to solve all the problems I made their own, usually with little or no advance notice. I am also grateful to Mirjam Nieman for her careful correction of the English and Dutch text.

I want to thank the people at Mierij Meteo and especially Arend Hagedoorn and Karel van der Wal for their help in performing the wind tunnel measurements. I also thank Bronkhorst High-Tech and especially Joost Lötters for their technical support. In packaging the wind sensor prototypes, Frank Riedijk, Sander van Herwaarden and Wim van der Vlist went beyond the call of duty, for which I am grateful.

Acknowledgments

For introducing me to the theory and practice of thermal modelling, I want to thank Prof. Vladimír Székely and Michael Glavanovics.

I want to thank my mother, who started it all by giving me a radio kit, and without whom none of this would have been possible. I also want to thank the rest of my family and my in-laws who always believed that this thesis would become a reality.

Most especially, I want to thank my wife, Abiola as well as my boys, Tumi, Remi and Soji for their patience and support during my long working hours and frequent absences. The boys did their very best to be "quiet" while I was writing, while Abiola created the "enabling environment" in which this thesis could be written.

My final thanks go to the Lord, who has indeed directed my paths and "made them straight," (Proverbs 3:6).

Kofi Makinwa

Delft, May 2004

List of Publications

Journal Papers

[1] K.A.A. Makinwa and J.H. Huijsing, "Constant power operation of a 2-D flow sensor," *IEEE Trans. Instrumentation and Measurement*, vol. 51, no. 4, pp. 840-844, Aug. 2002.

[2] K.A.A. Makinwa and J.H. Huijsing, "A smart wind sensor using thermal sigma-delta modulation techniques," *Sensors and Actuators A: Physical*, vol. 97-98, pp. 15 - 20, April 2002.

[3] K.A.A. Makinwa and J.H. Huijsing, "A wind sensor interface using thermal sigma-delta modulation techniques," *Sensors and Actuators A: Physical*, vol. 92, no. 1-3, pp. 280 - 285, August 2001.

[4] S.P. Matova, K.A.A. Makinwa and J.H. Huijsing, "Compensation of packaging asymmetry in a 2-D wind sensor," *IEEE Sensors Journal*, vol. 3, no. 6, pp. 761 - 765, Dec. 2003.

Conference Papers

[5] K.A.A. Makinwa and J.H. Huijsing, "A smart CMOS wind sensor," *Digest of Technical Papers ISSCC 2002*, pp. 432 - 433, Feb. 2002.

[6] J.F. Witte, K.A.A. Makinwa and J.H. Huijsing, "An oscillator based on a thermal delay line," *Proc. of SeSens2002*, p. 170, Nov. 2002.

[7] K.A.A. Makinwa, S.P. Matova and J.H. Huijsing, "Modelling and compensation of packaging asymmetry in a 2-D wind sensor", *Proc. of THERMINIC 2002*, Oct. 2002.

[8] S.P. Matova, K.A.A. Makinwa and J.H. Huijsing, "Compensation of packaging asymmetry in a 2-D wind sensor," *Proc. of IEEE Sensors 2002*, vol. 2, pp. 1256-1259, 2002.

[9] K.A.A. Makinwa, V. Székely and J.H. Huijsing, "Modelling and simulation of thermal sigma-delta modulators," *Proc. of IMTC 2002*, vol. 1, pp. 261 - 264, May 2002.

[10] K.A.A. Makinwa and J.H. Huijsing, "A Wind Sensor with an integrated chopper amplifier," *Proc. of SeSens 2001*, pp. 830 - 833, Nov. 2001.

[11] K.A.A. Makinwa, A. Hagedoorn and J.H. Huijsing, "Industrial design of a solid-state wind sensor," *Proc. of SiCon 2001*, pp. 68 - 71, Nov. 2001.

[12] K.A.A. Makinwa and J.H. Huijsing, "A smart wind sensor using time-multiplexed thermal sigma-delta modulators," *Proc. of the ESSIRC 2001*, pp. 460 - 463, Sept. 2001.

[13] K.A.A. Makinwa and J.H. Huijsing, "A wind sensor with an integrated low-offset instrumentation amplifier," *Proc. of ICECS 2001*, vol. 3, pp. 1505 - 1508, Sept. 2001.

[14] K.A.A. Makinwa and J.H. Huijsing, "A smart wind sensor based on thermal sigma-delta modulation," *Digest of Transducers 2001*, vol. 1, pp. 68 - 71, June 2001.

[15] K.A.A. Makinwa and J.H. Huijsing, "Constant power operation of a two-dimensional flow sensor using thermal sigma-delta modulation techniques," *Proc. of IMTC 2001*, vol. 3, pp. 1577 - 1580, May 2001.

[16] K.A.A. Makinwa and J.H. Huijsing, "A wind sensor with integrated interface electronics," *Proc. of ISCAS 2001*, pp. 356 - 359 vol. 1, May 2001.

[17] K.A.A. Makinwa, S.P. Matova and J.H. Huijsing, "Thermopile design for a CMOS wind-sensor," in *Sensor Technology 2001*, Kluwer Academic Publishers, pp. 77 - 82, 2001.

[18] K.A.A. Makinwa and J.H. Huijsing, "A wind sensor interface using thermal sigma-delta modulation," *Proc. of Eurosensors XIV*, pp. 249 - 252, Sept. 2000.

Invited Presentations

[19] K.A.A. Makinwa and J.H. Huijsing, "Interface Electronics", Tutorial presented at the 2nd Eurosensors School, Eurosensors 2001.

[20] K.A.A. Makinwa and J.H. Huijsing, "Low-offset amplifiers for sensor applications," Tutorial presented at the IEEE Sensors Conference 2003.

About the Author

Kofi Makinwa studied at the Obafemi Awolowo University, Ile-Ife, Nigeria where he received a B.Sc. degree (1st class honours) in 1985 and an M.Sc. degree in 1988, both in Electronic Engineering. In 1989, he received an M.E.E. degree (with distinction) from the Philips International Institute, Eindhoven, The Netherlands.

He began his working career in 1989 as a research scientist at Philips Research Laboratories in Eindhoven, a position he held until 1999. There, he developed electronic systems for interactive displays, and for optical and magnetic storage systems. He is currently an assistant professor at Delft University of Technology, Delft, The Netherlands.

His main research interest is in the design of analog interface circuits for sensors, and in particular, the application of sigma-delta modulation techniques to the realization of smart sensors.

24/5/2004